UNIVERSIDAD DE LAS AMÉRICAS PUEBLA

School of Sciences

Department of Chemical Biological Sciences

Development of electrodes based on titanium dioxide nanotubes modified with zirconium and iron MOFs for the detection and degradation of persistent organic pollutants

Thesis presented to fulfill the requirements of the Honors Program by the student

Andrea Fernanda García Ballesteros

ID 166753

Bachelor in Nanotechnology and Molecular Engineering

Dra. Mónica Cerro López and Dr. Ricardo Navarro Amador

San Andrés Cholula, Puebla. Fall, 2023

Signature sheet

Thesis presented to fulfill the requirements of the Honors Program by the student Andrea Fernanda García Ballesteros, ID 166753

Thesis Advisor

_____

Dra. Mónica Cerro López

Thesis President

_____

Dr. Ricardo Navarro Amador

Thesis Secretary

_____

Dra. Deborah Xanat Flores Cervantes

Index

1. Introduction

Water resources are being continuously contaminated by anthropogenic activities, mainly through industry activities, introducing hazardous pollutants into water bodies (Ara et al., 2022). One of the biggest environmental concerns worldwide is the pollution of water by organic compounds. Persistent organic pollutants (POPs) are of particular interest owing to their resistance to conventional chemical, biological, and photolytic degradation processes (Garcia-Segura & Brillas, 2017). POPs are toxic chemical contaminants that are bioaccumulative and remain in the environment for long periods of time, prone to long-range atmospheric transboundary migration and deposition. These contaminants represent a potential hazard to human health, wildlife, and the environment (Ashraf, 2017).

POPs can accumulate in soil, air, waters, and biota, with a half-life of years or even decades in soils and many days in the atmosphere. Owing to their semi-volatile nature, POPs are highly spread in the environment at low concentrations through waters or the air. Environmental temperatures can cause POPs to easily volatilize and be carried in the gas phase for long atmospheric distances, subsequently condensing in systems with low temperatures. When POPs reach cold environments, they sink, and they remain settled because the low temperatures prevent them from breaking down (Ashraf, 2017).

POPs tend to be lipophilic compounds; therefore, they tend to bind to organic solids, avoiding aqueous media in marine and terrestrial ecosystems. When they enter organisms, POPs are stockpiled in the fatty tissues being preserved in biota and climbing up the food chain. Thus, from water and air, POPs can reach soil and plants, being introduced to animals and humans. Because of their large production and use in different industries, some of the most common recalcitrant POPs are pesticides, pharmaceuticals,

and dyes (Garcia-Segura & Brillas, 2017), it is imperative to address their removal from wastewaters.

It is estimated that 70,000 tons of dyes are produced each year globally, azo dyes representing 70% of them (Ara et al., 2022; Chung, 2016). Azo dyes represent two-thirds of all synthetic dyes, being the most widely used in the industry due to their bright colors (Chung, 2016). This organic dyes are especially used in the textile and food industry (Garcia-Segura et al., 2013). Generally, dyeing processes are performed in aqueous solutions, producing large amounts of colored wastewater effluents (Cerrón-Calle et al., 2019). In the textile industry, inefficiencies in dyeing processes result in the loss of large amounts of dyestuffs (up to 50%) into wastewaters and are consequently discharged into water bodies (Ferraz et al., 2013).

Azo dyes are organic compounds that are comprise of a diazotized amine bonded to an amine or a phenol group through azo linkages, their precursors being aromatic amines. Azo compounds have the following chemical structure: R-N=N-R'; where -N=N- is the diazo group (the chromophore) and R/R' are alkyl or aryl groups. The word azo comes from the French term for nitrogen (Chung, 2016). The International Union of Pure and Applied Chemistry (IUPAC) defines an azo compound as a derivative of diazene (diimide), HN=NH, where the hydrogens are substituted with hydrocarbyl groups (IUPAC, 2019).

Azo dyes and their byproducts are genotoxic, carcinogenic, and mutagenic, endangering human and animal health (Chung, 2016). The pollution of azo dyes in water bodies can perturb the food chain through light adsorption, altering the ecosystems as a result (Ara et al., 2022). Furthermore, they can cause changes in the biological cycles of

aquatic biota, impacting the photosynthesis and oxygenation of water bodies and obstructing the passage of sunlight through the water (Ferraz et al., 2013). The exposure to azo dyes can take place via ingestion, inhalation, or skin contact (Chung, 2016). Inside the human body, these dyes are biotransformed by liver enzymes and intestinal microflora into aromatic amines, causing cancer (Ara et al., 2022).

Azo dyes are very stable in aquatic solutions and are persistent in water bodies, traditional wastewater treatments are usually not enough to remove azo dyes since they are stable under sunlight, do not fade away through washing, and have a high resistance to biodegradation in aerobic conditions (Garcia-Segura et al., 2013). Hence, traditional wastewater treatment methods are not sufficient to remove azo dyes from water (Chung, 2016). This high stability and low biodegradability, attributed to the azo bonds, cause the need for novel treatments for their removal (Cerrón-Calle et al., 2019). Indiscriminate disposal of azo dye poses a serious threat to human and environmental safety; on that account, azo dye polluted waters must be treated before entering the ecosystem (Ara et al., 2022).

To degrade azo dyes in wastewater, several physicochemical treatments have been applied, such as adsorption, filtration, coagulation, along with some biotreatments. Nevertheless, advanced oxidation processes (AOPs) have shown great potential for faster and even complete decolorization of wastewater. The effectiveness of AOPs is based on the generation and reaction of strong reactive oxygen species, like hydroxyl or superoxide radicals, as non-selective oxidants of organic pollutants (Garcia-Segura et al., 2013). AOPs are considered as green technologies since the oxidant radicals have relatively short lifetimes and their oxidation products are environmentally friendly (Liu et al., 2022). The oxidation of the organic dye causes the rupture of the azo bonds, enhancing the

biodegradability of these contaminants; thus, the application of inexpensive technologies for the treatment of dye polluted wastewaters is of great interest (Cerrón-Calle et al., 2019). Methyl red is considered a representative azo dye on account of its simple chemical structure (**Fig. 1.1.**) which facilitates the analysis during decolourization processes (Vatandoostarani et al., 2017).

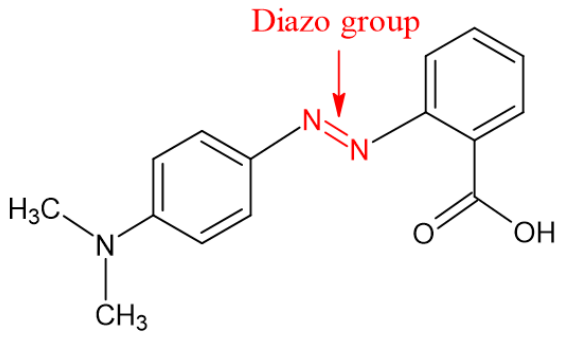

Fig. 1.1. Azo dye methyl red structure.

Photoelectrocatalysis (PEC) is a promising AOP for the degradation of POPs that combines the synergistic effect of photocatalysis and electrocatalysis oxidation techniques (Garcia-Segura & Brillas, 2017). PEC utilizes semiconductor-based electrodes (photoanodes) as cheap electroactive materials to degrade organic compounds. Techniques based on PEC for the remediation of biorefractory waters containing POPs have low physical foot-print requisites and can be easily applied in existing wastewater treatment plants (Cerrón-Calle et al., 2019).

PEC is a process that consists in the excitation of electrons upon light irradiation of a photocatalyst, forming electron/hole pairs (e^-/h^+) that can react with the media to form reactive oxygen species ($\bullet OH/\bullet O_2^-$); the recombination of these charge carriers is lowered by applying an external bias potential that directs e^- to the cathode. Organic

compounds can be oxidized by the oxidizing species, directly by h^+ or by the generated radicals (Garcia-Segura & Brillas, 2017).

$$\text{Photocatalyst} + h\nu \rightarrow \text{Photocatalyst} + e^-/h^+$$

$$h^+ + H_2O \rightarrow \bullet OH + H^+$$

$$e^- + O_2 \rightarrow \bullet O_2^-$$

$$\text{Dye} + \bullet OH/\bullet O_2^- \rightarrow \text{Degradable products}$$

For the development of high-performance electrodes for PEC water treatment, the semiconductor material must possess an outstanding e^-/h^+ separation efficiency and an exceptional electrochemical oxidation activity. Numerous semiconductors have been used for the fabrication of PEC electrodes, including TiO_2, WO_3, Cu_2O, and ZnO. Amongst these, TiO_2 is the most widely used material in PEC oxidative degradation, on account of its low cost, great chemical stability, nontoxicity, and ability to form oxidizing radicals under UV light irradiation (Liu et al., 2022).

The advantage of using nano-TiO_2 catalysts in PEC comes from the high surface area-to-volume ratio, high optical reactivity, low toxicity, and high stability (Rojviroon et al., 2021). TiO_2 nanotube arrays are of special interest because they have reported higher PEC activity due to their 3D structure with porous channels that provide a higher surface area that facilitates light harvesting through multiple-reflections and promotes light and reactant adsorption with numerous active sites (Li et al., 2016). What's more, the nanotubular structure favors the separation of photogenerated e^-/h^+ during the PEC process (Yu et al., 2023).

To enhance the efficiency of PEC degradation, the modification of the TiO_2 nanotube arrays with various materials has been studied. Amongst these, metal-organic frameworks (MOFs) have reported positive effects in PEC applications, ascribe to their high specific surface area, numerous active sites, easy functionalization, and adjustable electrochemical activity (Yu et al., 2023). MOFs are porous materials constructed of metal ions and organic ligands that can be photo/electro-redox active, making them an attractive material for PEC (Gao et al., 2021). The incorporation of the crystalline and porous MOF structure can enhance the PEC activity by acting as photosensitizers and lowering the charge carrier recombination rate. Additionally, the high surface to volume ratio of the framework can increase the number of active PEC sites, improving the efficiency of the degradation process.

In the present work, TiO_2 nanotube electrodes were synthesized by an electrochemical anodization method and a simple self-assembly solvothermal technique was applied for the deposition of MOFs from transition metals onto the electrode's surface. The TiO_2 nanotube electrodes were modified with UiO-66(Zr) and MIL-101(Fe) MOFs for the PEC degradation of methyl red as a model azo dye. The PEC activity of the MOF-modified electrode was analyzed and compared to the activity of bare TiO_2 nanotube electrodes to study the effect that the presence of the framework in the electrode structure has on its electrochemical properties.

2. Justification

The modification of nanostructures with metal-organic frameworks (MOFs) has been extensively reported and investigated to improve the photoelectrocatalytic (PEC) performance of the nanomaterials. Semiconductor/MOFs nanocomposites have shown an enhancement on the semiconductor's pristine photocatalytic activity, improving the

separation and transfer of charge carriers. To the best of our knowledge, an electrode based on TiO_2 nanotubes (TiO_2 NTs) and modified with UiO-66(Zr) or MIL-101(Fe) MOFs for the PEC degradation of dyes has not been yet reported. Nevertheless, articles have supported the theory that coupling the porous structure of the MOF onto the nanotube array can improve the PEC activity by a synergistic effect on the electrode's surface.

In their research, Guo et al. (2021) modified TiO_2 NTs with a titanium-based MOF (NH_2-MIL-125); the heterojunction showed a significant reduction in photogenerated e^-/h^+ pairs recombination, a better harvesting of visible light, faster mass transfer, and more efficient charge separation than the pure TiO_2. Further, the material proved to enhance photocathodic protection, preventing the corrosion of the composite.

The synergistic effects of hybrid MOFs and TiO_2 nanomaterials was shown by Song et al. (2019) by reporting a TiO_2 NTs electrode modified with nanoscaled NH_2-MIL-125(Ti) MOF. The electrode was used as an anode in PEC water splitting reactions, presenting an improved mechanism which suggests an enhanced light conversion efficiency, better charge separation, and improved photostability.

TiO_2/MOF heterojunctions can inhibit the recombination of photogenerated charge carriers during photocatalytic processes, thus Xue et al. (2018) synthesized MIL-125(Ti) and NH_2-MIL-125(Ti) modified TiO_2 NT arrays by solvothermal synthesis. The material showed a higher photocatalytic activity under (UV-Vis) light for the degradation of methylene blue, compared to bare TiO_2 NTs. The theories of the enhanced performance are based on the high specific surface area of the MOF and its band gap structure, in

which the valence and conduction band are more positive than that of TiO_2. Furthermore, the MOF produced a red shift of optical absorption for a narrow band gap of 2.6 eV.

You et al. (2020) deposited a bimetallic Fe/Ni MOF onto anodized TiO_2 NT arrays for PEC applications. Owning to the higher number of active sites, the composite presented an enhanced photocatalytic activity, a higher photocurrent, and good stability in photoreactions. Under UV-Vis light, the photoanode showed excellent light conversion, rapid photoresponse, and better interfacial charge separation. The coupling of the MOF with the nanotubes improved the charge carriers and electron recombination rate, presenting the material with great PEC stability.

The cooperative effect between MOFs and nanomaterials as catalysts for water remediation was proven by Mohaghegh et al. (2018) by modifying a composite based on TiO_2 NTs with MIL-88B(Fe) for the removal of pollutants from water. An Ag/TiO_2 NTs/Ti plate coated with the Fe-MOF was tested for various reactions; amongst these, the photocatalytic degradation of methyl orange dye under UV light presented the best results, showing an optimal photocatalytic activity.

Liu et al. (2017) grew the MIL-100(Fe) MOF onto a TiO_2 nanosheets substrate for visible light-driven photocatalysis, resulting in a hierarchical sandwich-like heterostructure. The introduction of the MOF efficiently improved the adsorption ability of the nanocomposite, owing to its porosity, from the tunnel adsorption of organic molecules, and its high surface area. What's more, the interface between the nanosheets and the MOF provided a platform for rapid photoexcited electron transfer, having a greater separation of photogenerated e^-/h^+ pairs. The resulting nanocomposites presented an enhanced photocatalytic degradation of methylene blue dye under visible light.

The potential of MOF materials to boost the properties of photoelectric anodes was proven by the development of TiO_2 NTs-based catalysts coupled with a NH_2-UiO-66(Zr) MOF derivative (Ar–ZrO_2) for PEC oxidation done by Zhang et al. (2023). The Ar–ZrO_2/Ti_2O_3-TiO_2 NTs system showed 95% degradation of the antibiotic tetracycline in wastewaters, showing great photoelectric synergy under visible light attributed to its high electrical conductivity and enhanced charge carrier separation and transfer.

It has been proven that the interactions between photocatalyst heterostructures govern the charge separation affecting the photocatalytic efficiency of the material. For example, a UiO-66(Zr)-NH_2@TiO_2 hollow sphere heterostructure was synthesized by Xu et al. (2023) through solvothermal grow for the reduction of Cr(VI) from wastewaters under visible light, successfully enhancing the photocatalytic activity of the TiO_2 material. The catalyst displayed good regeneration and reusability, presenting a larger absorption range of light, and repressing the recombination of e^-/h^+.

Man et al. (2022) showed the practical applications of MOF-based photocatalyst for the degradation of pollutants, proving that the photocatalytic efficiency of TiO_2 can be improved by the coupling of porous materials. In their investigation, a UiO-66(Zr)@TiO_2 nanocomposite was developed, and the addition of the MOF had a significant impact on the optical properties of the material. The improved photocatalytic activity under UV light indicates that the contact interferences between the MOF and the titanium material provides more photogenerated e^-/h^+ pairs and can promote their separation and transfer. A good stability and reusability of the catalyst was demonstrated through cycling experiments.

Photocatalytic TiO_2/UiO-66(Zr)-NH_2 nanocomposites were prepared by Zhang et al. (2020) for the oxidation of volatile organic pollutants under UV light irradiation. The Zr MOF-based composite exhibited higher photocatalytic activity and stability than pure TiO_2, TiO_2 porous nanomaterials, and pristine UiO-66(Zr)-NH_2 MOF. The PEC properties of the oxygen-rich material showed a better separation and transport of photoinduced charge carriers in the interface of both components, with an enhanced UV light harvesting and mass transfer.

Sun et al. (2020) constructed a graphene oxide nanocomposite based on UiO-66(Zr)-$(OH)_2$ MOF for the adsorptive removal of dyes and antibiotics from wastewaters, owing to the modifiable pore size and functionalization of the framework. The analysis of the adsorption of methylene blue and tetracycline hydrochloride showed spontaneous monolayer chemisorption on a heterogeneous surface. The addition of hydroxyl groups onto the MOF's structure provided more active sites for adsorption. Results showed the application of MOFs-based composites as water purification sorbents.

3. Objectives

3.1. General objective

Develop electrodes based on TiO_2 nanotubes and modified with transition metal MOFs for the enhancement of photoelectrocatalytic activity of the nanotubes for the degradation of methyl red.

3.2. Specific objectives

- Synthesize TiO_2 nanotube-based electrodes by electrochemical anodization.
- Deposit zirconium and iron MOFs onto TiO_2 nanotube substrate by a solvothermal method.

- Characterize the physicochemical properties of the electrodes using SEM, EDX, IR, Raman, and Cyclic Voltammetry to understand the composition, morphology, and electrochemical behavior of the composite material.
- Test the photoelectrocatalytic and photocatalytic capacity of the prepared electrodes in the degradation of methyl red dye.

4. Theoretical background

4.1. Nanotechnology

In 1959, Nobel Prize Laureate Richard P. Feynman set the basis for nanotechnology with his lecture titled "There's plenty of room at the bottom," where he envisioned the miniaturization of technology all the way to a molecular scale. Nanotechnology is a multidisciplinary science that studies matter at the nanoscale (1 – 100 nm). The prefix "nano" denotes a scale of 10^{-9}, thus a nanometer (nm) refers to $1.0x10^{-9}$ m. Nanostructures or nanomaterials have one or more dimensions in the nanometer scale, the interest on these materials lies on the novel physical and chemical properties matter acquires at this scale, which differ from their bulk materials (at the macroscopic scale) (Sengupta & Sarkar, 2015). Nanotechnology works at the molecular level, atom-by-atom, with the ability to create new structures based on their molecular organization. Nanotechnology can then be defined as the science and technology of objects, namely materials and devices, with an engineered structure in the nanoscale (Ramsden, 2016).

The two key concepts to understand the behavior of matter at the nanoscale are the enhanced surface-to-volume ratio (S/V) and the quantum confinement. A nanomaterial has a higher S/V than its bulk counterpart, which means that more atoms are exposed to their surroundings and more unsaturated "dangling" bonds become available at the surface, making nanoparticles more chemically active due to their higher

surface area. Quantum confinement arises from size reduction, resulting in more tightly confined electronic wave functions that change optical and electronic properties of the material. A smaller particle has a stronger confinement, enhancing its band gap and modifying the band structure. This effect influences the properties of the material, such as the electron effective mass, electron mobility, the relative dielectric constant, electric and magnetic domains, etc. Most branches of applied science and technology are being advanced in some way with the development of nanotechnology, generating new fields of research such as nanomedicine, nanobiotechnology, nanoelectronics (Sengupta & Sarkar, 2015), and nanoelectrochemistry.

4.2. Electrochemistry

Electrochemistry is a physical chemistry science that studies chemical processes that rely on charged species. An electrochemical reaction occurs when a charge transfer transpires between chemical species (Péter, 2021). Electrochemistry deals with electrical and chemical effects, mainly chemical changes caused by an electric current or the production of electrical energy from chemical reactions, when an electric potential is applied and current passes through the system (Bard et al., 2022).

Applying electrochemical methods to study chemical systems requires the understanding of the fundamental principles of reactions at the electrode's surface and the electrical properties of the electrode/electrolyte interface. Electrochemical measurements are useful to study the kinetics of the reactions happening at the electrode or to obtain thermodynamic data (Bard et al., 2022).

Electrochemical systems involve processes of charge transport across interfaces between chemical phases, usually an electronic conductor (electrode) and an ionic

conductor (electrolyte) (Bard et al., 2022). The reaction is induced or spontaneously occur through the application of a flow of electrons; this process occurs when a solution is in contact with a metal surface, or any polarizable solid surface, that allows a transfer of electrons across the interface. Usually, the solution is an aqueous electrolyte of known ionic strength and the electrode provides the polarizable surface (Collins et al., 2018).

The charge transport occurs by the movement of ions in the electrolyte and by the movement of electrons in the electrode; though in semiconductor electrodes, holes also participate in the transport. At the interface, the charge transport requires these conduction modes to be associated by an electrode reaction, having electrons and ions produced or consumed at the electrode or in the electrolyte, respectively (Bard et al., 2022). The concept of electrode implies conducting phases with different charge carrier mechanisms. The properties of the region where the transition from one conduction mechanism to another takes place condition the functionality of the electrode. (Péter, 2021).

An electrochemical reaction allows to remove or add electrons to an electroactive species (molecule or ion) in the surface of a metallic or semiconducting electrode. However, this reduction/oxidation (redox) processes usually only occur on the active sites of the surface, being just a small fraction of the electrode. For this reason, the reacting species need to be transported to the points of reaction and these processes of transport affect the reaction rate. When a reaction initiates at the electrode, it may proceed through different mechanisms involving protons and electrons at its surface or with other molecules or ions. Electrode reactions are affected by the ions and molecules' orbital structures and the band structures of the electrode material (Bard et al., 2022).

An electrochemical cell can be defined as two electrodes, a working electrode (WE) and a counter (auxiliary) electrode (CE), separated by an electrolyte phase. The analytical reaction takes place at the surface of the WE (cathode), meanwhile the CE (anode) is needed for the current flow, being the current-supporting counterpart of the working electrode (Harris, 2016). Electrolytes are usually liquid solutions containing ionic species where the solvent-electrolyte system is sufficiently conductive to be useful in an electrochemical cell (Bard et al., 2022).

The electrodes are generally not at the same electric potential and electrons move from the more negative electrode to the more positive one, this way a chemical reaction can be supported in the cell. An electrode reaction produces electrons at the negative electrode that go to the positive electrode where they are consumed for another reaction. The overall chemical reaction in the cell is constituted from independent half-reactions that describe the chemical changes at the two electrodes (Bard et al., 2022). Electrochemical cells are based on ion motion and accumulation on the surface of an electrode. The electrochemical process and the overall dynamics of the system are controlled by a complex interplay of molecular properties of ions and the dimensions of the cell (Taner Camci et al., 2023).

To control what electroactive species react at an electrode, the potential of the WE should be modulated. The potential of an electrochemical cell may be regulated by using a three-electrode configuration, where a reference electrode (RE) is introduced to measure the potential of the WE. A metal electrode is polarizable, meaning that its potential is easily changed with small currents flow. A RE, such as Ag/AgCl or Hg/Hg_2SO_4, is not polarizable, so its potential only varies under a significant current flow. Thus, it is possible to measure the potential of a polarizable WE with respect to the no polarizable RE.

Current flows between the WE and the CE, while the current that flows through the RE is negligible, having a constant potential. The potential difference between the WE and the RE can be regulated by a potentiostat (Harris, 2016).

In the bulk electrolyte, it can be assumed that the electrolyte ions and solvent molecules are arranged randomly and homogenously since the forces acting on them are equal in all directions (on average). Nevertheless, the interactions in the electrode/electrolyte interface differ from those in the bulk electrolyte. Being the electrode a charged surface, in the interface the forces that act on the electrolyte particles are anisotropic, producing a new arrangement of ions and solvent molecules with different dipoles forming an electric double layer. Because of the formation of the double layer, a potential difference is generated across the interface (Collins et al., 2018).

The electric double layer is a complex structure that forms when a charged electrode comes into contact with the electrolyte. The solvent molecules are adsorbed onto the electrode's surface, creating the inner Helmholtz plane, and electrostatic forces make ions approach the charged surface as close as possible, while maintaining their solvation shell, this closest approach place is called creating the outer Helmholtz plane. If ions lose their solvation shell, they become adsorbed into the electrode's surface where a redox reaction can take place. The transition zone between the double layer and the bulk electrolyte is referred to as the diffuse layer, where there is a distribution of ions and charge as a function of distance from the surface of the electrode, producing an exponential decrease of the electric potential (Collins et al., 2018).

4.3. Nanoelectrochemistry

Nanoelectrochemistry focuses on electrode structures with lateral dimensions below 100 nm, studying systems that involve electron transfer mechanisms. The motivation of developing this science lies in the fundamental phenomena that one can gain through nanoelectrodes, inaccessible at the macro-scale. Some issues that we encounter are the critical dimension an electrode can reach and the number of molecules that are probed at the surface (Eliaz, 2012). Nanomaterials have special geometries, such as nanotubes or nanowires, unique bonding patterns, and quantum effects that dictate their electronic properties (Mirkin & Amemiya, 2015). The ability to manipulate matter at the nanoscale allows to develop materials with a controlled composition and structure (Lavacchi et al., 2013).

One of the main advantages that nanomaterials offer in electrocatalytic applications is a greater surface area. The surface area is of great importance in electrocatalysis since electrochemical reactions usually take place on the surface of the electrocatalysis. The increase of the electrode-electrolyte interface results in a decrease in the energy required for the electrochemical reaction, representing a positive impact on energy efficiency. (Lavacchi et al., 2013). A greater surface area signifies a more reactive material, obtaining a higher electrocatalytic activity. Furthermore, the increased efficiency of a nanostructured catalyst can be explained by the reduced transfer time of the intermediate from one active site to another (Péter, 2021). An intrinsic problem of nanomaterials is their stability, which is often low as a natural consequence of their high reactivity. The practical use of nanostructures as catalysts is generally restrained by how long or how many times it can be employed (Mirkin & Amemiya, 2015).

Nanoscience not only revolutionized electrochemistry by developing novel electrode systems, but also helped developed analytical chemistry, giving molecular knowledge about heterogeneous process properties and an analysis of electrode's surface (Mirkin & Amemiya, 2015).

4.4. Semiconductors

The band gap (E_g) of a material is defined as the difference in energy between its valance band (HOMO) and the conduction band (LUMO). Materials can be classified according to their band gap (Ameta et al., 2018):

- Conductor or metal: $E_g < 1.0$ eV
- Semiconductor: $E_g < 1.5 – 3.0$ eV
- Insulator: $E_g > 5.0$ eV

In semiconductors, the atom's orbitals are so close that they overlap, presenting almost continuous regions of energy that forge the electron energy bands. Two characteristic energy bands, the valance band (of lower energy) and the conduction band (of higher energy), are separated by the band gap energy (Bessegato et al., 2015). If a semiconductor material has an excess of electrons, being negatively charged, it is classified as an *n*-type (extrinsic) semiconductor. If the semiconductor has an absence of electrons (holes), it will be positive charged and referred to as a *p*-type (intrinsic) semiconductor (Sharon, 2016).

The main difference between a semiconductor and a metal is that a semiconductor provides both the conduction band and the valence band for electro transfer reactions, whilst metals do not have different energy levels, having only one energy platform (Fermi

energy level) that is an equivalent to the position of the conduction and valence band levels (Sharon, 2016).

At 0 K, a semiconductor turns into an insulator because the valence band is fully occupied, and the conduction band is empty. The Fermi level lies within the band gap, and it corresponds to the energy of the highest filled state at 0 K. Hence, the generation of charge carriers is needed for the material to become conductive. Charge carriers (e^-/h^+ pairs) are usually formed by photoexcitation, by irradiating the semiconductor's surface by light with an energy equal or higher than its band gap, promoting electrons from the valence band to the conduction band. The use of charge carriers in chemical reactions is limited to the recombination of e^-/h^+ pairs, having a low photonic efficiency (Bessegato et al., 2015).

To improve the charge separation on the space charge layer, a bias potential can be applied to control the Fermi level, easing the reactions of charge carriers on the surface of the semiconductor. In an *n*-type semiconductor, such as titanium dioxide (TiO_2), when the applied potential is greater than the flat band potential (the potential where there is no space charge layer and the bands are flat) electrons are depleted and holes are improved in the semiconductor's surface, increasing the band bending. If the potential applied is equal to the flat band potential, the bands will be flat and the carriers would recombine. Under irradiation, the photogenerated holes on the surface promote oxidation of reduced molees that have a formal potential more negative than the valence band of the semiconductor (Bessegato et al., 2015).

In a semiconductor-electrolyte interface, electrons and holes can react with either the semiconductor, behaving like an active electrode, or with the redox electrolyte, behaving

like an inert electrode. When the electron transfer reaction occurs in the semiconductor, it is called a corrosion reaction. However, if the semiconductor is inert to the electrons or holes but allows the redox electrolyte to undergo an electrochemical reaction, the semiconductor is considered electrochemically stable (Sharon, 2016).

The interface between a semiconductor and a redox electrolyte produces a Schottky junction that causes a change in the electrochemical potential of the semiconductor (Fermi level) to reach an equilibrium. This adjustment generates a band bending within the semiconductor phase, the amount of bending is proportional to the difference of the Fermi levels of the semiconductor and the electrolyte. The space charge layer, or depletion layer, is the region where the bending occurs and it is characterized by the depletion of the majority of charge carriers, electrons in *n*-type semiconductors and holes in *p*-type semiconductors (Bessegato et al., 2015).

4.5. Electrocatalysis

Electrocatalysis is a branch of electrochemistry that studies reactions where electrical energy is converted to chemical energy by using catalytic material (Lavacchi et al., 2013). The electrocatalysis energy conversion mechanism is based on chemical bond formation, with a high transformation efficiency (up to 100% Faradic efficiencies) in comparison to the low quantum yield of photocatalysis. Electrocatalytic reactions can be controlled by modulating the applied electric potential. Most of the reported catalysts for electrocatalysis are based on noble metals, being high-cost and scarce, thus limiting their applications. For this reason, the development of electrocatalysts based on Earth-abundant metals is of great interest (Gao et al., 2021).

To increase electrocatalytic properties, it is important to focus on the development of new electrode architectures. The main characteristics that dictate the electrocatalytic activity of an electrode are composition, surface structure and morphology. The design of the electrode's material can improve the rate of the electrochemical reaction, making the process more efficient (Lavacchi et al., 2013). Here is where nanotechnology comes in, offering novel materials to develop electrodes with enhanced properties to increase their electrocatalytic activity.

An efficient electrocatalyst should have a high electrical conductivity, plenty active sites, and good charge transfer and separation. Traditional electrocatalysts are usually based on precious metals, being expensive and having poor stability. More accessible materials have been studied for the development of electrocatalysts, such as semiconductive composites (Gao et al., 2021).

4.6. Photocatalysis

Photocatalysis is a chemical process where a photocatalyst and light are needed to carry out or accelerate a reaction, where an electron/hole (e^-/h^+) pair is generated after exposing a semiconducting material to light (Moura & Picão, 2022). The term photocatalyst is composed of two words: "photo," related to photons, and "catalyst," meaning a substance that affects the rate of a reaction; thus, a photocatalyst is a substrate that can absorb light and consequently alter the rate of a chemical reaction. Photocatalysis converts solar energy into chemical energy and these reactions can be classified based on the physical state of the reactants: it is a homogeneous photocatalysis if both the catalyst and the reactant are in the same phase and a heterogeneous photocatalysis if they are in different phases (Ameta et al., 2018).

Semiconductors can conduct electricity even at room temperature in the presence of light, acting as photocatalysts. When a photocatalyst is irradiated with light of sufficient energy (greater than the semiconductor's bandgap), the energy of the photons is absorbed by electrons (e^-) in the valence band and are promoted to the conduction band, as a result of electron excitation. This process generates a hole (h^+) in the valence band, creating an e^-/h^+ pair in a photo-excitation state. The excited electron is then used to reduce an acceptor molecule and the hole to oxidate a donor molecule; here is where the importance of photocatalysis lies, this process provides an oxidation and a reduction environment simultaneously (Ameta et al., 2018).

The free e^-/ h^+ pairs generated from the absorption of light in a semiconductor across its band gap are charge carriers that can react with their environment when they reach the surface of the semiconductor (Grundmann, 2016). These charge carriers are in an unstable excited state and tend to return to their ground state in picoseconds due to recombination reactions (Cerrón-Calle et al., 2019). If an e^-/h^+ pair recombines, it loses its catalytic activity; hence, the efficiency of the photocatalytic activity of a semiconductor depends on its efficiency of charge separation; for this reason, semiconductor surfaces must present a small density of recombination centers. Small structures typically exhibit more efficient charge-carrier separation due to their large surface-to-volume ratio, having a greater opportunity for the charge carriers to interact with the surface. Additional charge carriers cause an increase in the conductivity of the material (Grundmann, 2016).

The basic principle of a photoinduced process at a semiconductor/electrolyte interface is the transportation of the e^-/ h^+ pairs to the interface where they react with the adsorbed molecules in the surface of the electrode (Aliofkhazraei & Makhlouf, 2016).

Electrons at the surface can be donated and reduce electron acceptors (A), usually oxygen, and the holes can oxidize donor species (D) (Grundmann, 2016).

In aqueous solutions, highly reactive hydroxyl radicals are formed due to a charge exchange at the valence band with the vacancies ($H_2O + h^+ \rightarrow \bullet OH$) and superoxide anions are generated by the reduction of dissolved molecular oxygen by the excited electrons at the conduction band ($O_2 + e^- \rightarrow O^-_2$). These hydroxyl radicals and superoxide anions have the capacity to oxidize virtually all organic materials to CO_2 and H_2O (Aliofkhazraei & Makhlouf, 2016), being capable of attack and detoxify organic pollutants in aqueous solutions (Grundmann, 2016).

Photocatalysts should feature three main properties: an appropriate bandgap, a good distribution of active sites, and an efficient charge transfer and separation. Semiconductor systems are often employed as photocatalyst; however, traditional semiconductors endure a limited bandgap, low charge carriers' separation, and low catalytic activity. Nevertheless, these issues can be addressed by doping or modifying the structure of the semiconductors (Gao et al., 2021).

Photocatalytic cells present many advantages since they operate under mild reaction conditions, have a fast reaction rate and a simple process operation. One drawback, however, is the rapid recombination of e^-/h^+ pairs, but this issue can be addressed by doping modifications or heterojunctions (Jia et al., 2020). The main feature to improve in hybrid photocatalytic systems is the level of interaction between the component materials and the efficiency of the co-catalysts (Dong et al., 2021).

Photocatalysis is an environmental-friendly technique that has been employed for water splitting, photoreduction of CO_2, organic synthesis and photodegradation of

contaminants, being an alternative or complementary technology for the treatment of wastewaters (Gao et al., 2021; Hariganesh et al., 2020). Since photocatalytic reactions are usually regulated by mechanisms of free radicals (•OH, $•O_2^-$, $H_2O•$), they are considered as an indiscriminative process, particularly in water (Hadi Dehghani et al., 2022).

4.7. Photoelectrocatalysis (PEC)

Electrochemistry assisted photocatalysis, or photoelectrocatalysis (PEC), is a chemical technique that improves heterogeneous photocatalytic processes by applying a biased potential to a photoelectrode with a supported catalyst. PEC techniques are based on the separation of photogenerated e^-/h^+ pairs by a gradient potential. The applied potential causes photogenerated electrons to flow through an external circuit to the counter electrode, improving the efficiency of the PEC method (Bessegato et al., 2015).

When a PEC system is irradiated with light equal or greater than the band-gap energy of the semiconductor, the electrons in the semiconductor surface are excited from the valence band (VB) to the conduction band (CB), leaving holes (h^+) in the VB and excited electrons (e^-) in the CB (Liu et al., 2022). Subsequently, a positive potential directs e^- to the counter electrode while h^+ reacts with H_2O/OH^- to generate highly oxidizing hydroxyl radicals (●OH). In the cathode, adsorbed O_2 molecules act as e^- acceptors to form superoxide ions ($●O_2^-$). Both species are capable of degrading aromatic compounds, such as dyes, through oxidation. The advantage of using PEC over photocatalysis lies on the application of a potential across the photoanode, where the catalyst is supported, allowing a more efficient separation of the photogenerated charge carriers (e^-/h^+) and increasing their lifetime (Ferraz et al., 2013).

A photoelectrode is based on a semiconductor attached to a conductive substrate that, when irradiated with energies equal or higher than the semiconductor's band gap energy, generates e^-/h^+ pairs that can be separated by potential gradients that are established at the interface of the electrode and the electrolyte. The applied anodic potential bias generates a simultaneous potential gradient inside the photoelectrode (photoanode), forcing the photogenerated electrons to move to the counter electrode, separating the photogenerated holes (Jia et al., 2020). The imposition of a difference of potential during photoexcitation induces the separation of the photogenerated charge carriers, minimizing their recombination (Cerrón-Calle et al., 2019). PEC configurations offer a higher effectivity of photogenerated charge separation, because the light irradiation has higher energy than the band gap of the semiconductor, increasing the lifetime of the photogenerated e^-/h^+ pairs (Bessegato et al., 2015).

This type of catalysis fully employs the combined synergistic principle of electrocatalysis (electricity) and photocatalysis (light) (Devi et al., 2023). Additionally, it counts with a great recycling efficiency of the catalyst, in comparison with powder catalysts, which are challenging to recover. A photoanode is typically constructed by coating a conductive plate with a powder catalyst to form a bulk electrode, decreasing dispersion, and improving the mass transfer rate (Jia et al., 2020). PEC is a multidisciplinary field, involving surface material science, electrochemistry, solid-state physics, and optical physics (Bessegato et al., 2015).

In 1972, Fujishima & Honda discovered the relation between electrochemistry and light-driven semiconductors by conducting the photolysis of water using a TiO_2 electrode without any external bias potential. The sequential reports on water photolysis

and the photoconversion of small organic molecules using semiconductors open the path to other PEC applications (Sharon, 2016).

A PEC process usually involves a system of three electrodes: a working electrode (WE), a counter electrode (CE), and a reference electrode (RE). The WE is based on a photo-electrocatalytically active material (semiconductor). Semiconducting materials need to have a band gap that corresponds to the incident light radiation. When light hits the WE, e^-/h^+ pairs are generated that drive redox reactions; hence, the electrical energy drives the chemical process. A critical factor that limits the photocatalytic efficiency (the conversion efficiency of light to chemical energy) is the recombination of photogenerated e^-/h^+ pairs, which also produces unwanted heat. This recombination can be prevented by applying a differential potential, obtaining a higher magnitude current. The RE is used to quantify the current generated in the system, this current can be used to quantify the efficiency of the PEC process. A CE, usually a metal wire, completes the circuit (Devi et al., 2023).

PEC oxidation occurs when using an *n*-type semiconductor, and a PEC reduction takes place when using an *p*-type semiconductor. Photogenerated holes on the semiconductor surface are used for oxidation reactions and the electrons that flow to the counter electrode generate the reduction reactions. Hence, charge carriers recombination is minimized, improving the quantum yield of the PEC process (Bessegato et al., 2015). For PEC applications, a semiconductor must be electrochemically stable in order to have the electron transfer occur only with the electrolyte (Sharon, 2016). In catalysis, the surface of a semiconductor is especially important because it is subject to interaction with the chemistry of its environment (Grundmann, 2016).

Many low-cost and environment-friendly semiconductors with high stabilities, such as TiO_2, have been utilized as catalysts for different photoredox reactions (Gao et al., 2021). The extensive use of semiconductors in PEC applications arises from their versatility and their capacity for generating electrons, holes, hydroxyl radicals, and/or superoxide radicals (Bessegato et al., 2015). An advantage that semiconductor-mediated PEC presents is that it helps to overcome problems related to the fast charge recombination of the catalysts (Ameta et al., 2018). The applications of a semiconductor material depend on its capacity to generate electrical power, which in turn depends on electron transfer properties (Sharon, 2016).

PEC processes have been well studied for environmental remediation; being a clean, low-cost, and environmental-friendly technique for the removal of pollutants (Zhong et al., 2020). One of the main challenges in PEC is the development of stable semiconductor materials that can be activated by solar irradiation (Bessegato et al., 2015).

The efficiency of PEC processes can be optimized by modifying the properties of the photoactive material. One of the most used techniques is to engineer the bandgap of the semiconductor by varying the composition, shape, size, or anisotropy by synthesizing composites with other materials. These composites could also increase the lifetime of e^-/h^+ pairs, making them available for a longer period of time for redox reactions (Devi et al., 2023).

In PEC, the most reported catalysts are TiO_2, ZnO, CeO_2, CdS and ZnS. With TiO_2 having a maximum yield with the simplest performance (Aribam et al., 2022).Recent developments in PEC have been achieved thanks to advances in material science, especially in nanomaterials. Highly ordered nanomaterials, such as nanotubes, nanowires,

nanofiber, etc., have been rigorously studied mainly due to their high surface area and excellent electronic transport (Bessegato et al., 2015).

4.7.1. PEC degradation

PEC degradation of pollutants is considered one of the most promising technologies for the harness of solar energy to address the water pollution problems around the world (Gao et al., 2021). In PEC, nontoxic semiconductors are employed to eliminate pollutants present in waste waters. This technique includes transfer, adsorption, degradation, and removal of the pollutant at the interface of the semiconductor (Aribam et al., 2022). PEC processes have been thoroughly applied for water treatment because of their high removal efficiency when degrading and mineralizing organic pollutants to intermediate products, CO_2, or H_2O. They are considered environmentally friendly, compared to other physical and chemical approaches, since PEC does not usually release harmful residues or transform the contaminants to another phase (Xiong et al., 2022).

PEC degradation is categorized as an advanced oxidation process, which is a method for the degradation of pollutants by oxidation with hydroxyl radicals. Hydroxyl radicals (●OH) are nonselective and highly oxidizing species, being able to mineralize organic compounds. In the valence band, the oxidizing nature of the photogenerated holes generates hydroxyl radicals by the oxidation of H_2O molecules or OH^- ions adsorbed onto the semiconductor's surface, being also able to directly oxidize organic molecules (Bessegato et al., 2015) The mineralization of organic pollutants to species like CO_2, NH_4^+, NO_3^-, or SO_4^{2-}, takes place by the formation of O_2^-, HOO•, or OH• through a multistep reduction (Ameta et al., 2018)

In order to achieve a maximal degradation efficiency, the catalyst must have an adequate band gap, rapid charge separation, high quantum yield, and a large surface area to improve the photocatalytic activity (Aliofkhazraei & Makhlouf, 2016). Because of their structure, semiconductors act as sensitized catalysts for photoredox processes, some of them being able to photocatalyze the degradation of organic pollutants like aromatics, halo hydrocarbons, insecticides, pesticides, surfactants, and dyes. Nanostructured semiconductors have been used in organic compound oxidation, CO_2 reduction, anion reduction, hydrogen generation, disinfection, and electrosynthesis through PEC processes (Bessegato et al., 2015).

4.8. Titanium dioxide materials

Titanium dioxide (TiO_2) is a wide band-gap inorganic semiconductor that can be used as a functional material for photovoltaic and photocatalysis applications (H. Yang & Fei, 2017). TiO_2 has a band gap of about 3.2 V suitable for high photocatalytic activity, allowing the use of UV light for PEC applications (Aliofkhazraei & Makhlouf, 2016). Large band gap materials, such as TiO_2, are highly stable both in acidic and basic media and for both *p*-type and negative *n*-type electron carriers. TiO_2-based materials are widely used for their high stability, biocompatibility, abundance in earth, and low cost, it has been studied for its applications in fuel conversion, biomedicine, and environmental cleanup (Sharon, 2016).

TiO_2 is a compound that presents three crystal structures: rutile, anatase and brookite. From these, anatase and brookite have the higher photocatalytic activity, but the brookite type is very unstable. In anatase and brookite, the TiO_2 ions are in the octahedral center formed by six adjacent O^{2-} ions. The main difference between these two types is the combination mode of the octahedral structures, which leads to different densities and

bad structures. The mass density of rutile is slightly higher than anatase, 4.250 g/cm^3 and 3.894 g/cm^3 respectively, and the energy band gap of anatase (3.14 eV) is slightly lower than that of anatase (3.3 eV) (Li, 2020). Generally, anatase is more active in photocatalysis than rutile; this difference is mainly due to the transport of excitons to the surface (Luttrell et al., 2014). Further, the anatase type has a longer lifetime of charge carriers because anatase belongs to the indirect band gap semiconductors. On the other hand, electron traps in rutile are often too deep for photogenerated electrons to participate in reactive oxygen species generation reactions, causing a low generation and a high recombination rate of charge carriers (Žerjav et al., 2022).

On account of its great mechanical properties, excellent chemical and thermal stability, high corrosion resistance, availability, low cost, environmentally friendly, and nontoxicity, TiO_2 is a promising material for hydrogen production by water splitting, photocatalytic reduction of CO_2, and photocatalytic degradation of organic contaminants (Dong et al., 2021). Heterogeneous binary metal oxide photocatalysts, such as TiO_2, have been extensively studied for the removal of organic-colored pollutants. Specifically, TiO_2 has been used to fully oxidate, detoxify and mineralize dyes in aqueous solutions under UV light irradiation, such as methyl red, methylene blue, Congo red, crocein orange G, to name a few (Ameta et al., 2018).

TiO_2 is one of the most used materials for PEC applications due to its long e^-/h^+ pair lifetime, compatible energy position of its valence and conduction band, and its superior catalytic stability, compared to other photoelectrocatalysts such as WO_3, ZnO, CdS, Fe_2O_3 and SnO_2. Further, the band-edge position of TiO_2 relative to water oxidation allows the formation of hydroxyl radicals, being a potent oxidant for the PEC degradation of organic pollutants in water (Bessegato et al., 2015). TiO_2 is an *n*-type semiconductor

with a valence band with a high enough potential for oxidizing H_2O and OH^- to hydroxyl radicals (Bessegato et al., 2015).

Binary metal oxide combinations alter the materials' capacity to harvest solar radiation, affecting the PEC activity. TiO_2 has been considered as the best semiconductor for PEC because of its low band gap, stability, durability, reusability, etc., and its composites usually report higher efficiency than the individual semiconductor (Ameta et al., 2018). Using TiO_2-based electrodes for PEC is a powerful advanced oxidation process that can oxidize virtually all organic contaminants by reactive oxygen species, without producing damaging end products (Xiong et al., 2022). Hybrid TiO_2 photocatalysts have shown improved PEC activity, boosting TiO_2 photocatalytic properties. Photocatalysis with hybrid TiO_2 materials is a nontoxic and cost effective approach for environmental cleanup (Chimmikuttanda et al., 2022).

The major drawback of using TiO_2 in photocatalysis is its wide band gap (3.0 – 3.3 eV), being active only in the UV region. The solar spectrum consists of only about 4% of UV light ($\lambda < 387$ nm). Developing photocatalysts with an extended photo-response to the visible region would allow to make use of 55% of solar light (Nyamukamba et al., 2017).

One of the most studied applications of TiO_2 materials is the PEC degradation of organic pollutants in water because they endow a one-way channel for the transfer of photoexcited electrons, as a result of their ordered porous arrangements and a great internal surface area (Song et al., 2019). Fujishima & Honda reported for the first time, in 1972, the use of TiO_2 surfaces for the degradation of toxic pollutants through light-induced water electrochemical photolysis. The interest of using TiO_2-based electrodes for

organic compound decomposition comes from the strong oxidizing power of the semiconductor, along with a long-term stability and low-cost preparation (Aliofkhazraei & Makhlouf, 2016).

4.9. Titanium dioxide nanotubes (TiO_2 NTs)

Nanomaterials in PEC have been studied as smart materials for water treatment due to their high surface area, morphological features, discrete quantum influences, and unique physical chemical properties, having distinct electric and optical behaviors. Nanophotocatalysts have a high oxidizing capacity, generating oxidizing species that are able to degrade various compounds under light irradiation (Fakhri et al., 2022).

Titanium-based materials present interesting characteristics such as highly efficient photoconversion, longevity, and low cost, which turns them into an interesting material for PEC applications. The dimensional morphology of titanium can enhance the performance of the material in specific applications; its morphologies at the nanoscale include nanotubes, nanofibers, nanorods, nanoflowers, and their nanocomposites (You et al., 2020). Titanium nanoarrays are an ideal electrode material for PEC sensing, yielding a large active surface area that augments activity and accelerates surface reactions. The open space between the nanoarray enhances the diffusion of active species on its surface. Based on the electron transfer theory, nanoarrays can promote electron flow and, because they are in direct contact with the conductive substrate, they ensure a good electron transportation and the ability to immobilize an active material on the electrode surface (You et al., 2020).

TiO_2 nanomaterials present a higher photocatalytic efficiency compared to their bulk counterparts, owing to their light-harvesting capacity (Song et al., 2020). Different

nanostructures of TiO_2 have been studied for the degradation of organic pollutants due to their high photochemical stability, non-toxicity, low cost, and simple preparation (Mohaghegh et al., 2018).

Titanium dioxide nanotubes (TiO_2 NTs) are one-dimensional nanostructures that followed the discovery of carbon nanotubes done by Iijima in 1991. TiO_2 NTs offer vast free space, both in the interior of the tube and in the outer area, that can be functionalized with active materials, namely semiconductors, oxides, and noble metals (Zhou et al., 2021). The nanotubular structure provides a faster electron transportation rate and a lower recombination of photo-generated carriers (Xue et al., 2018). TiO_2 NTs have an open tube structure; in this manner, substrates can easily reach photocatalytic-active sites, allowing the attachment of functional guest molecules (Song et al., 2020). Even though TiO_2 NTs endure a higher photocatalytic activity compared to that of nanoparticulated TiO_2 films, their specific surface area is lower than the one of TiO_2 nanoparticles (Xue et al., 2018).

For PEC applications, the photosensitizer must possess an adequate surface area and porosity; for this reason, TiO_2 NT arrays have been rigorously studied for PEC reactions, owning to their excellent electrical conductivity (Mohaghegh et al., 2018), ion-changeable capacity, and photocatalytic activity (Aliofkhazraei & Makhlouf, 2016).

Unfortunately, TiO_2-based nanostructures present certain disadvantages in their practical applications as anodes for photocatalytic degradation and detection, facing the intrinsic drawbacks of bulk TiO_2. Similar to TiO_2 particles, TiO_2 NTs have a wide energy band gap (3.0 eV for rutile and 3.2 eV for anatase) that can only be irradiated by UV light, thus not presenting absorption of visible light, undermining the solar energy conversion efficiency in photocatalytic processes (Song et al., 2020). Moreover, TiO_2 NTs exhibit a

rapid recombination of photo-generated chargers (excitons) because of its short diffusion paths of charge carries, limiting their use under solar energy (Dong et al., 2021).

To overcome the traditional issues of TiO_2-based photocatalysis, functionalization methods can be applied to increase photocatalytic activity by reducing the energy band gap and retarding the recombination of e^-/h^+ pairs; this functionalization methods include doping with metals or non-metals, dye sensitization, or semiconductor coupling (Mohaghegh et al., 2018). TiO_2 composites can be doped or coupled with other nanomaterials that have a narrower band gap energy to extend its spectral response to the visible light spectrum (Song et al., 2020). The incorporation of extension materials have been extensively studied for the modification of TiO_2 NT arrays to enhance their photocatalytic activity (Zhou et al., 2021).

4.9.1. Electrochemical synthesis of TiO_2 NT arrays

Several methods have been reported for the synthesis of TiO_2 NTs, such as assisted-template method, hydrothermal treatment, or electrochemical anodization (anodic oxidation) (Aliofkhazraei & Makhlouf, 2016); **Table 1.1.** shows a brief comparison between the three methods.

Table 1.1. Comparison of usual TiO_2 NT array synthesis methods (Aliofkhazraei & Makhlouf, 2016).

Synthesis method	**Crystal structure**	**Distribution**	**Advantages and disadvantages**
Template-assisted	Amorphous, crystalline	Ordered, vertically aligned	Prefabrication and post-removal or templates, impurities
Hydrothermal treatment	Titanate, anatase	Random	Strong alkaline solution, high pressures
Electrochemical anodization	Amorphous, anatase	Ordered, vertically aligned	Simple and efficient for robust, pure TiO_2 NTs

Electrochemical anodization is a simple synthesis technique, performed in electrolytes containing small amounts of fluoric ions, that allows to control the synthesis of vertically aligned and highly ordered TiO_2 NT arrays, obtaining a high aspect ratio and a pure-phase TiO_2 structure under environmental conditions (Aliofkhazraei & Makhlouf, 2016). TiO_2 NT-based electrochemical sensors present various advantages over TiO_2 bulk materials; TiO_2 NTs prepared by electrochemical anodization can be employed as a PEC platform, amplifying the detection signal of the sensor (Zhou et al., 2021).

Anodizing thin titanium sheets to induce the formation of horizontal and perpendicular structured TiO_2 NTs on the sheet's surface improves electron transfer, enhancing the photocatalytic activity of the material (Rojviroon et al., 2021). TiO_2 NT arrays synthesized through electrochemical anodization of titanium sheets exhibit a unique combination of geometry and functionality (Xue et al., 2018); this synthesis method was first reported by Zwilling et al. in 1999, who used an aqueous hydrofluoric acid electrolyte to anodized titanium, obtaining self-ordered TiO_2 NTs arrays. In a more practical sense, high aspect ratio TiO_2 NTs were first obtained by Macák et al. in 2005, using an organic electrolyte. Owning to their distinct tubular features, high specific surface area, high pore volume, biocompatible, anticorrosion, well-oriented charge transfer route, and regular arrays that are perpendicular to the substrate surface; TiO_2 NT arrays obtained by electrochemical anodization have wide applications in areas like photocatalysis, sensing, biomedicine, etc. (Zhou et al., 2021).

The electrochemical anodization of TiO_2 NTs is basically a selective etching process, being a competition between different physical and chemical reactions, such as anodic oxide formation, chemical dissolution, and complexation. The anodization process can be

explained by three main steps: oxide layer growth, field-assisted oxide dissolution, and chemical oxide dissolution by the fluoride acidic electrolyte (Li et al., 2014).

First, an oxide layer grows on the surface of the metal plate due to the interaction between the titanium and the oxygen ($Ti_{(s)} + O_{2(g)} \rightarrow TiO_{2(s)}$). The applied potential polarizes the Ti-O bond, weakening it and facilitating the dissolution of the Ti^{+4} and O^{2-} ions. The oxygen anions then migrate through the oxide layer to the metal/oxide interface where they keep reacting with the metal, and the titanium cations dissolve into the fluoride acidic electrolyte, forming TiF_6^{2-} anions. The growth of the oxide layer is dominated by the migration of the Ti^{+4} and O^{2-} ions in the growing compact layer (Li et al., 2014).

The surface of the oxide layer is locally activated and starts to dissolve, producing the random growth of pores. The barrier layer at the bottom of the pores becomes thinner, increasing the electric field intensity, resulting in further pore growth. The nanotubes start a steady growth when the rate of TiO_2 formation is almost equal to the rate of TiF_6^{2-} formation and dissolution (Li et al., 2014).

The structure and morphology of TiO_2 NT arrays can be modified by adjusting some key parameters during the electrochemical synthesis, including composition/shape of the titanium substrate, type of electrolyte, fluoride concentration, temperature, pH, anodization voltage, current, reaction time, and other anodization parameters. Controlling these parameters can influence features such as grow rate, tube diameter and length, wall thickness, and crystallinity. Moreover, annealing post-treatment or modification of the nanotube arrays govern the final characteristics and the performance of the TiO_2-based device. Annealing the NT array changes the crystalline structure, affecting the conductivity and the lifetime of charge carriers; on the other hand, modifying the arrays

with other elements can decrease the band gap of the semiconductor material (Aliofkhazraei & Makhlouf, 2016).

The two main experimental parameters that regulate the morphology of TiO_2 NTs synthesized by electrochemical anodization are the nature of the electrolyte used and the anodization voltage applied. Depending on the type of electrolyte employed, the TiO_2 NTs can be classified in four generations: first generation include inorganic aqueous electrolytes based on hydrofluoric acid, second generation are buffered electrolytes based on fluoride ions, third generation are organic electrolytes with fluoride salts, and fourth generation consist of fluoride-free electrolytes. Each electrolyte provides unique geometrical features and surface properties (Aliofkhazraei & Makhlouf, 2016).

Third-generation electrolytes allow the synthesis of smooth and taller nanotubular structures, to the regime of hundreds of micrometers. The length of the nanotubes is mainly determined by a steady-state situation between the electrochemical formation of TiO_2 at the tip of the pore and its chemical dissolution by fluorides from the electrolyte. The pH at the tip of the pore is lowered by the hydrolysis reactions of the Ti^{4+} formed during the anodization and the Ti^{4+} flux can be controlled by the current applied. Therefore, we can maintain the pore tip adequately acidic meanwhile the pore walls dissolve much more slowly, allowing the nanotube to grow to higher lengths (Aliofkhazraei & Makhlouf, 2016).

The anodization voltage strongly affects the morphology of the nanostructure formed. For example, at low voltages (<5.0 V) nanopores will form instead of nanotubes, but at high voltages (>50 V) sponge-like structures are formed because of break-down events inside the nanotube. The anodization voltage regulates different aspects of the synthesis,

such as the transition from porous TiO_2 to nanotubes, also affected by water content, the rate of growth, length and crystallization, and the diameter of the nanotube, which is linearly proportional to the voltage (Aliofkhazraei & Makhlouf, 2016).

4.10. Metal-organic frameworks (MOFs)

MOFs are a novel multi-dimensional ultra-porous material with exceptionally high crystallinity and accessible surface area, being categorized as a subclass of polymers (H. Yang & Fei, 2017). The official IUPAC definition of MOFs is a coordination network with organic ligands containing potential voids (Batten et al., 2013). MOFs are composed of a self-assembly of metal ions or clusters linked to organic ligands by coordination bonds, forming an ordered microporous structure with chemical functionalities that provide spatial and electronic structural diversity (Song et al., 2020).

The electronic and optical structure of MOFs can be modulated without changing its crystalline structure, by doping with metal ions or functionalization of the organic ligands. The pore size and pore environment of a MOF can also be modified, improving the selectivity of the material (Gao et al., 2021).

Thanks to their unique properties, such as large surface area, high porosity, adjustable pore size and shape, open-framework structure, tunable chemical composition, easy functionalization, and specific electrochemical catalytic performance, MOFs have a wide range of applications, including gas storage/separation, drug delivery, chemical sensing, molecule separation, pollutant sequestration and applications in biomedicine, energy, catalysis, etc. (Zhou et al., 2021; H. Yang & Fei, 2017). Fabrication of electronic and optoelectronic devices can be achieved by growing MOF films onto conductive substrates, supercapacitors, photovoltaic materials, and electrocatalysts (H. Yang & Fei,

2017). Furthermore, MOFs are a promising electrode material in the field of electrochemistry, they have been studied as rechargeable batteries, supercapacitors, fuel cells, and for PEC applications (F. Yang et al., 2018).

4.10.1. MOFs in PEC applications

Mainly due to their large surface area, high porosity, and easily tunable optical and electronic properties, MOFs are ideal materials for PEC applications. Given that metal ions/clusters and even some organic ligands in MOFs are photoelectron-redox active. MOFs' structure provides intrinsic pores and ultrahigh specific surface area, facilitating the adsorption of reactant molecules and thus improving their contact with active sites (Gao et al., 2021).

MOFs are a new generation of photoelectrocatalysts, their structural properties are advantageous for the study of PEC reaction mechanisms, such as adsorption, separation of charge carriers, mass transfer, active site access, etc. MOFs present various advantages when compared to other photoelectrocatalysts. Firstly, they have the properties of both a homogenous and a heterogeneous catalyst, being an ideal platform to study catalytic mechanisms because of their highly ordered crystal structure at the molecular level and their porous solid state provides them with a high catalytic activity, chemical stability, and easy recyclability. Moreover, the porous structure and large surface are increase the active sites and accelerate mass transport, improving the PEC activity (Gao et al., 2021).

Functional sites can be integrated to the MOF structure, obtaining a multifunctional material for catalysis. The morphology of the MOF can improve the PEC activity of the material, exposing more active sites or improving the charge transfer (Gao

et al., 2021). In their structure, the organic ligand acts as the valence band, and the metallic ions as the conduction band; thus, the photocatalytic activity of the material can be easily modified (Candia-Onfray et al., 2023).

Integrating a nanomaterial with the MOF can increase its intrinsic activity, enhancing its conductivity and the charge transfer process, a synergistic interfacial effect between both materials can improve the catalytic activity of the MOF. MOFs also enhance the ability of the material to cope in complex environments (acidic, alkaline and neutral) and it has a good recyclability, improving economic aspects. Furthermore, the ligand and metal active centers of the MOF are conductive, extending the light absorption region (Gao et al., 2021).

MOFs can also display good performance in PEC applications, certain MOFs present the properties of semiconductors, acting as a photocatalysts and being useful for organic transformations, water splitting for hydrogen pollution, CO_2 reduction, and the degradation of organic pollutants (Song et al., 2019). A series of representative MOF materials have been developed for solar-to-energy conversion in the field of photocatalysis, having great efficiency as catalysts in electrochemical reductions (Xue et al., 2018).

One of the advantages of MOF-based photocatalysts is the capacity to regulate the photocatalytic activity at a molecular level by modifying their metal nodes and organic ligands. In addition, the diffusion of reaction substrates and the promotion of the photocatalytic reaction rate are improved by tunning the pore size of the MOFs (Song et al., 2019). MOFs have the potential to improve the photocatalytic activity of other materials due to their ability to enhance the harvesting of irradiation energy and promote

charge transportation (Song et al., 2020). MOF-derived photocatalysts integrate high light adsorption capacity, catalytic sites, and high surface area all-in-one (Dong et al., 2021).

The use of bare MOFs in PEC reactions is restricted due to its rapid recombination of photogenerated e^-/h^+ and the fast oxidation by charge transfer (You et al., 2020). To overcome this drawback, MOFs can be modified by ligand substitution, functionalization with noble metals, and the construction of heterostructures, by coupling the MOF with a semiconductor substrate. Definite MOF-based heterostructures have displayed an improved photocatalytic efficiency (Song et al., 2019).

The growth of MOFs onto a conductive substrate, such as TiO_2 NT arrays, is useful for the development of electronic and opto-electronic devices, such as batteries, photovoltaics, and electrocatalysts. Molecular sieving MOF membranes have the facility to chemical separate molecules and MOF films can serve as an efficient catalyst for photo-oxidation, being an exciting prospect for applications in heterogeneous catalysis reactions. The synthesis of MOF films by the solvothermal deposition method presents the advantages of being easy, inexpensive, and efficient, compared to other film-processing techniques. Furthermore, this deposition approach avoids decomposition and defragmentation of powder MOF catalysts due to physical treatment methods, e.g., stirring (H. Yang & Fei, 2017).

Theorical calculations have demonstrated that MOFs can be regarded as semiconductors with large band gaps. The HOMO band in a MOF is governed by the conjugation of organic ligands, this way the bandgap can be modified by the ligands. Under light irradiations, the organic ligands are photoexcited by harvesting the light and they activate the metal nodes through ligand-to-metal charge transfer (Gao et al., 2021).

MOF derivatives are an attractive material for PEC catalysts. Transforming traditional MOFs into metal-based nanomaterials result in a more stable structure, increased channels for electron/mass transport, a greater number of active sites, and higher electrolyte permeability. MOF derivates can possess different morphologies, such as nanoparticles, nanorods, nanosheets, nanotubes, etc. (Gao et al., 2021).

4.10.2. UiO-66(Zr) MOF

One of the main issues in the use of MOFs in practical applications is their low stability. The UiO-66(Zr) MOF stands out for its great thermal and chemical stability (Khudozhitkov et al., 2021), having a decomposition temperature above 500 ºC, remaining crystalline at high pressures, and being resistant to many chemicals (Hoang Tran et al., 2021). UiO-66 is one of the most stable porous carboxylate MOFs, with an exceptional surface area (1180 – 1240 m^2/g) (Ponomareva et al., 2022).

The microporous UiO-66 is a zirconium-based MOF [$Zr_6O_4(OH)_4(CO_2)_{12}$] with a robust three-dimensional porous structure consists of 12 coordinated hexanuclear zirconium clusters (Zr_6O_{32}) linked by the bridging ligand benzene-1,4-benzodicarboxylic acid (BDC), also called terephthalic acid, and an isoreticular series (Yang et al., 2018). Each octahedral $Zr_6(\mu_3\text{-}O)_4(\mu_3\text{-}OH)_4$ cluster (where μ_3 is the element coupled to three metal atoms) is connected to 12 adjacent BDC ligands by carboxylate groups, forming a face-centered cubic (FCC) highly-packed framework (**Fig. 4.1.**) (Tan et al., 2019).

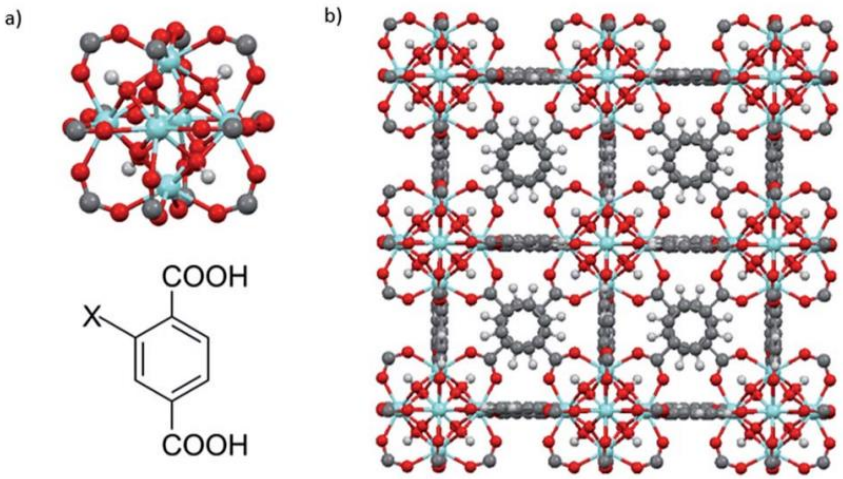

Fig. 4.1. UiO-66-X crystal structure (Zr: blue, O: red, C: gray, H: white). a) Octahedral Zr clusters (top) and BDC organic ligand (bottom) (X = H, NH_2, SO_3). b) Cubic unit cell. (Reproduced from Gong et al. (2018) with permission from the Royal Society of Chemistry).

Due to the highly oxophilic nature of Zr^{VI}, the Zr_6 cluster secondary building unit in the UiO-66 MOF is an inert and robust structure under different chemical conditions (Sun et al., 2013). Furthermore, the topological connections and strong coordination bonds provide the material with exceptional water stability, even in acidic or weak alkaline conditions (Qilin et al., 2020). The strong Zr-O coordination bonds between the clusters and the carboxylate ligands give the compact crystal structure a greater stability. In addition, its mechanical stability is attributed to the great number of connections in the framework from the high coordination between metal centers and organic ligand. The ability of inner Zr_6 clusters to rearrange reversibly after dihydroxylation or rehydration of μ_3-OH groups without affecting the connecting carboxylate ligands also contributes to the high stability of the material (Ponomareva et al., 2022).

The 3D porous structure of the material is formed by tetrahedral (~0.8 nm) and octahedral (~ 1.1 nm) cages interconnected by narrow triangular windows (~0.6 nm) (Hoang Tran et al., 2021). This pore-window-pore topology makes UiO-66 (Zr) a great platform for adsorption processes, having been applied in several separation and catalytic applications. The activity of the MOF is closely related to the mobility of the adsorbates, guest and structural dynamics of the framework as a result of adsorption should be study; yet, the molecular mechanism behind the adsorption process of MOFs is rarely reported (Khudozhitkov et al., 2021).

UiO-66 (Zr) remains structurally stable in many chemical solvents such as water, benzene, dimethylformamide, and strong acids, even at high pressures (Hoang Tran et al., 2021), and it does not undergo hydrolysis in pH from 0 to 10 (Ponomareva et al., 2022). This zirconium framework counts with an arrangement of secondary building units topologically equivalent to a cubic close-packed crystal structure. High-performance crystalline UiO-66 with different crystalline sizes shows excellent electrochemical properties. Owing to its high surface area and great thermal and chemical stability, the UiO-66(Zr) MOF has been widely used as an electrode material (Yang et al., 2018).

The functionalization of the UiO-66 framework is done to tune the properties of the material, which can be achieved by introducing functional groups through the organic ligand. For example, the substitution of BDC with the 2-aminoterephthalic acid (BDC-NH_2) generates an isostructural UiO-66(Zr)-NH_2 (**Fig. 4.2.**). This aminated Zr-MOF has shown an enhanced photocatalytic activity in the transformation of organic compounds under visible light irradiation, given that the amino groups can act as light-absorption chromophores enhancing the photocatalytic performance of the MOF (Sun et al., 2013). The presence of amino groups increase the adsorption capacity and the selectivity of the

MOF, but even though after functionalization the UiO-66 displays the same skeletal structure, the stability of the MOF usually presents some degradation (Cao et al., 2018).

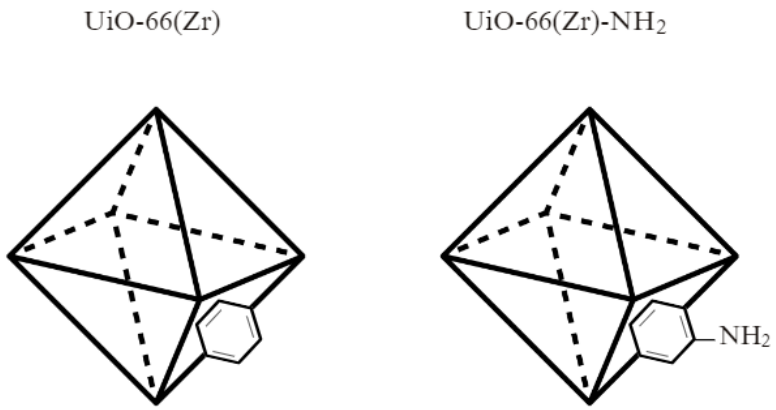

Fig. 4.2. Functionalization of UiO-66(Zr) with BDC-NH_2.

UiO-66 (Zr) is an alternative to the use of conventional zeolites as adsorbents, owing up to its good selectivity, high working capacity, and regeneration under mild conditions (Khudozhitkov et al., 2021). This MOF has been applied for gas separation, CO_2 capture, photocatalysis, and electrochemistry (Hoang Tran et al., 2021).

4.10.3. MIL-101(Fe) MOF

MOFs based MILs (Matériaux de l'Institut Lavoisier) series present great advantages attributed to their high stability and the availability of raw materials, working with Al^{3+}, Cr^{3+}, and Fe^{3+} ions (Gecgel et al., 2019). Férey et al. (2005) made one of the major discoveries in MOF chemistry by synthesizing the MIL-101 frame-work, a rigid zeotype cubic crystal structure of hydrothermally synthesized chromium(III) terephthalate, consisting of quasi-spherical cages of two modes (2.9 and 3.4 nm) (Maksimchuk et al., 2012). The MIL-101(Cr) presented a high surface area and pore volume, permanent porosity, and a great chemical and thermal robustness. These characteristics drew

attention to the MIL-101 MOFs for applications in sensing, separation, magnetism, gas and liquid storage, oxidative catalysis, and electrocatalysis (Barbosa et al., 2017).

The MIL-101 family consists of mesoporous MOFs whose structure is based on a series of "corner-sharing" super-tetrahedra, constituted by the linkage of inorganic trimers and BDC anions or its derivates (**Fig. 4.3.**). The super-tetrahedra connections guarantee the three-dimensional network morphology with and augmented mesoporous zeotype architecture, related to Mobil thirty-nine topology. MIL-101 MOFs are usually use as support/host due to their stability in water and its wide pore opening (Almáši et al., 2018).

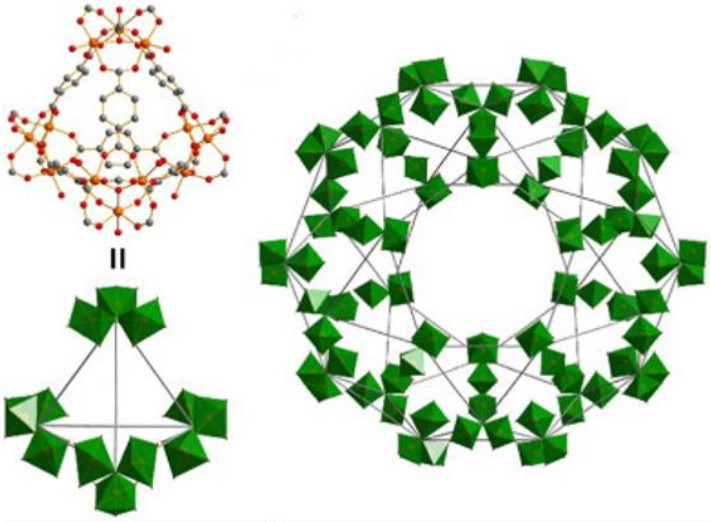

Fig. 4.3. Crystal structure of the MIL-101 family (Reproduced from Almáši et al. (2018) with permission from Elsevier).

Iron-based MILs have been extensively applied in different areas on account of its textural properties, including an extensive distribution of single iron sites, stability on aqueous mediums, porous structure, and large surface area (Gecgel et al., 2019). One of the most studied iron-based MOFs is the MIL-101 (Fe), having a well-defined morphology, good thermal stability, high porosity, and extra-large surface area (up to

4500 $m^2 \cdot g^{-1}$). MIL-101 (Fe) is a mesoporous carrier with pore sizes of 12 Å × 29 Å; 16 Å × 34 Å, and it is comprised of nontoxic components, employing BDC as the organic ligand and iron as the inorganic node (Alavijeh & Akhbari, 2020). The MIL-101(Fe) MOF consists of Fe^{3+} carboxylate trimetric clusters with terminal H_2O molecules. This molecules can be removed by a thermal vacuum treatment, yielding catalytically active sites coordinatively unsaturated (Maksimchuk et al., 2012).

MIL-101 (Fe) has been employed in different applications, such as imaging and drug delivery, proton exchange membranes, gas adsorption, and catalysis (Barbosa et al., 2017). (Maksimchuk et al., 2012) reported the intrinsic catalytic properties of MIL-101 (Fe), showing a superior activity and selectivity in the oxidation of cyclohexane. This study demonstrated that the nature of the active metal ions affects the product distribution of a reaction, being a useful heterogeneous catalyst applied in photocatalytic reduction, oxidation processes, synthesis, condensation, and coupling reactions (Barbosa et al., 2017).

The porous Fe(III) terephthalate MOF, MIL-101(Fe), has been used for diverse applications, for instance as gas adsorption, proton exchange membranes, imaging and drug delivery, solid supports for the immobilization of molecular species, and catalysis. As heterogeneous catalysts, MIL-101(Fe) has been employed in reactions such as photocatalytic CO_2 reduction, allylic oxidation of alkenes, coupling reactions, cyclic carbonate synthesis, and Knoevenagel condensation. It has been shown that the nature of the active metal ions in MIL-101 influence the product distribution of the reaction. An advantage of working with iron-based MOFs is that iron is a relatively abundant metal in the earth's crust and they are considered to be environmentally friendly (Barbosa et al., 2017).

4.11. TiO_2 NTs/MOF heterojunctions

MOFs are one of the most used modifiers of TiO_2 nanostructures for applications in photocatalyst, given that MOF/TiO_2 heterojunctions are able to promote the separation of photo-generated e^-/h^+ pairs during the photocatalytic process. TiO_2/MOF heterostructures can be applied as powerful catalysts in the photo-oxidation of organic contaminants, these composites can inhibit charge recombination being a potential material for efficient solar energy conversion, producing dye-sensitized solar cells (Xue et al., 2018). The specific interest of modifying the TiO2 NTs arrays with the Zr-MOF UiO-66 arrises from the more negative redox potential of Zr^{VI}/ Zr^{III} compared to Ti^{VI}/ Ti^{III} (Sun et al., 2013).

The properties of TiO_2 are surface dependent, hence coupling TiO_2 nanomaterials with MOFs of customized functionalities and porosity can benefit the development of novel electrodes (Xue et al., 2018). A cooperative synergism between TiO_2 and MOFs has the potential to enhance the PEC performance of the photoanode (Jia et al., 2020). The development of TiO_2 NT arrays as substrates for the deposition of thin films of catalytic MOFs can lead to novel catalytic applications in PEC, by doping TiO_2 NT arrays with MOFs the production of photocurrent can be promoted, increasing both conductivity and electron transfer (Cardoso et al., 2018). The presence of additional electrons and pores on the modified surface of the TiO_2 NT array, coming from the MOF, enables the effective carrying of charge carriers, enhancing reactions of reduction and oxidation (Aribam et al., 2022).

5. Methodology

5.1. Reagents and equipement

Titanium plates, glycerol ($C_3H_8O_3$), sodium fluoride (NaF), sodium sulfate (Na_2SO_4), potassium hydroxide (KOH), zirconium(IV) chloride ($ZrCl_4$), iron(III) chloride

hexahydrate ($FeCl_3 \cdot 6H_2O$), terephthalic acid (C_6H4-1,4-$(CO_2H)_2$) (BDC), 2-aminoterephthalic acid ($H_2NC_6H_3$-1,4-$(CO_2H)_2$) (BDC-NH_2), and acetic acid (CH_3COOH) were purchased from Sigma-Aldrich. Acetone and ethanol were purchased from J. T. Baker, sulfuric acid (H_2SO_4) from Merck Millipore, and dimethylformamide (C_3H_7NO) from Reactivos Meyer. Methyl red indicator was purchased from Mallinkrodt Pharmaceuticals. Distilled water was obtained from the Merck Millipore Elix Essential 3 water purification system.

Electrochemical anodization was carried out using a B&K Precision 1761 DC power supply. Calcination processes were done in the Cole-Parmer Thermo Scientific Thermolyne tube furnace. A Parr 4749 acid digestion vessel was used for solvothermal synthesis. Scanning electron microscope (SEM) and Energy-dispersive X-ray (EDX) spectroscopy measurements were execute by a Tescan MAIA3 Triglav coupled with a Bruker XFlash 6|30 EDX detector. Raman analysis was carried out by a Horiba XploRA PLUS confocal Raman microscope with a laser gun of 532 nm. Fourier Transform Infrared (FTIR) spectra was obtained from the Agilent Technologies Cary 630 FTIR spectrometer coupled with an Attenuated Total Reflectance (ATR) accessory. Cyclic voltammetry (CV) characterization was done using a Digi-Ivy DY2100 Mini potentiostat.

Photoelectrocatalytic (PEC) and photocatalytic (PC) degradation experiments were conducted using an UVP Blak-Ray B-100AP UV lamp with a 100-watt longwave (365 nm) bulb and a Tacussel PJT 24-1 Potentiostat/Galvanostat. PEC and PC systems were cooled down by a Cole-Parmer Polystat refrigerated circulating bath. The degradation process of methyl red was followed using an Agilent Varian Cary 50 UV-Vis spectrophotometer.

5.2. Synthesis

5.2.1. Synthesis of TiO_2 NTs electrodes

In this work, TiO_2 NT arrays were synthesized employing a third-generation organic electrolyte with fluoride salts. The main advantages of constructing arrays of third generation TiO_2 NTs are the increase on tube length, due to the neutral pH that avoids the dissolution on the top of the NTs, and a smooth external structure, on account of the use of viscous glycerol that prevents local concentration fluctuations and pH bursts during the anodization process. In the third generation of TiO_2 NTs, the main aspects that control the synthesis are potential, water content, and anodization time (Aliofkhazraei & Makhlouf, 2016).

TiO_2 NT arrays were synthesized onto titanium plates by electrochemical anodization using a two-electrode system. The working electrode was a titanium plate with a purity of 99.7%, a square area of 1.0 cm^2 (plus stem) and a thickness of 0.127 nm (**Fig. 5.1.**). The counter electrode was also a titanium plate with a greater area of 9.0 cm^2. The working electrode was cleansed by an ultrasonic bath using acetone, ethanol, and distilled water. The two-electrode system was immersed in an anodizing solution, which contained a mixture of distilled water and glycerol (1.3:1 v/v) with NaF (0.5 % w/v) and Na_2SO_4 (0.2 M). A voltage of 30.0 V was applied until the anodization process was complete. An iridescent surface was formed in both sides of the titanium plate, suggesting the correct formation of the nanotubes. The resulting electrode with TiO_2 NTs arrays was then cleansed by sonication with acetone. The electrode then was subjected to an annealing process by calcination in a tube furnace at 500 ºC for 1h30, with a heating ramp of 5 ºC/min, to remove impurities and to induce the transformation of amorphous TiO_2 to

the anatase phase to improve its catalytic activity and other properties, such as thermal stability and electrical conductivity.

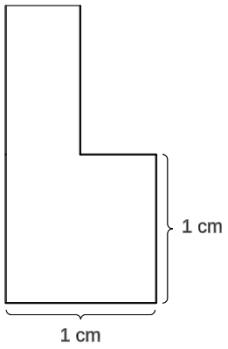

Fig. 5.1. Dimensions of the as-synthesized TiO_2 NTs electrode.

5.2.2. Modification of TiO_2 NTs electrodes with Zr and Fe MOFs

For the modification of the TiO_2 NTs arrays with MOFs of the transition metals zirconium and iron, the solvothermal method was employed using an autoclave pump. The UiO-66(Zr) MOF was synthesized using the salt $ZrCl_4$, dimethylformamide (DMF) as solvent, acetic acid as modulator, and terephthalic acid (BDC) as the organic ligand. After the homogenization of the reactants by ultrasonic bath, the TiO_2 NTs electrode was placed at the bottom of the autoclave pump and treated in the oven for 24 h at 120 ºC for its modification. Once the thermal reaction took place, a white precipitate formed in the surface of the electrode (**Fig. 5.2.a**). Aminated UiO-66(Zr) was also synthesized for the modification of the TiO_2 NTs, employing the organic ligand BDC-NH_2. The resulting MOF had a pale-yellow tonality.

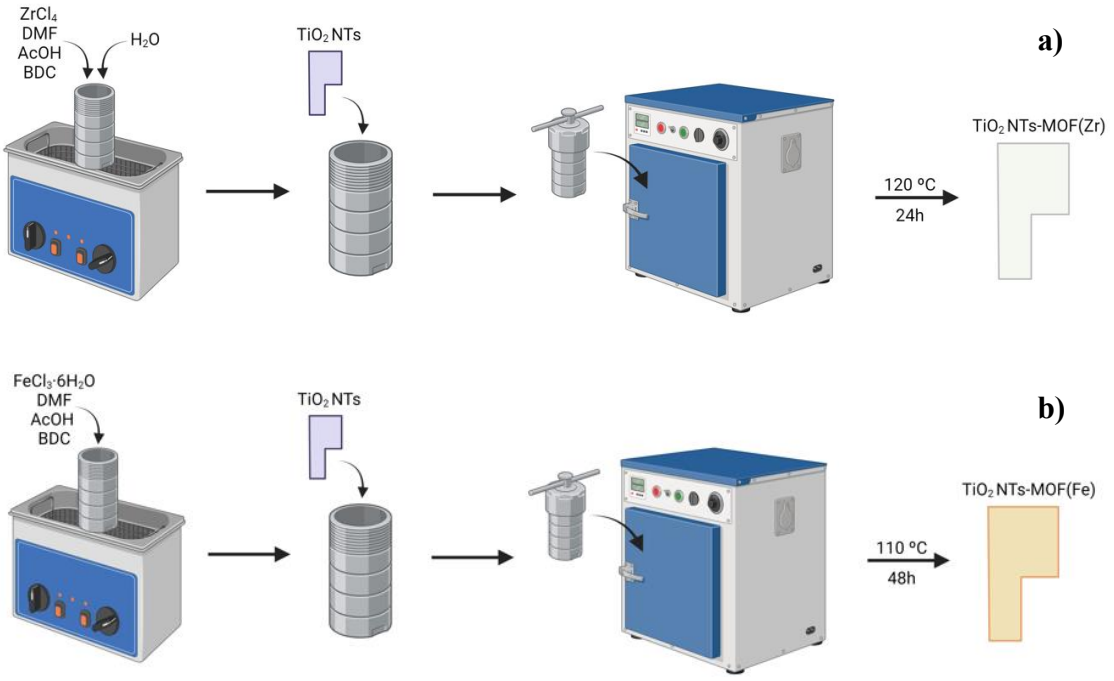

Fig. 5.2. Modification of TiO_2 NTs electrodes with a) Zr MOFs and b) Fe MOFs.

The same procedure was followed for the MIL-101(Fe) MOF, using the salt $FeCl_3 \cdot 6H_2O$, acetic acid as modulator, and the same solvent and organic ligand. In this case, after a thermal treatment of 48h at 110ºC, an orange precipitate was formed (**Fig. 5.2.b**). The resulting modified electrodes were cleansed with distilled water under an ultrasonic bath in order to remove the MOF crystals that were not strongly attached to the surface of the electrode,

5.2.3. Purification of MOFs

After removing the MOF-modified electrode, the remaining precipitates of the UiO-66(Zr) MOF and MIL-101(Fe) MOF were recovered and purified for their later characterization. The MOFs were washed with DMF and ethanol several times before leaving it suspended in ethanol for 48h for a solvent change, a couple more ethanol washes were performed before drying the products in the oven for 24h, at a temperature

of 60 ºC for the Zr-MOF and 75 ºC for the Fe-MOF. The resulting products were white and orange powders for the UiO-66(Zr) and the MIL-101(Fe) crystal MOFs, respectively.

5.3. Characterization

5.3.1. Scanning Electron Microscopy (SEM)

Scanning electron microscope (SEM) was used to obtain micrographs to analyze the surface morphology and topography of the synthesized electrodes. These images helped confirm the correct synthesis of the TiO_2 NTs, the average diameter of the nanotubes, the growth of the MOF crystals onto their surface, and the size of these crystals. SEM characterization was performed three times throughout the electrodes' synthesis. First, after the electrochemical anodization process to analyze the right formation and morphology of the NTs array; then, after solvothermal treatment to confirm the growth of the MOF onto the electrode; and finally, after the cleansing of the modified electrode, accompanied by an EDX analysis to verify the growth of the MOF inside and around the NTs.

Before MOF-modification, SEM images of TiO_2 NTs bare electrodes (**Fig. 5.3.**) were obtained to confirm the correct formation of the NT array. From these micrographs, it was determined that the diameter of the NTs formed was under 250 nm.

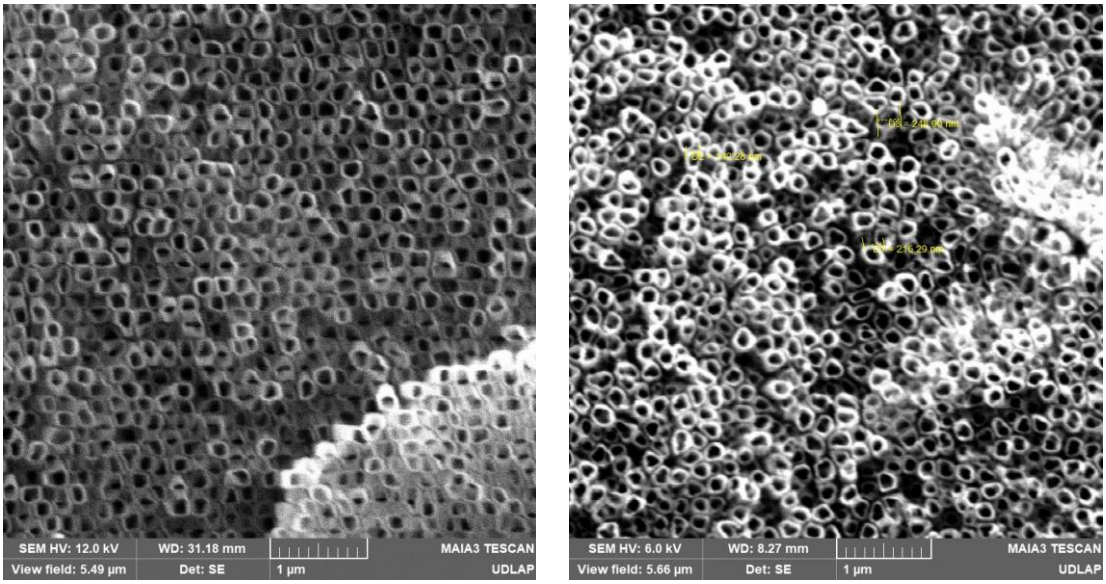

Fig. 5.3. SEM micrographs of TiO_2 NTs bare electrodes.

Another set of SEM micrographs were captured after the solvothermal MOF-modification of the electrodes, before ultrasonic cleansing (**Fig. 5.4.**). We can clearly observe the growth of MOF crystals onto the surface of the NT array, the size of these crystals was from 145 to 600 nm.

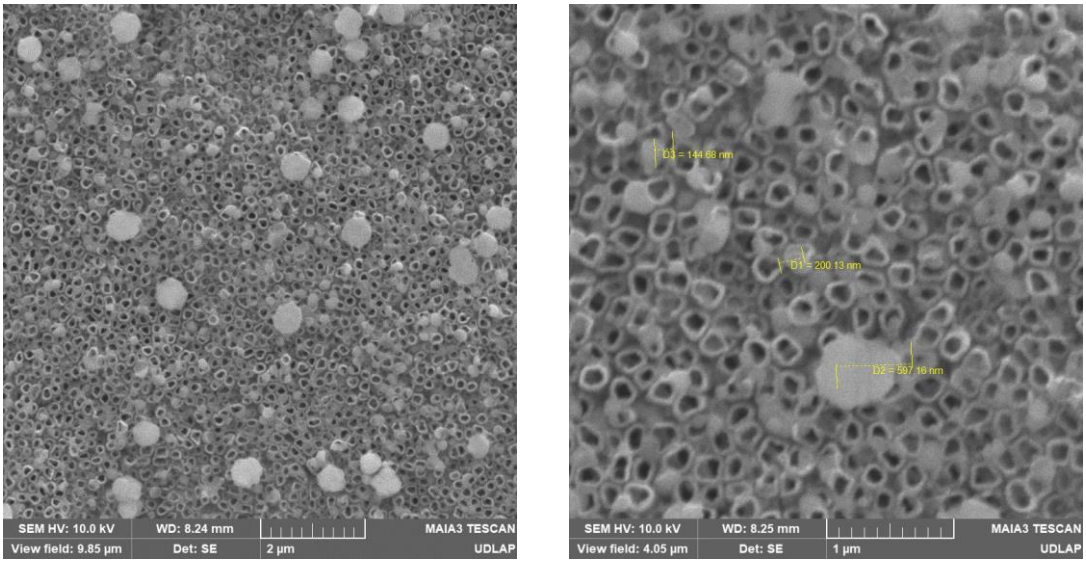

Fig. 5.4. SEM micrographs of (Fe)MOF crystals grown onto TiO_2 NTs arrays before ultrasonic cleansing.

Fig. 5.5. presents a SEM micrograph of the final MOF-TiO_2 NTs electrode synthesized. A fairly homogenous surface was achieved, with some differences that arise mainly from the length of the NTs and some residual MOF adsorbed in the surface of the electrode.

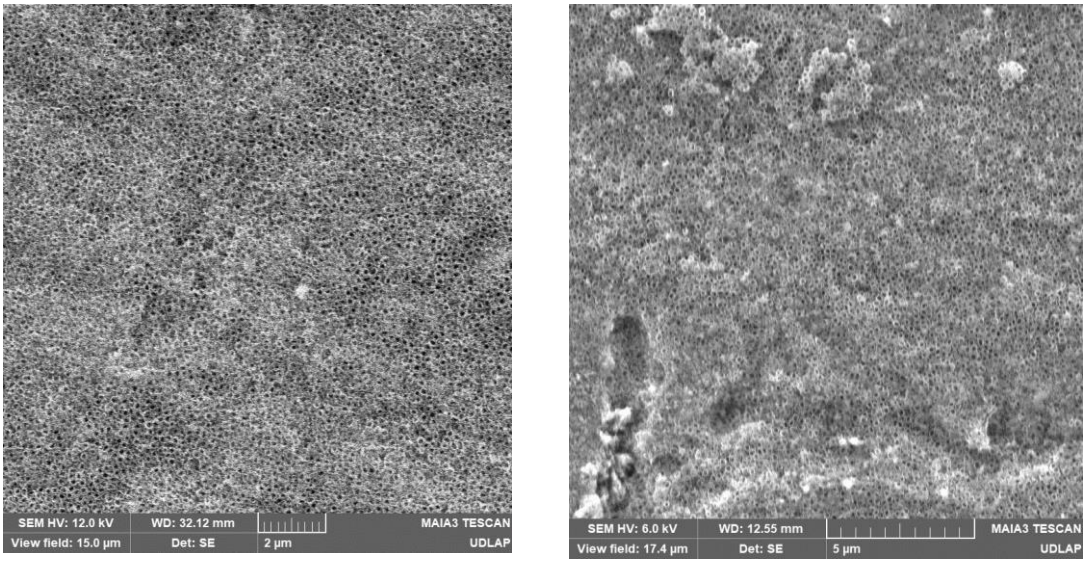

Fig. 5.5. SEM micrograph of (Zr)MOF-modified TiO_2 NTs electrode.

5.3.2. Energy-Dispersive X-ray (EDX) Spectroscopy

To evaluate the growth of the MOF inside and in between the TiO_2 NTs, EDX analysis was implemented for both (Fe)MOF and (Zr)MOF modified electrodes to obtain qualitative and quantitative information about their elemental composition. **Fig. 5.6.** shows the elemental spectrum and quantification of (Fe)MOF TiO_2 NTs electrode. The high atomic percentage of iron in the analysis (20.66 %) indicates a considerable amount of (Fe)MOF present in the electrode.

Following SEM images, we can determine that the MOF correctly grew inside the vacancies of the NTs arrays. The same conclusions can be drawn from the EDX analysis of the (Zr)MOF TiO_2 NTs electrode, presented in **Fig. 5.7.**, where zirconium has a slightly

lower, but still significant, contribution to the atomic percentage of the sample (9.93%). In comparison, the atomic percentage of titanium was even lower (4.76%), indicating that the NT array was well covered with the (Zr)MOF that grew correctly on top of it. It is important to mention that the transition metal contribution to the mass of the electrodes varied in each synthesis, suggesting that the growth of the MOF onto the NT array was not always constant in the solvothermal treatment.

EDX analysis corroborates that the MOF crystals not only grew onto the surface of the electrode but are also present inside and around the NTs arrays. This will allow the MOFs of transition metals to enhance the PEC activity of the TiO_2 NTs, without blocking the NTs arrays properties. In addition, it was confirmed that the electrodes did not present contamination, only small percentages of carbon and fluor were identified but these elements come from remains the of the anodization solution used in the synthesis of the TiO_2 NT array, which were calcinated during the thermal treatment.

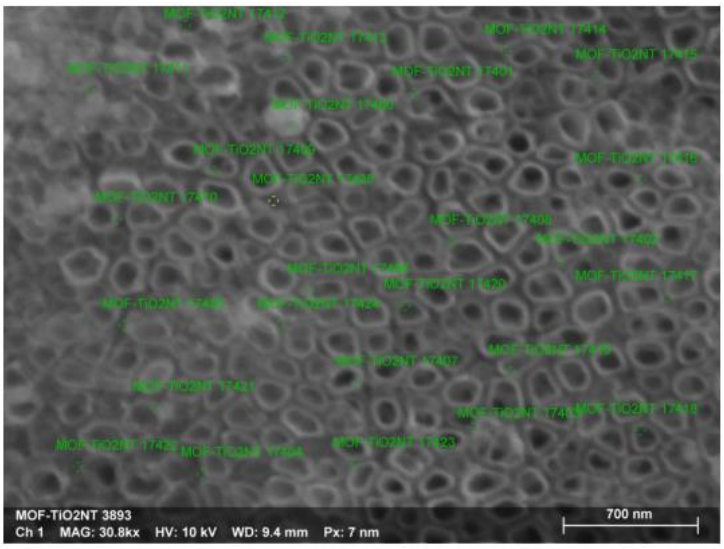

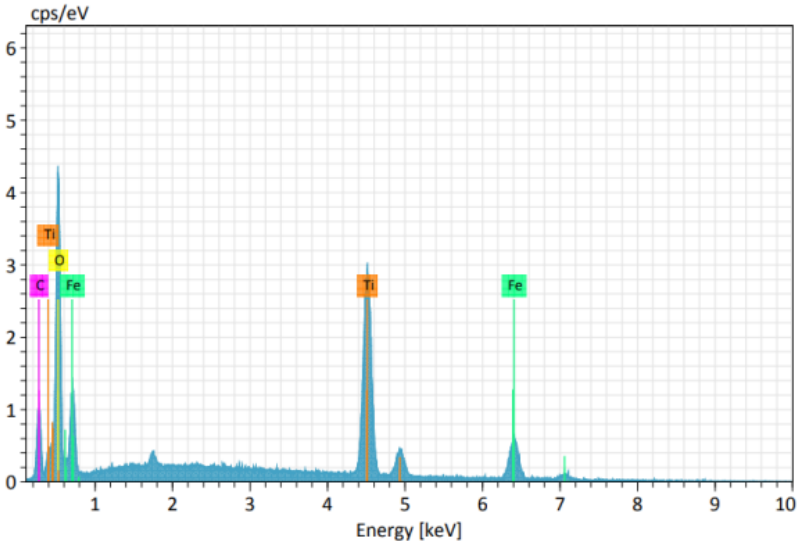

Element	At. No.	Netto	Mass [%]	Mass Norm. [%]	Atom [%]	abs. error [%] (1 sigma)	rel. error [%] (1 sigma)
Titanium	22	35075	37.98	38.77	26.04	1.35	3.55
Iron	26	7977	35.15	35.89	20.66	1.65	4.70
Oxygen	8	23972	21.36	21.81	43.84	2.71	12.70
Carbon	6	4516	3.46	3.53	9.45	0.58	16.68
		Sum	**97.95**	**100.00**	**100.00**		

Fig. 5.6. EDX analysis of (Fe)MOF-modified TiO_2 NTs electrode.

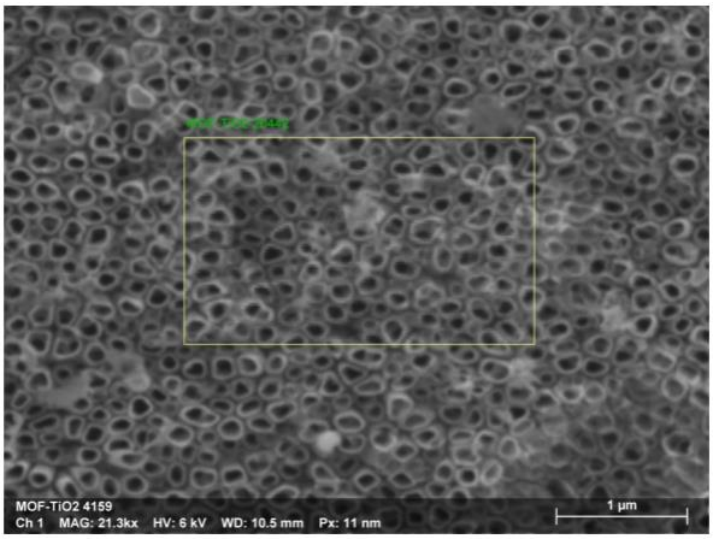

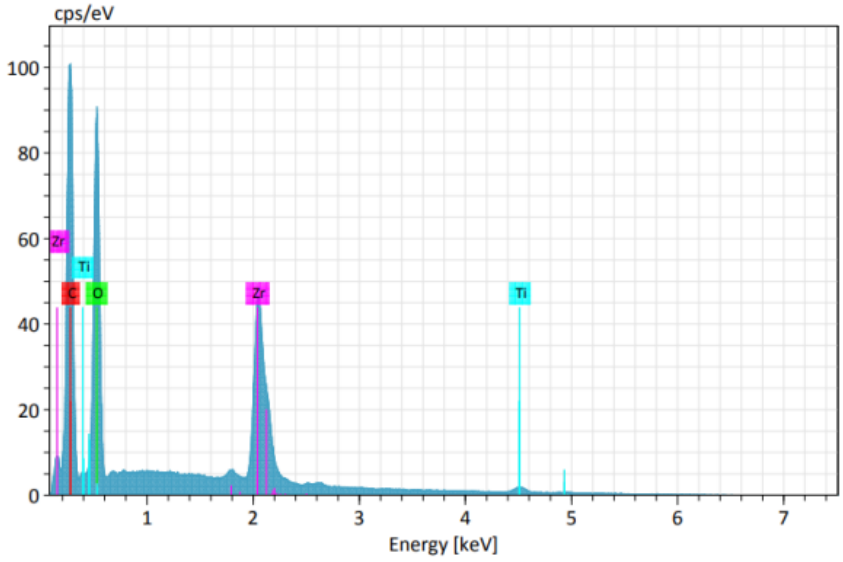

Element	At. No.	Netto	Mass [%]	Mass Norm. [%]	Atom [%]	abs. error [%] (1 sigma)	rel. error [%] (1 sigma)
Carbon	6	98871	23.25	27.32	52.10	2.65	11.38
Oxygen	8	87715	19.75	23.20	33.21	2.27	11.48
Titanium	22	7541	8.47	9.95	4.76	1.26	14.90
Zirconium	40	103061	33.66	39.54	9.93	1.39	4.14
		Sum	**85.13**	**100.00**	**100.00**		

Fig. 5.7. EDX analysis of (Zr)MOF-modified TiO_2 NTs electrode.

To further confirm the homogenous distribution of the MOF in the TiO_2 NTs arrays, an elemental mapping was carried out. **Fig. 5.8.** displays the distribution of

titanium and zirconium in the (Zr)MOF TiO_2 NTs electrode, showing a good relation between the TiO_2 NTs and the (Zr)MOF distribution on the modified electrode.

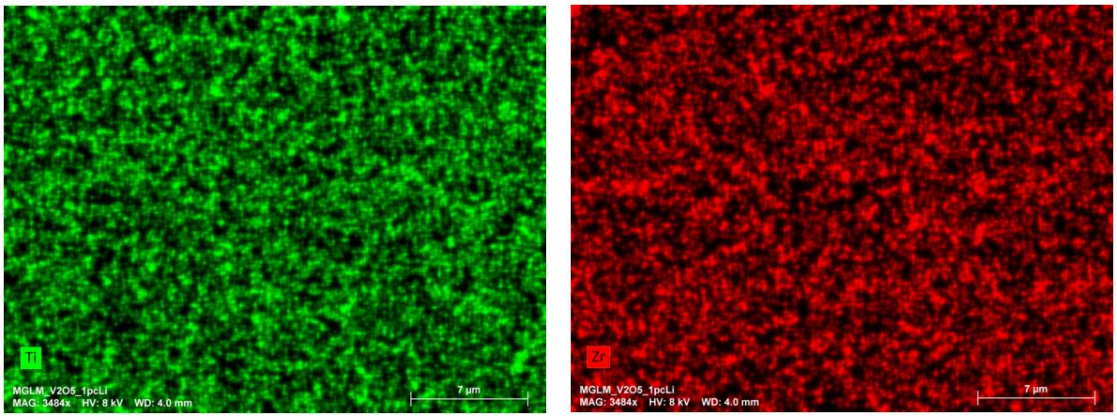

Fig. 5.8. EDX elemental mapping of (Zr)MOF-modified TiO_2 NTs electrode.

5.3.3. Raman Spectroscopy

Further structural analysis of the TiO_2 NTs, MOFs, and composite electrodes was carried out through Raman spectroscopy. The pristine MIL-101(Fe) and UiO-66(Zr) MOFs were characterized in powder form, after being purified and completely dried. Raman spectra were collected in a range of 60-3400 cm^{-1}.

Firstly, this characterization technique was used to confirm the transition of the crystallographic structure of the TiO_2 NTs from amorphous to the anatase phase during the annealing process. It has been reported that anatase TiO_2 presents six fundamental vibrational modes, in comparison with the amorphous phase which has very weak signals in Raman scattering (Barbosa et al., 2017; Frank et al., 2012; Mukherjee & Mergel, 2013). **Fig. 5.9.** presents the Raman spectrum of the pure TiO_2 NTs, the peaks obtained are assigned to the molecular vibrational modes A_{1g} (505.56 cm^{-1}), B_{1g} (394.78 cm^{-1} and 508.61 cm^{-1}), and E_g (146.53 cm^{-1}, 197.39 cm^{-1}, and 629.96 cm^{-1}). No additional bands

are present in the spectrum, which confirms the pure anatase phase that is favored over the rutile phase during the thermal treatment of the prepared NTs.

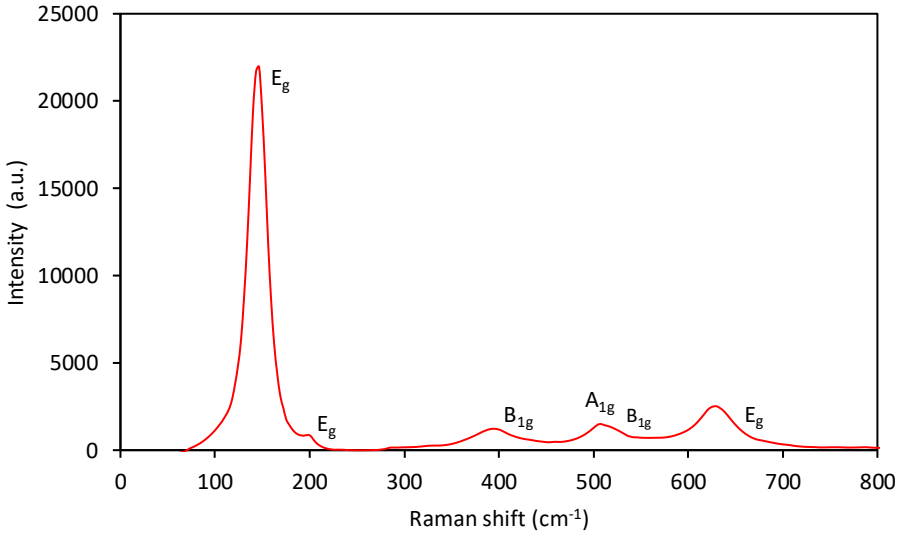

Fig. 5.9. Raman spectrum of TiO_2 NTs bare electrode.

In MOFs crystal, it is challenging to assign the Raman bands to specific vibrational modes due to the complexity of the arrangements, most of the vibrations are not pure motions of a specific species. Moreover, the large number of atoms in MOF systems produce a great quantity of Raman modes with frequencies that are very closely spaced; despite the modes having different motions, most of the atomic motions are just slightly different and occur in the same species in a small frequency region. An exact assignment of Raman bands is almost impossible in such a complex structure. Thus, Raman spectra of the MOFs will be discussed in terms of different family modes (Yost et al., 2022).

The vibration dynamics of the anatase phase of TiO_2 are presented in **Fig. 5.10**. The arrows indicate the displacement of the atoms, showing only one of the possible displacement geometries for double degenerated vibrations (E_g), and the length of the

arrows represent the amplitude of the vibration, the length is proportional to the involvement of the atom in motion (Frank et al., 2012).

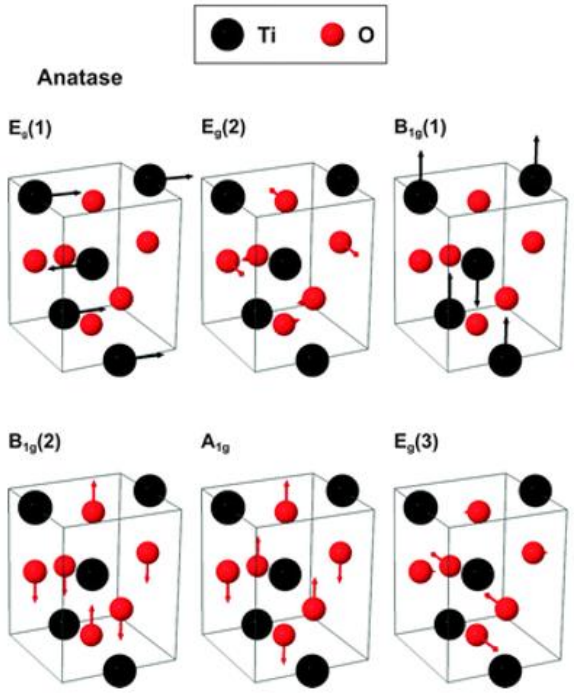

Fig. 5.10. Scheme of the molecular vibrations in symmetry allowed Raman-active modes of anatase phase of TiO_2. (Reproduced from Frank et al. (2012) with permission from the Royal Society of Chemistry).

The UiO-66(Zr) MOF Raman spectrum is presented in **Fig. 5.11.**, this spectrum is in agreement with characterizations reported in the literature (Yost et al., 2022; Andrade et al., 2022; Piscopo et al., 2015) and it is even consistent with the simulated model from the ideal UiO-66 structure reported by Shearer et al. (2014). In this Raman spectrum we can find that the three main family modes correspond to (1) modes dominated by the Zr-O coordination bond, (2) modes assigned mainly to contributions from motion of Zr-μ_3-OH and Zr-μ_3-O, and (3) modes of motions primarily confined to the ligands, with slight motion of the metal atoms or withing the subunits (Yost et al., 2022).

Raman modes with frequencies between 425-450 cm^{-1} are mostly attributed to the motions of the bond Zr-μ_3-OH, each mode having slightly different motions and providing different contributions from the ligand molecule. In this region, some motions appear to be pure Zr-μ_3-OH wagging, while other contributions are more complex, with a combination of motions from the ligand carboxylate tails and C-H wagging in the benzene ring. The Raman band at 865 cm^{-1} corresponds mainly to C-H motion from the ligands and in the "fingerprint region" (150-400 cm^{-1}) most Raman-active modes come from the Zr atoms (Yost et al., 2022). According to Andrade et al. (2022) band assignment of the UiO-66 Raman spectra, the band at 242 cm^{-1} could be attributed to either the out of plane ligand metal-cluster bending and the Zr-(OH)-Zr bending or the O-C-O translation mode. The band at 496 cm^{-1} can be ascribed to the in-phase bending of μ_3-OH and μ_3-O. We observe two combined bands at 1432 cm^{-1} and 1448 cm^{-1}, the former can be related to two vibrational modes, the in-plane asymmetric C=C-H bending and the asymmetric C=C stretching, and the later the C-C symmetric stretching.

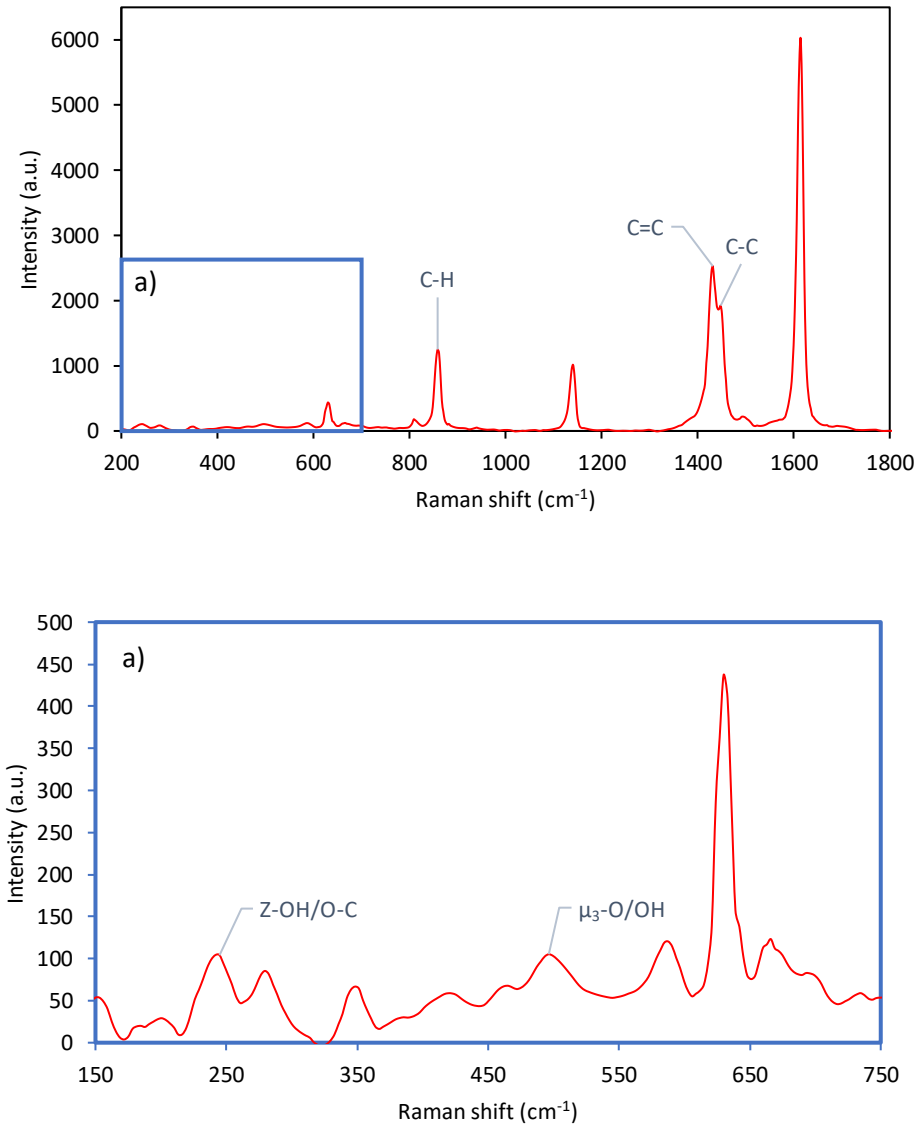

Fig. 5.11. Raman spectrum of UiO-66(Zr) MOF, a) close up of the fingerprint region.

The Raman spectrum of the MIL-101(Fe) MOF is presented in **Fig. 5.12.**, the signals present considerable noise, this may be due to remaining of the solvents used during the purification of the MOFs. In the MIL-101 spectrum, most of the bands correspond to the organic ligands in the framework (Liu et al., 2021). The vibrational bands observed in the range 860–1620 cm^{-1} indicate the aromatic and dicarboxylate groups in BDC (Beiranvand et al., 2022). Bands around 1140 cm^{-1} are ascribed to the

C=O of the carboxylic group, those around 1453 cm^{-1} to the C-C bond in the benzene ring, and the bands about 820 cm^{-1} are assigned to vibrations of the benzene ring and of C-H bonds (Liu et al., 2021). We can also observe a wide peak between 1500 – 2000 cm^{-1}; Zhou et al. (2014) and Duan et al. (2018) reported a Raman spectra of the MIL-101(Fe) with characteristic intense peaks around 1600 cm^{-1}, an overlapping of these signals could also have taken place because of the persistence of solvents in the characterized MOF sample.

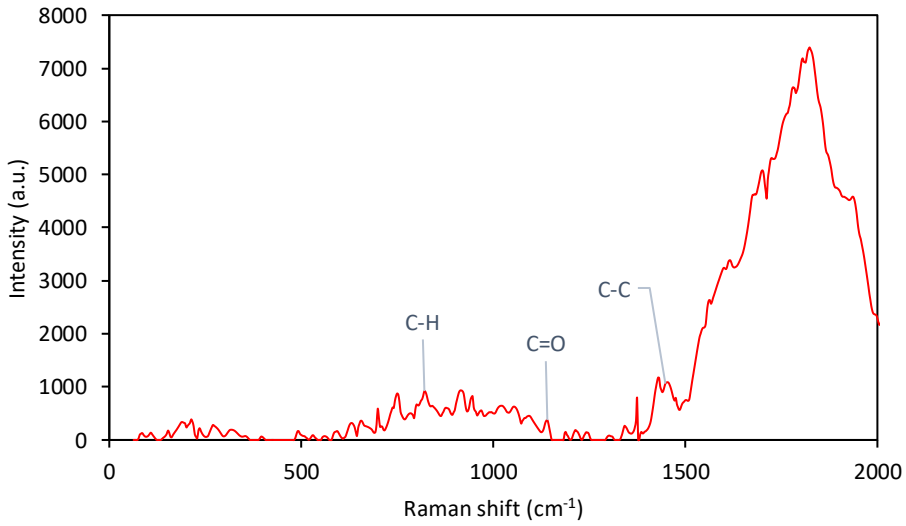

Fig. 5.12. Raman spectrum of MIL-101(Fe) MOF.

Raman spectra of the modified TiO_2 NTs electrodes with the MIL-101(Zr) MOF and the UiO-66(Fe) MOF are presented in **Fig. 5.13.** and **Fig. 5.14**, respectively. When compared to the bare TiO_2 NTs spectrum, it can be observed that only the characteristic band signals of the molecular vibrations of the anatase phase of TiO_2 are present, only exhibiting a weaker intensity going from a scale of over 20 000 a.u. to 6000-8000 a.u., this can be due to a lowering on the surface plasmon resonance effect caused by the MOF growth into the TiO_2-NT array. Being able to observe the bands of anatase TiO_2 indicates

that the MOF-modification of the electrodes does not interfere with the properties of the nanotubes.

Having no additional bands from the MOFs structure could be attributed to the fact that MOFs tend to have a weak Raman signal, because of their composition of light atoms that do not scatter the light as strongly (Sun et al., 2019), that is hard to detect against the background signal of the TiO_2 NTs. Additionally, EDX analysis showed a relatively low concentration of the MOFs on the surface of the electrode, thus the characteristic bands of the MOF are not easily detectable. It is also possible that the characteristic bands of the MOFs overlap with those of the TiO_2.

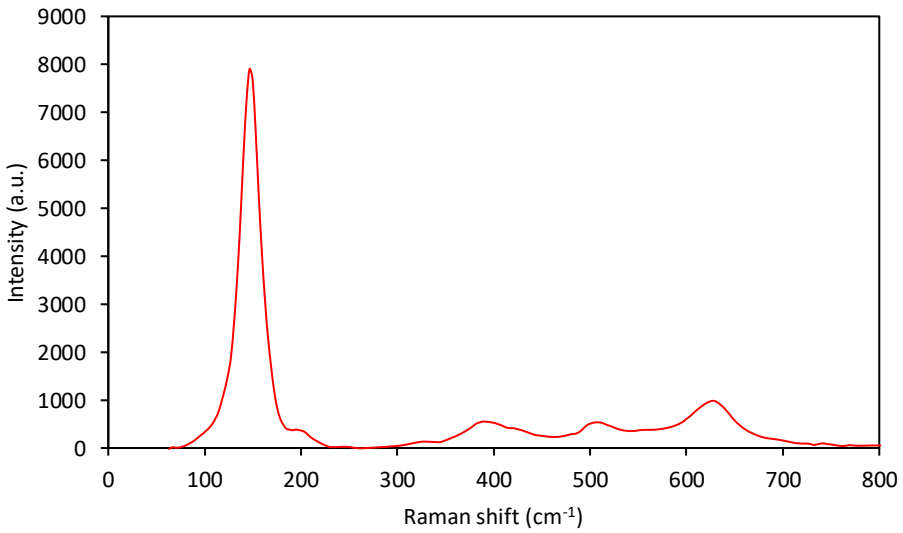

Fig. 5.13. Raman spectrum of (Zr)MOF-modified TiO_2 NTs electrode.

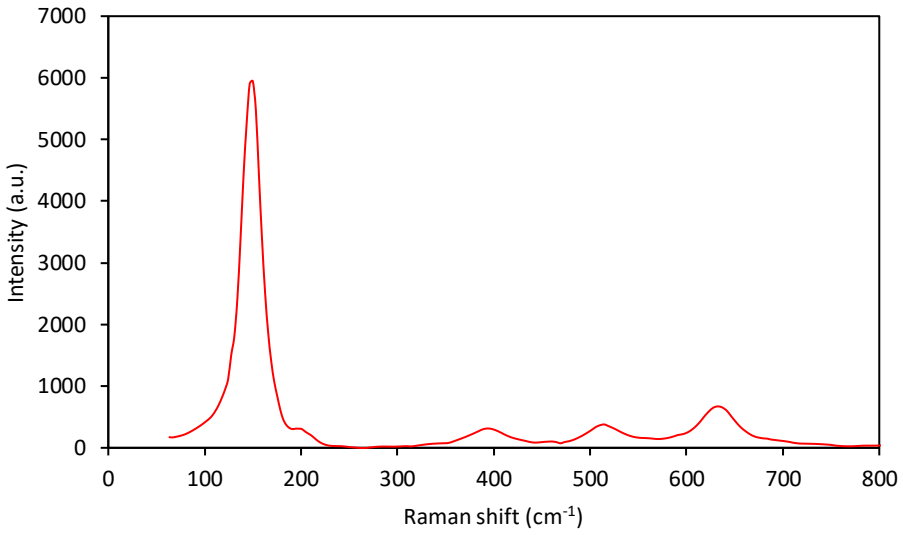

Fig. 5.14. Raman spectrum of (Fe)MOF-modified TiO_2 NTs electrode.

5.3.4. Fourier Transform Infrared (FTIR) Spectroscopy

To confirm the molecular structure and functional groups present in the TiO_2 NT arrays and MOF structure, Fourier Transform Infrared (FTIR) spectroscopy analysis was carried out to study the electrodes properties. FTIR measurements were taken at a range of 400–3900 cm^{-1}.

Fig. 5.15. presents the FTIR spectrum of the bare TiO_2 NTs, which is in concordance with previously reported data (Zakir et al., 2022; Ismail et al., 2018; Terracciano et al., 2017; Nie et al., 2013). The broad band between 900-400 cm^{-1} can be assigned to the different vibrational modes of the anatase phase of TiO_2, especially the band at 402 cm^{-1} corresponds to the stretching of the Ti-O bond. The band around 1715 cm^{-1} can be attributed to the stretching and bending vibrations of the O-H groups of the adsorbed water molecules at the TiO_2 surface (Zakir et al., 2022; Nie et al., 2013).

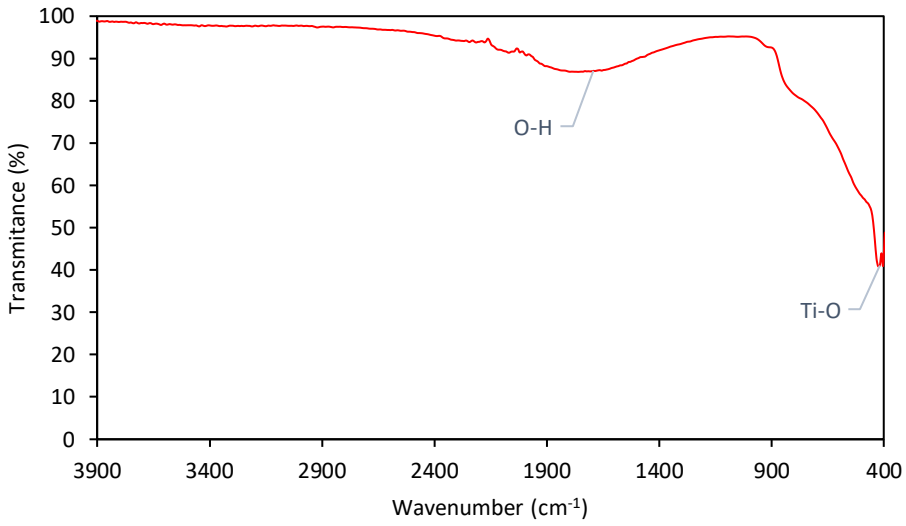

Fig. 5.15. FTIR spectrum of bare NTs TiO_2.

To ensure a complete and accurate characterization of complex systems, such as MOFs, it is important to analyze the material through both Raman and IR vibration spectroscopies. Compared to Raman characterization, IR spectroscopy allows for a more complete characterization of the vibrational modes in MOF structures due to the fact that many modes observed in the IR spectrum are not Raman-active or have very weak Raman signals (Yost et al., 2022). The FTIR spectroscopy spectra of the UiO-66(Zr) and MIL-101(Fe) MOFs are reported in **Fig. 5.16.** and **Fig. 5.17**., respectively. In both IR patterns, we can observe a broad absorption band around 3000 cm^{-1} that is assigned to the stretching vibration of O-H coming from the presence of residual solvent and adsorbed water in the samples, or it could be induced by the hydroxyl groups coming from the deprotonation of the carboxylate groups in the BDC organic ligand (Duan et al., 2018; Xu et al., 2019).

The characteristic FTIR peaks of the UiO-66(Zr) MOF (**Fig. 5.16.**) that appear at 1588, 1394, 1021, 746, 664, 552, and 477 cm^{-1} are mainly due to the Zr-BDC

combination, proving the structural crystal transformation. Peaks at 477 and 552 cm^{-1} are assigned to the in/out-of-plane ring deformation. The pair of peaks at 746 and 664 cm^{-1} correspond to the Zr-μ_3-O stretching and the symmetric vibration of O-Zr-O. The signal at 1394 cm^{-1} is assigned to the C-C ring modes. The peak at 1588 cm^{-1} is attributed to the O-C=O asymmetric in/anti-phase stretching vibrations. The peak at 1021 cm^{-1} confirms the coordination between the Zr metallic nodes and the organic ligand. (Vellingiri et al., 2017).

The obtained FTIR peaks indicate that the main functional groups in the BDC have been kept in the MOF structure, proving that the Zr metal coordination center in the organic framework is formed by bridging with the organic ligand BDC through the bond μ_3-O (Xu et al., 2019). The presented FTIR spectrum is in agreement with those reported previously (Zhang et al., 2022; Kim et al., 2021; Xu et al., 2019; Vellingiri et al., 2017).

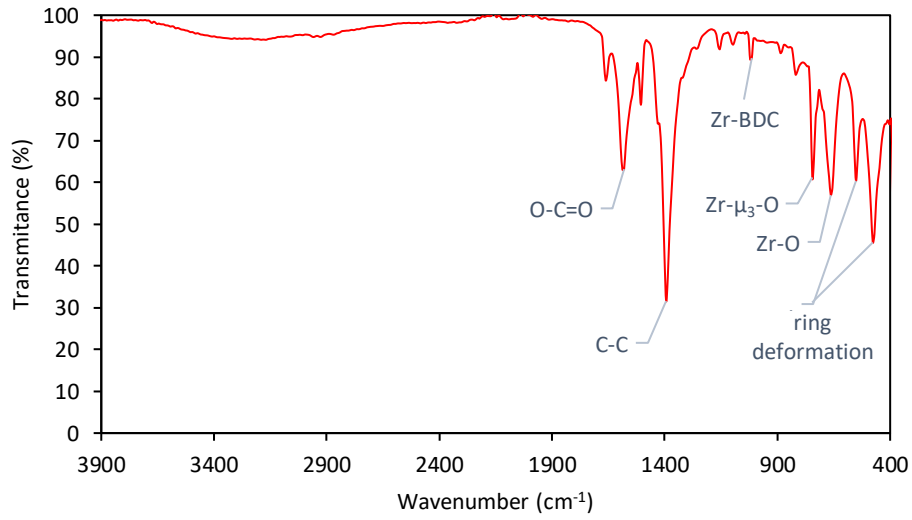

Fig. 5.16. FTIR spectrum of UiO-66(Zr) MOF.

The characteristic FTIR peaks of the MIL-101(Fe) MOF structure appear at 544, 746, 1021, 1379, 1506, and 1551 cm^{-1} (**Fig. 5.17.**). MIL MOFs consist of benzene-

carboxylates; therefore, the signals that appear in the IR spectrum are mainly originated from the vibrations of C=O and C-O on the carboxyl groups and C-H on the benzene ring of the BDC (Xie et al., 2017; Hu et al., 2019).

The peak at 544 cm^{-1} is assigned to the Fe-O bond vibration, at 746 cm^{-1} the signal comes from an out-of-plane bending vibration of C-H groups in benzene, and the C-O-C bending is assigned to the peak at 1021 cm^{-1}. The absorption bands assigned to the carboxyl groups are present at 1379 and 1506 cm^{-1}, corresponding to the symmetric and asymmetric vibrations of O-C=O, and at 1551 cm^{-1} from the C=O bond. The strong peak at 1506 cm^{-1} can also be related to the aromatic C-C vibrational mode. This is in agreement with the reported literature (Beiranvand et al., 2022; Liu et al., 2021; Duan et al., 2018), verifying the correct synthesis of the framework.

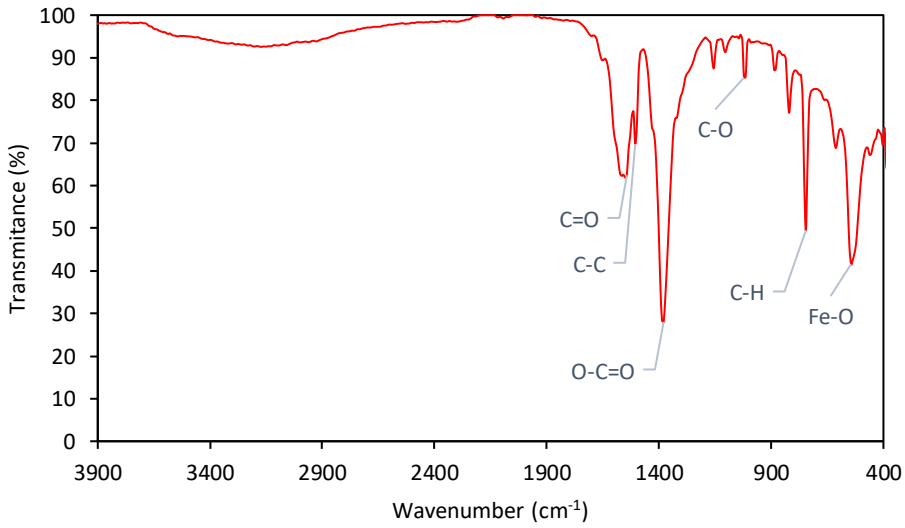

Fig. 5.17. FTIR spectrum of MIL-101(Fe) MOF.

The MOF-coupled TiO_2 NTs electrodes were also characterized by FTIR spectroscopy, the spectra of the Zr-MOF and the Fe-MOF electrodes is presented in **Fig. 5.18.** and **Fig. 5.19.**, respectively. Similar to the Raman characterization results, in the

spectra of the modified electrodes we observe just the signals coming from the TiO_2 NT arrays. The bands are the same as the FTIR spectrum of the bare TiO_2 NTs electrode (**Fig. 5.14**), with just a slight shift in the position and change in the intensity of the bands. This may be attributed to the interactions between the NTs and the MOF structure or to the presence of dopants in the interstitials of the lattices in the electrode's structure (Zakir et al., 2022).

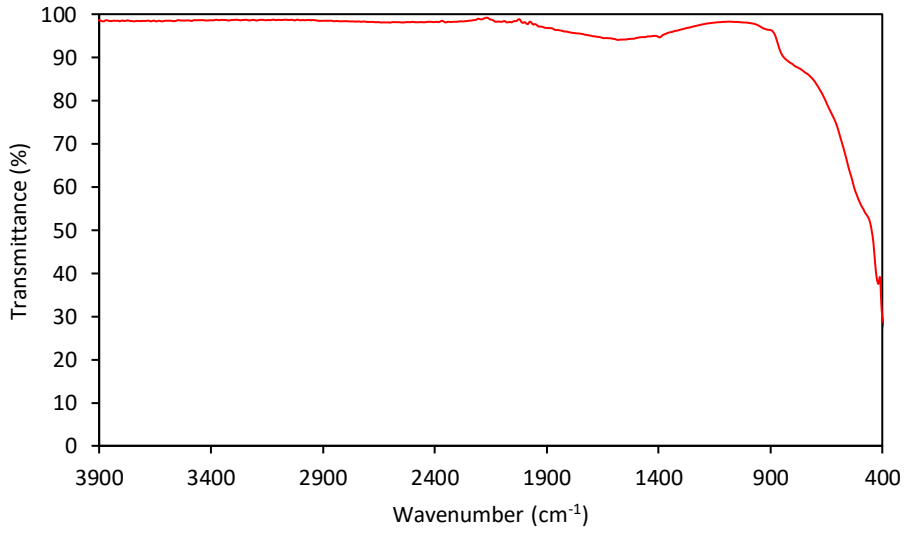

Fig. 5.18. FTIR spectrum of NTs TiO_2-MOF(Zr).

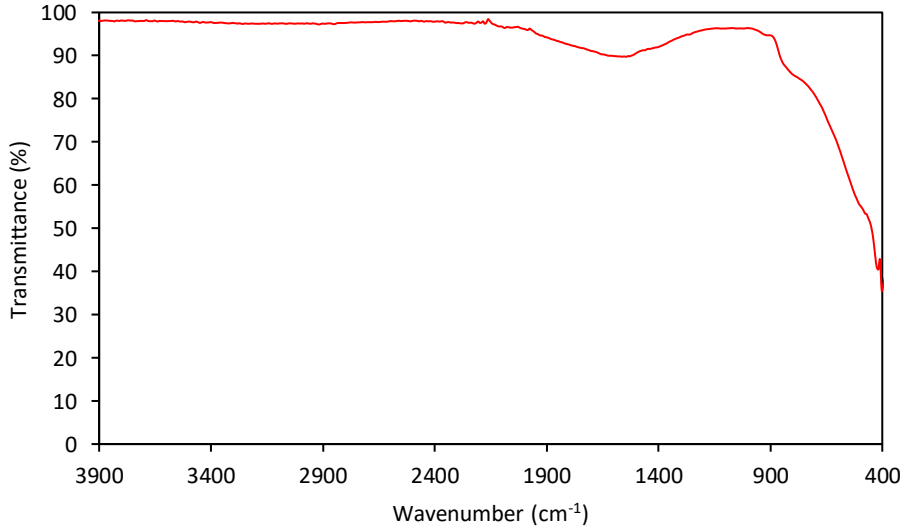

Fig. 5.19. FTIR spectrum of NTs TiO_2-MOF(Fe).

5.3.5. Cyclic Voltammetry (CV)

Cyclic voltammetry (CV) was employed to analyze the electrochemical behavior of the synthesized electrodes. CV measurements were carried out using a three-electrode system, where the working electrode was the TiO_2 NTs-based electrode, the counter electrode a platinum wire, and the reference electrode an Ag/AgCl (3.0 M KCl), in a KOH 0.10 M electrolyte solution.

The alkaline electrolyte was chosen based on the research conducted by Raut et al. (2016), where different electrolytes were tested for the characterization of TiO_2 NTs and it was found that a KOH electrolyte gave the largest current with double of the specific capacitance due to the high ionic mobility and small diameter of hydrated sphere of K^+ that results in a higher ionic conductivity.

The bare TiO_2 NTs electrode was first characterized in a potential range from -1.0 to 0.0 V at different scan rates: 20, 50, 100, and 200 mV/s. The resulting voltammograms are presented in **Fig. 5.20.** The TiO_2 NT array exhibits redox peaks around -0.7 V, possibly ascribed to the transition between TiO_2 and $Ti(OH)_3$ ($Ti^{+4} \leftrightarrow Ti^{+3}$), that indicate a pseudocapacitive behavior. It can be observed that the voltametric current increases with the scan rate, maintaining the redox potential, this shows that the pseudocapacitive behavior is surface controlled and that the electrolyte ions have a fast diffusion into the NT array (Raut et al., 2016).

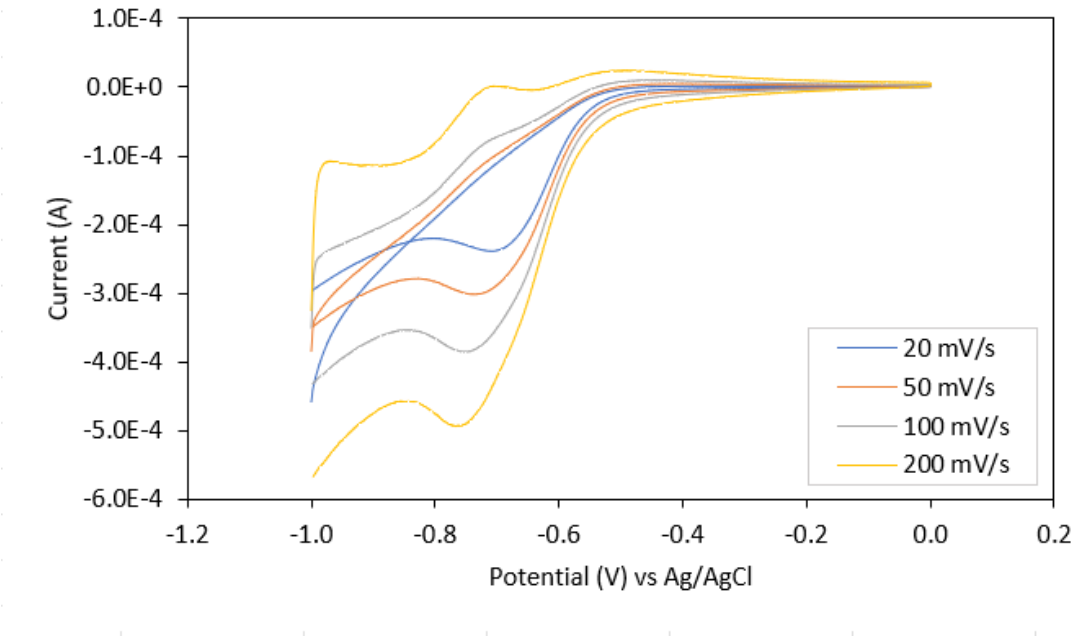

Fig. 5.20. CV characterization of bare TiO_2 NTs electrode.

CV measurements for MOF-modified TiO_2 NTs electrodes were done in a potential window of -0.6 – 1.0 V, using the same system and under the same conditions. **Fig. 5.21.** and **Fig. 5.22.** present the obtained voltammograms of TiO_2 NTs-MOF(Zr) and TiO_2 NTs-MOF(Fe) electrodes, respectively, at different scan rates (from 20 to 200 mV/s). The differences between these voltammograms and that of the bare TiO_2 NTs electrode arise from the redox processes attributed to the framework.

In both voltammograms, the oxidation peak of the TiO_2 NTs shifted to more positive potentials, around -0.5 V, and the reduction peak did not appear anymore. These could imply that the presence of the MOF altered the electrochemical properties of the electrode, resulting in changes in the redox processes taking place on the surface of the electrode. The shift in the oxidation peak suggests that the MOF altered the energetics of the oxidation reaction of the titanium, making it easier to oxidize this species. On the other hand, the disappearance of the reduction peak may be because the MOF is inhibiting

the reduction reaction of titanium. The voltammograms also presented a current density increase with the increase of the scan rate, due to a faster rate of electron transfer.

Besides the positive shift in the oxidation peak, an increase in the oxidation peak current is also observed in both TiO_2 NTs-MOF voltammograms. At a scan rate of 200 mV/s, the bare TiO_2 NTs oxidation peak had a current of 1.92E-06 A; in the TiO_2 NTs-MOF(Zr) and TiO_2 NTs-MOF(Fe) the peak current increased to 3.71E-05 and 3.01E-04, respectively. This could suggest that the electrochemical active surface area of the MOF-modified electrodes is larger, that the concentration of electroactive species is greater, or that there was a change in the reaction mechanism; this could improve the electrocatalytical performance of the electrodes (Chen et al., 2022).

In the CV of TiO_2 NTs-MOF(Zr) (**Fig. 5.21.**), apart from the oxidation peak, we obtained a fairly narrow electrochemical active area, which is in agreement with reported cyclic voltammograms of UiO-66(Zr) MOF and its nanocomposites (Chen et al., 2022; Gamal et al., 2023; BoorboorAjdari et al., 2022).

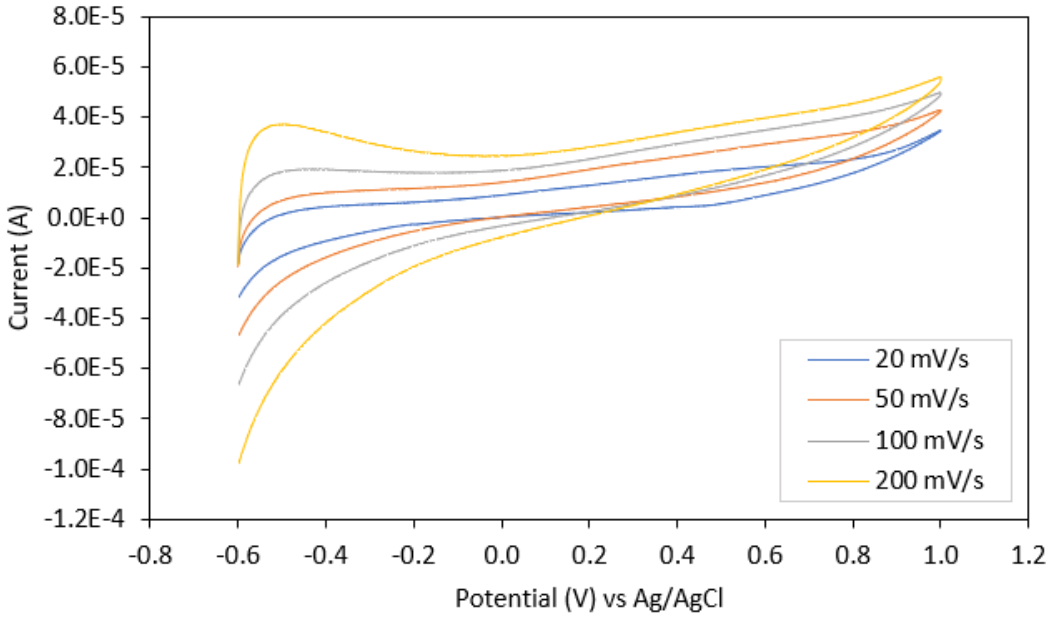

Fig. 5.21. CV characterization of modified TiO_2 NTs-MOF(Zr) electrode.

The CV of TiO_2 NTs-MOF(Fe) electrode (**Fig. 5.22.**) presented the highest anodic peak current. A small cathodic peak can be observed around 0.0 – 0.3 V, this reduction peak presents a negative shift with the increase of the scan rate. This voltammogram possess an even narrower shape than the MOF(Zr)-modified electrode, which indicates a small potential window for redox reactions. The obtained voltammogram is in accordance with reported CV characterization of MIL-101(Fe) MOF and its composites (Wu et al., 2022; Günduğar & Semerci, 2022; Safari & Mazloom, 2023).

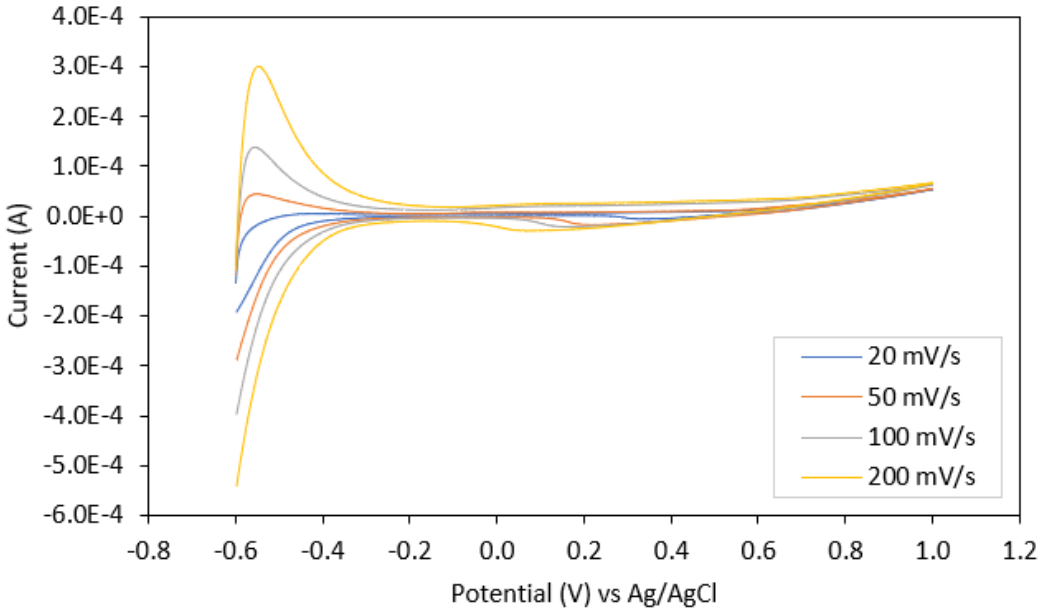

Fig. 5.22. CV characterization of modified TiO_2 NTs-MOF(Fe) electrode.

Further CV characterization of the electrodes was done throughout the experimental section to investigate the changes in the electrochemical properties after degradation processes. The CV measurements were performed under the same conditions (electrode system, electrolyte, and equipment), in a potential range of -1.0 to 1.0 V.

5.4. PEC degradation of methyl red

To examine the degradation efficiency of the TiO_2 NTs-MOF(Zr) electrodes, the degradation of the azo dye methyl red (15 ppm solution in H_2SO_4 0.5 M) was first carried out through PEC, using an UV lamp and a potentiostat. A three-electrode system was assembled, where the working electrode was the TiO_2 NTs-MOF(Zr) electrode, the counter electrode a titanium wire, and the reference electrode a Hg/Hg_2SO_4 (3.0 M K_2SO_4); the system was kept in the dark under magnetic stirring and was cooled down by a circulating water bath (**Fig. 5.23.**).

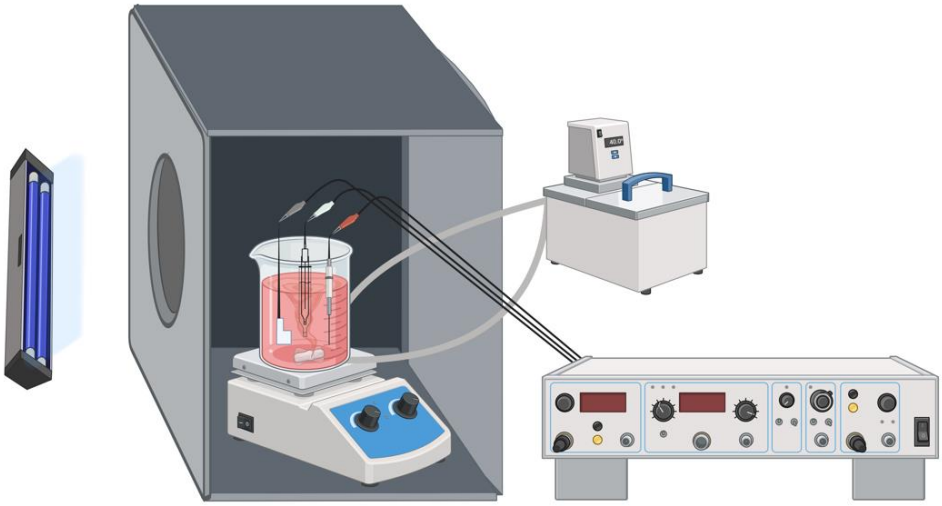

Fig. 5.23. PEC system for the degradation of methyl red.

Photocatalysis (PC) experiments were also conducted to analyze the role of light and voltage in the degradation of the azo dye. The photodegradation was carried out using only the UV lamp with a two-electrode system, using a titanium wire as the counter electrode (**Fig. 5.24.**).

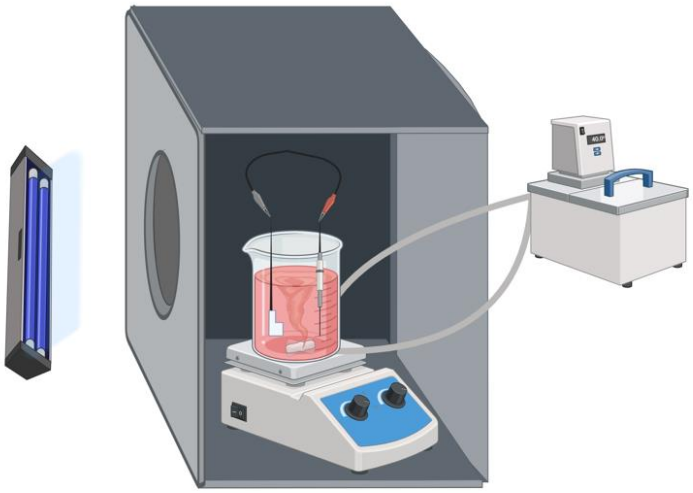

Fig. 5.24. PC system for the degradation of methyl red.

Cycling experiments were done to evaluate the reusability of the electrodes and its reproducibility was tested using different electrodes under the same conditions. To follow the degradation of the azo dye and to analyze the kinetics of these reactions, aliquots were taken throughout the degradation process (**Fig. 5.25.**) and subsequently analyzed by UV-Vis spectroscopy at 515 nm.

Fig. 5.25. Aliquots from the PEC degradation of methyl red using the TiO_2 NTs-MOF(Zr) electrode.

6. Results and discussion

6.1. Calibration curve of methyl red

Firstly, a calibration curve of the methyl red solution was obtained. For this purpose, five serial dilutions were prepared, with a dilution factor of 1/2, of an initial 15 ppm methyl red solution (in H_2SO_4 0.5 M). The absorbance of the initial solution and the serial dilutions were measured by UV-Vis spectroscopy, a graph of absorbance versus concentration was plotted to create the calibration curve by a linear regression. **Fig. 6.1.** presents the calibration curve of methyl red, from 15 ppm to 0.47 ppm.

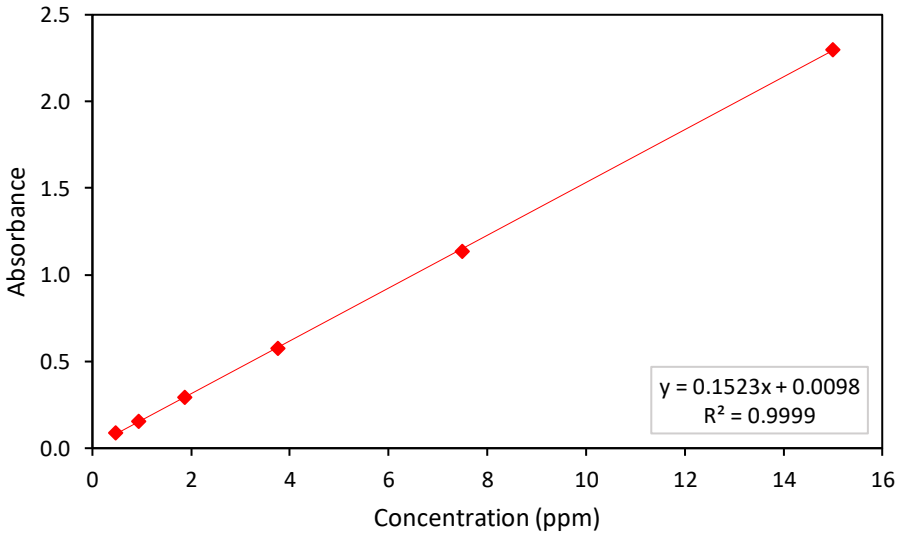

Fig. 6.1. Calibration curve of methyl red solution (H_2SO_4 0.5 M).

The high coefficient of determination ($R^2 = 0.9999$) indicates that the data fits well a linear model, having very low deviations from linearity. This shows that, at these concentrations, the methyl red solution follows the Lambert-Beer Law, which states that the absorbance of a solution is directly proportional to the concentration of the absorbance specie. Hence, the methyl red solution used for the degradation experiments had a concentration of 15 ppm and each aliquot taken during the degradation process was

diluted 1/2 with H_2SO_4 0.5 M in order to reduce the concentration of the absorbing species, ensuring accurate measurements of absorbance.

6.2. Preliminary experiments

Preliminary experiments were performed with both TiO_2 NTs-MOF(Fe) and TiO_2 NTs-MOF(Zr) electrodes to analyze which heterojunction had the higher PEC activity. These first tests were done with electrodes with an area of 0.5 cm^2, 10 mL of the methyl red solution (15 ppm), a potential of 1.8 V, and 3h of treatment. Given the objective of these preliminary experiments, the kinetics of the reactions was not followed, and only initial and final absorbance measurements were conducted.

Fig. 6.2. presents the absorbance spectrum of the solutions after the 3h of PEC degradation. The percentage of degradation attributed to each electrode is presented in **Table 6.1.** The Zr-MOF modified electrode presented the highest PEC degradation activity of the three materials. Based on these results, it was decided that the focus of the following experiments would be on the TiO_2 NTs-MOF(Zr) electrodes.

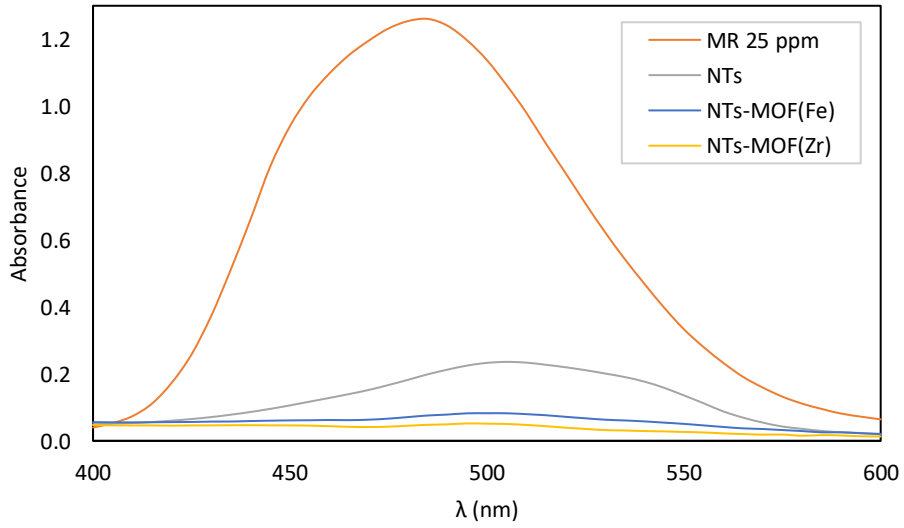

Fig. 6.2. Methyl red (MR) PEC degradation with different electrodes.

Table 6.1. Percentage of PEC degradation of each electrode.

Electrode	PEC degradation (%)
Bare TiO_2 NTs	82.12
TiO_2 NTs-MOF(Fe)	93.79
TiO_2 NTs-MOF(Zr)	96.06

A CV of the TiO_2 NTs-MOF(Zr) and the bare TiO_2 NTs was obtained from -1.0 V to 1.0 V, at a rate scan of 50 mV/s, to compare the redox properties of both electrodes (all posterior CV characterizations were performed under the same conditions for comparison purposes). From **Fig. 6.3.** we observe that the MOF-modified electrode voltammogram is displayed at lower currents, the lowering of the NTs signals confirms the growth of MOF crystals onto the TiO_2 NT arrays.

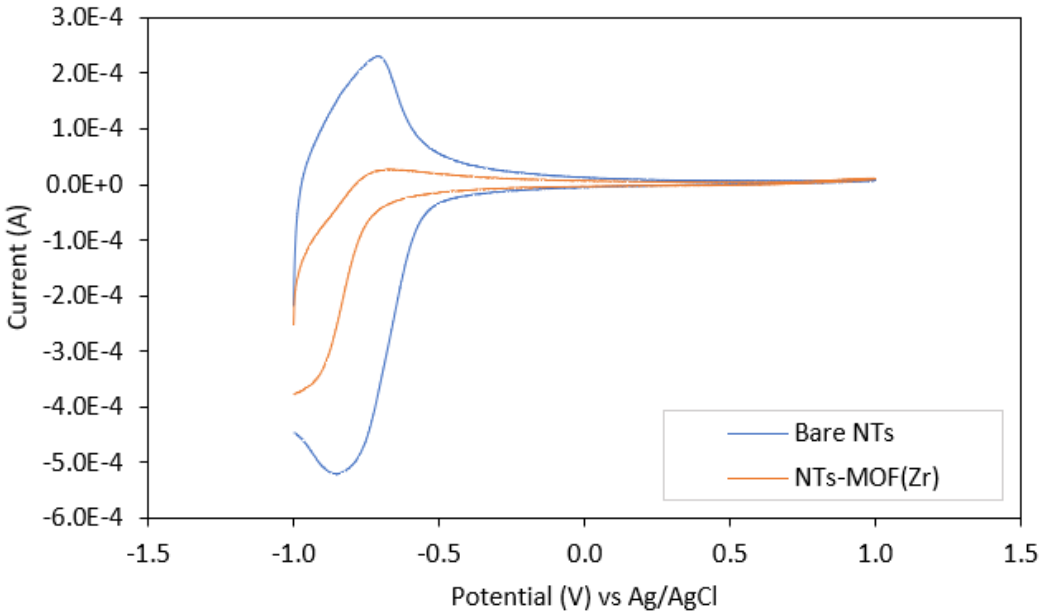

Fig. 6.3. CV comparison of bare TiO_2 NTs and modified TiO_2 NTs-MOF(Zr) electrodes.

6.3. PEC Degradation of methyl red

The PEC degradation of methyl red was carried out with TiO_2 NTs-MOF(Zr) 1.0 cm^2 electrodes, with 50 mL of methyl red (15 ppm) and a potential of 1.8 V for 3 cycling

experiments. An analogue experiment was performed using a bare-TiO_2 NTs electrode. Since, following the Lambert-Beer Law, the concentration of the solution is directly proportional to its absorbance, the degradation was measured through the change of UV-Vis absorbance. The absorbance (A) values were normalized by dividing the absorbance at any given time by the initial absorbance of the solution (A_t/A_0). The normalize absorbance, in function of time, obtained from these experiments are presented in **Fig. 6.4.** and the percentage of degradation of each PEC cycle is shown in **Table 6.2**.

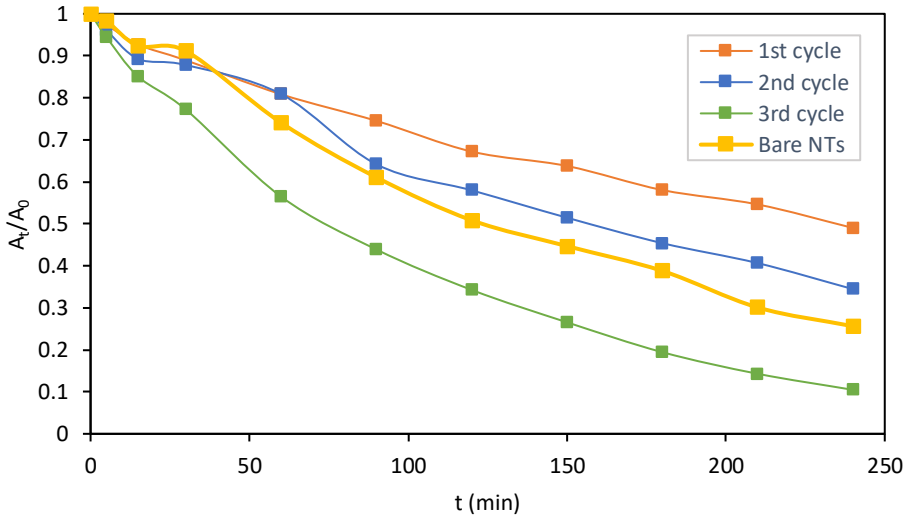

Fig. 6.4. Cyclic experiments of the PEC degradation of methyl red (1.8 V) with TiO_2 NTs-MOF(Zr) and its comparison with the bare TiO_2 NTs electrode.

Table 6.2. Percentage of PEC degradation at 1.8 V.

Electrode	PEC degradation (%)
TiO_2 NTs-MOF(Zr) 1st cycle	50.99
TiO_2 NTs-MOF(Zr) 2nd cycle	65.55
TiO_2 NTs-MOF(Zr) 3rd cycle	89.53
Bare TiO_2 NTs	74.38

The PEC degradation activity of the Zr MOF- modified electrode improved with the number of cycles, but when compared to the bare-NTs electrode, we can observe that only the last cycle of the nanocomposite had a higher activity. This could be explained by the progressive loss of the MOF material in the surface of the electrode throughout the degradation cycles due to the electric potential applied. It could be theorized that, initially, the high concentration of MOF in the surface of the electrode was obstructing the PEC activity of the TiO_2 NTs and once the excess of material was lost, the electrode presented a higher PEC activity. A doping effect from the UiO-66(Zr) MOF could also be present in the NT array.

CV measurements were obtained for the pristine TiO_2 NTs-MOF(Zr) electrode, the electrode after one cycle of PEC, and then after three cycles of PEC (**Fig. 6.5.**). This analysis showed that after one PEC cycle, the electrode displays the characteristic voltammogram of the bare TiO_2 NTs (presented in **Fig. 6.3.**), indicating the loss of the MOF material from the surface of the NT array. However, after three PEC cycles the shape of the voltammogram changes again, with reduce peak currents, further suggesting a possible doping effect coming from the Zr-MOF.

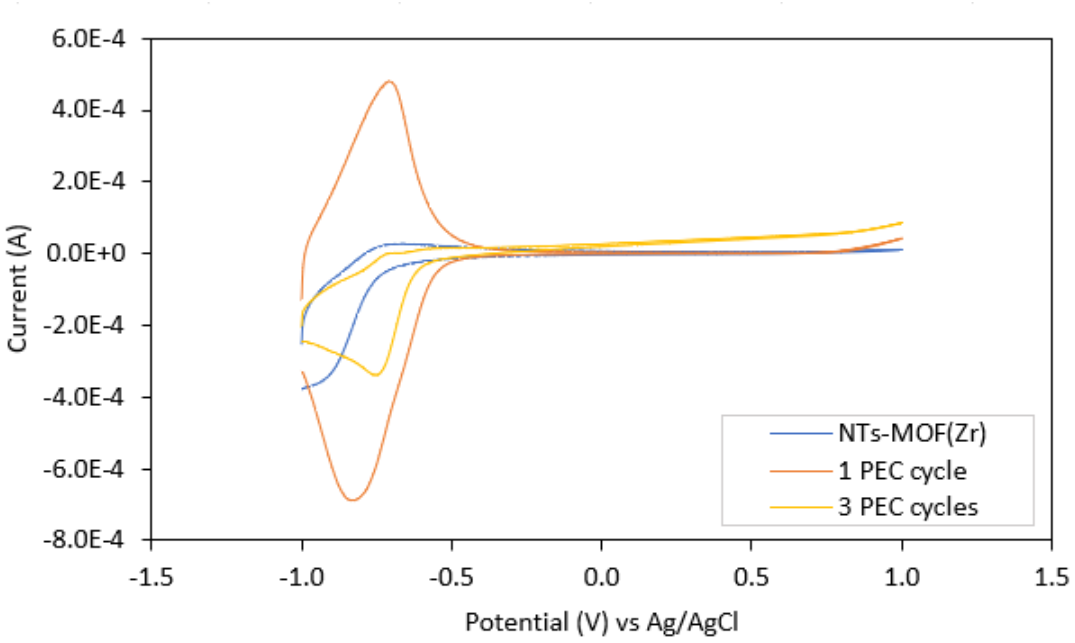

Fig. 6.5. CV of pristine TiO_2 NTs-MOF(Zr), after once cycle, and after three PEC cycles (1.8 V).

A CV characterization of the TiO_2 NTs-MOF(Zr) electrode was carried out at a higher potential range (-1.0 – 2.0 V) to analyze the electrochemical behavior of the electrode at the voltage used. **Fig. 6.6.** presents the obtained voltammogram, a small oxidation peak was found around 1.4 V, which could indicate that the material is not stable at higher potentials. For this reason, following PEC experiments were done with a lowering of potential, at 1.3 V.

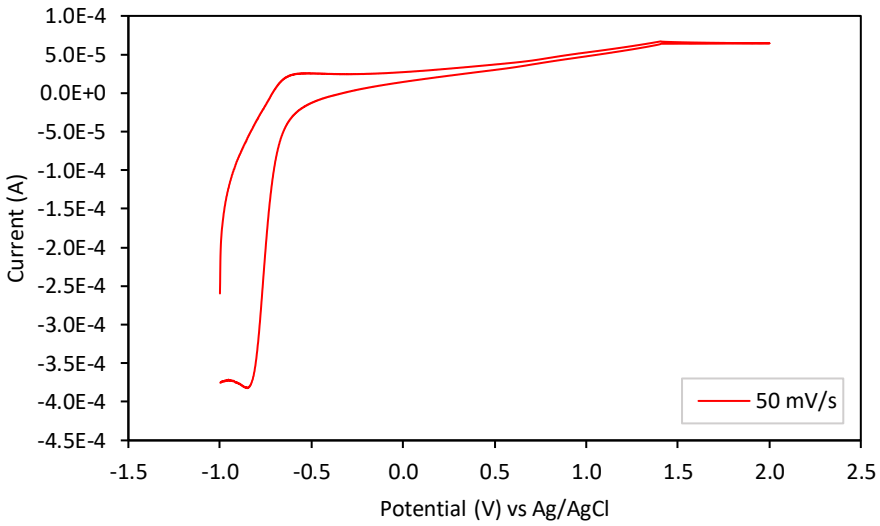

Fig. 6.6. CV of pristine TiO_2 NTs-MOF(Zr).

The same PEC system was used for 5 cycling degradation experiments using a new TiO_2 NTs-MOF(Zr) electrode and applying an electric potential of 1.3 V. No relationship between the number of cycles and the PEC degradation activity was found. For kinetic evaluation and comparison purposes, only three of the cycles are presented in **Fig. 6.7.** The complete results of the 5-cycle PEC degradation tests of methyl red are presented in **Annex 1**. We find that the PEC degradation efficiency of the MOF-modified electrode was greater than the bare TiO_2 NTs in all three cycles, even if a relationship between the number of cycles and the percentage of degradation was not observed (**Table 6.3.**). These results show that, with a lowering in the potential, the Zr-MOF material is more stable.

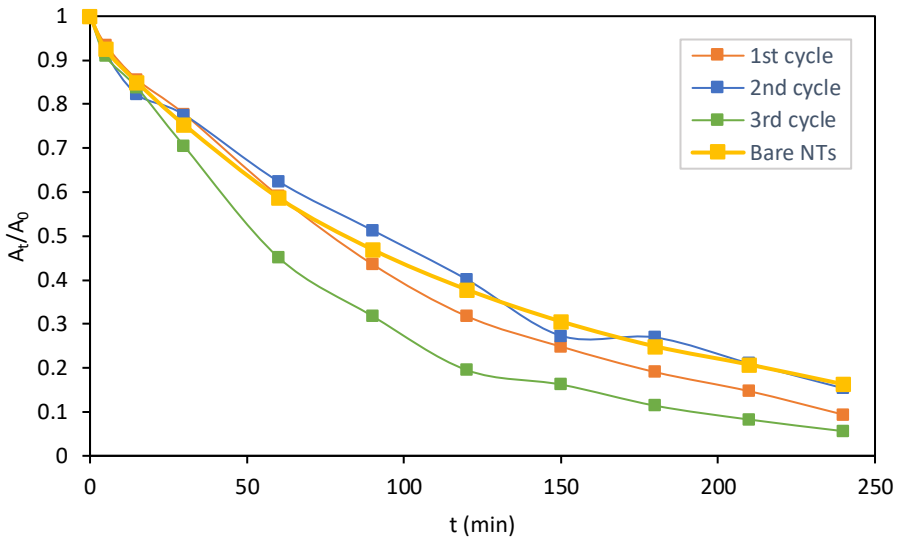

Fig. 6.7. Cyclic experiments of the PEC degradation of methyl red (1.3 V) with TiO_2 NTs-MOF(Zr) and its comparison with the bare TiO_2 NTs electrode.

Table 6.3. Percentage of PEC degradation at 1.3 V.

Electrode	PEC degradation (%)
TiO_2 NTs-MOF(Zr) 1st cycle	90.65
TiO_2 NTs-MOF(Zr) 2nd cycle	84.66
TiO_2 NTs-MOF(Zr) 3rd cycle	94.49
Bare TiO_2 NTs	83.73

6.4. Photocatalytic (PC) degradation of methyl red

To analyze the role of the UV light in the degradation reaction, photocatalytic (PC) experiments were performed. The experiments were carried out using the same system as the PEC test, only without applying a potential, during five PC degradation cycles with the TiO_2 NTs-MOF(Zr) electrode. Once again, no relationship was found between the number of cycles and the degradation efficiency of the electrode; hence, only three cycles were taken into consideration, for comparison purposes. The complete results of the 5-cycle PC degradation tests of methyl red are presented in **Annex 2**. The degradation

results are presented in **Fig. 6.8.** and **Table 6.4.** Compared to PEC results, a lowering in the degradation efficiency can be observed, demonstrating the enhancement that the potential represents in PEC processes.

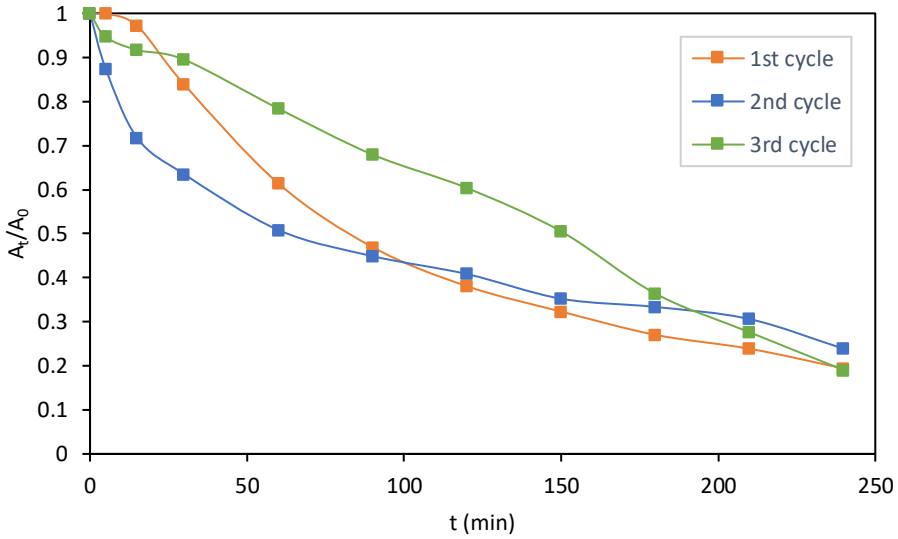

Fig. 6.8. Cyclic experiments of the PC degradation of methyl red with TiO_2 NTs-MOF(Zr).

Table 6.4. Percentage of PC degradation of TiO_2 NTs-MOF(Zr).

Electrode	PC degradation (%)
TiO_2 NTs-MOF(Zr) 1st cycle	80.60
TiO_2 NTs-MOF(Zr) 2nd cycle	76.14
TiO_2 NTs-MOF(Zr) 3rd cycle	80.97

For comparison, the same three-cycles PC degradation test was carried out with the bare TiO_2 NTs electrode. The results (**Fig. 6.9.**, **Table 6.5.**) showed that the MOF modification of the NT array has a positive impact in the PC activity of the electrode, obtaining higher percentages of degradation in the test with the TiO_2 NTs-MOF(Zr) electrode (76 - 81 %) compared to the bare TiO_2 NTs (62 – 78%). Moreover, the cycling experiments of the TiO_2 NTs indicate that the NT array has a higher PC activity with each

cycle, this could be attributed to a surface activation or processes of adsorption/desorption on the electrodes surface.

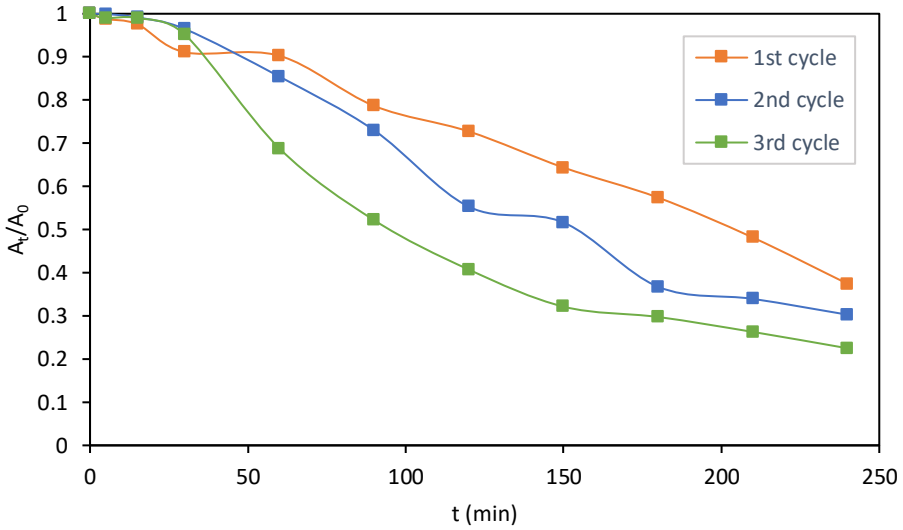

Fig. 6.9. Cyclic experiments of the PC degradation of methyl red with bare TiO_2 NTs.

Table 6.5. Percentage of PC degradation of bare TiO_2 NTs.

Electrode	PC degradation (%)
TiO_2 NTs 1st cycle	62.58
TiO_2 NTs 2nd cycle	69.73
TiO_2 NTs 3rd cycle	77.51

To analyze the reproducibility of the PC degradation of methyl red using the TiO_2 NTs-MOF(Zr), three different electrodes were tested. Results are presented in **Fig. 6.10.** and **Table 6.6.** The electrodes presented a PC degradation activity from 74-86 %. The difference in the degradation efficiency could be due to the amount of MOF present in the sample. As discussed previously, the proportion of MOF deposited onto the electrode through the solvothermal treatment was not constant in every synthesis, this was confirmed through multiple EDX analysis.

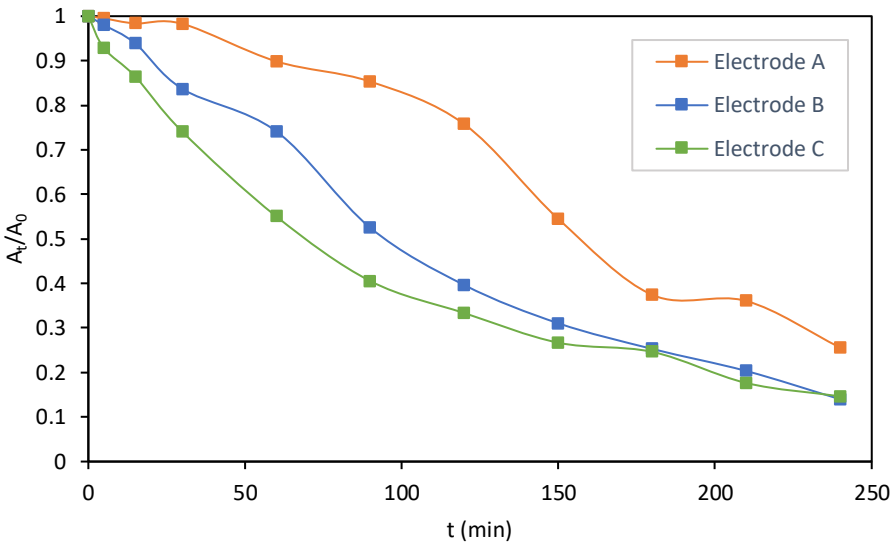

Fig. 6.10. PC degradation of methyl red with different TiO_2 NTs-MOF(Zr) electrodes.

Table 6.6. Percentage of PC degradation of different TiO_2 NTs-MOF(Zr).

Electrode	PC degradation (%)
A. TiO_2 NTs-MOF(Zr)	74.43
B. TiO_2 NTs-MOF(Zr)	86.03
C. TiO_2 NTs-MOF(Zr)	85.36

6.5. PEC and PC degradation activity

The results of the presented three-cycle experiments of PEC at 1.8 V, PEC at 1.3 V, and PC degradation with the TiO_2 NTs-MOF(Zr) electrode were compared to analyze the role of the potential and the UV light in the degradation process, and to determine which conditions are the optimal for the enhancement of the degradation of methyl red. From the three cycles, a percentage average of degradation was obtained, **Table 6.7.** presents these results. The best degradation activity for the (Zr)MOF-modified electrode was obtained with a PEC system, using a potential of 1.3 V. This shows the enhancement that the degradation process can have at low voltages.

Nevertheless, the advantage of focusing on PC processes lies in the positive impact on energy consumption, not needing any additional electric energy, and being a simpler and more energy efficient process. Under a PC system, the TiO_2 NTs-MOF(Zr) showed an average of 79.24%; compared to the degradation efficiency of the bare TiO_2 NTs electrode (69,94%), we observe an enhancement in the degradation of the electrode by a 10%.

Table 6.7. Degradation activity average of TiO_2 NTs-MOF(Zr) under different processes.

Type of degradation	Degradation avg. (%)
PEC (1.8 V)	68.69
PEC (1.3 V)	89.93
PC	79.24

In **Fig. 6.11.** and **Fig. 6.12.**, a comparison between the first cycle of the TiO_2 NTs-MOF(Zr) and the bare TiO_2 NTs electrodes, respectively, under the different systems is presented. Once more, a greater degradation efficiency is obtained with a PEC process at 1.3 V for both electrodes. But we can clearly see the enhancement that the MOF structure brings when using a PC system, improving the degradation of the bare NTs by 12% (from 25.57% to 37.42%).

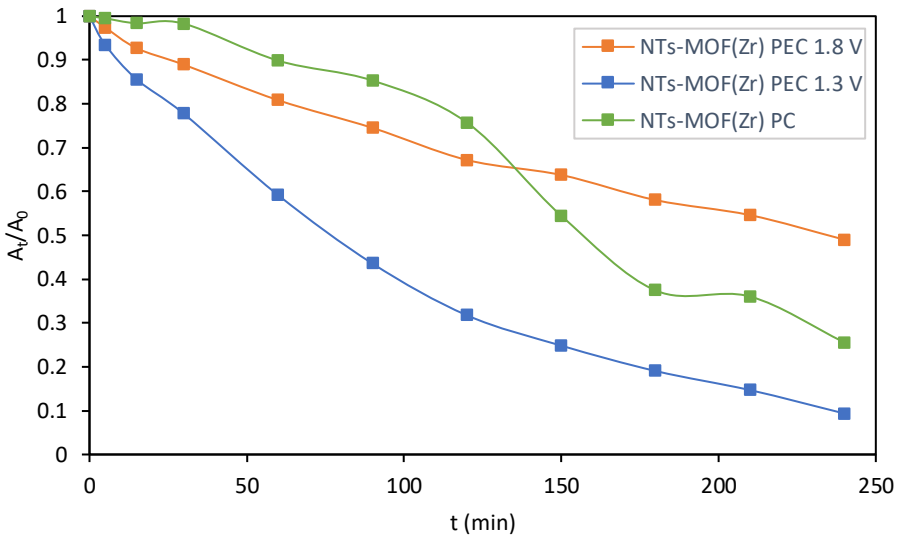

Fig. 6.11. First cycles of PEC and PC degradation of the TiO_2 NTs-MOF(Zr) electrode.

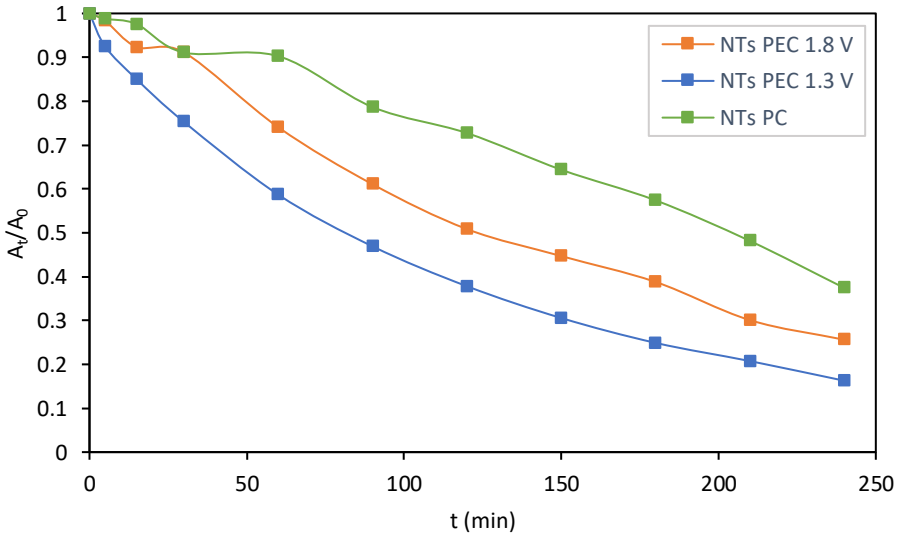

Fig. 6.12. First cycles of PEC and PC degradation of the bare TiO_2 NTs electrode.

CV were obtained for the two used TiO_2 NTs-MOF(Zr) electrodes, after 5 PEC (1.3 V) cycles and 5 PC cycles. The voltammograms were compared with that of the pristine TiO_2 NTs-MOF(Zr) electrode (**Fig. 6.13**). As previously discussed, it appears that after PEC cyclic experiments the electrode suffers from a loss of MOF crystals at the

surface of the NT array, producing a voltammogram with peaks corresponding to the TiO_2 NTs. But the PC cycling experiments seemed to have a different impact on the electrochemical properties of the electrode, resulting in a voltammogram with no peaks whatsoever. This could be explained by a decomposition of the MOF crystals at the surface of the electrode, covering the TiO_2 NTs and losing the electrochemical activity of the electrode.

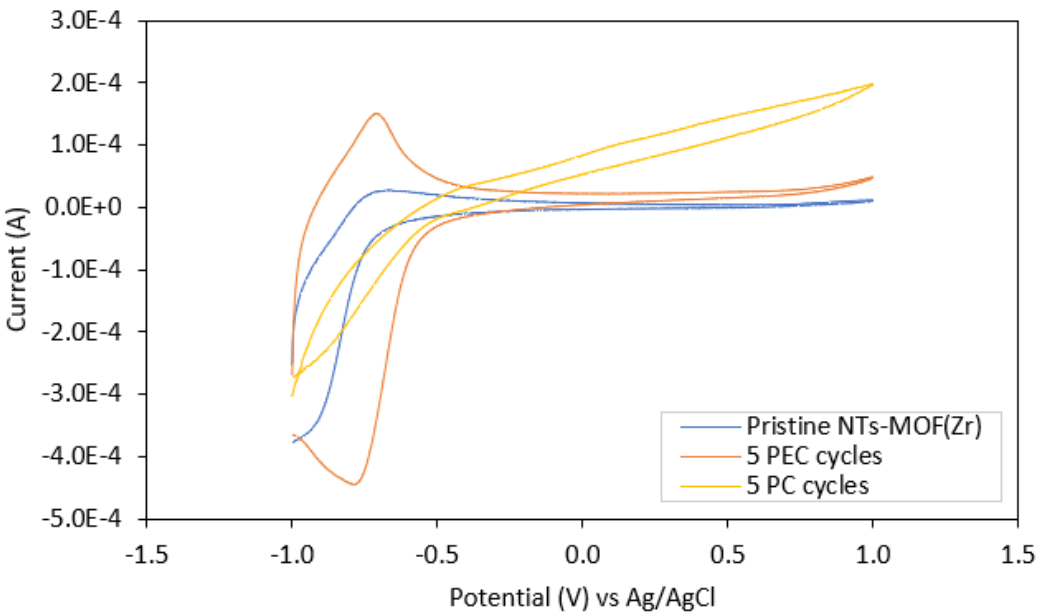

Fig. 6.13. CV of pristine TiO_2 NTs-MOF(Zr), after 5 PEC cycles, and after 5 PC cycles.

6.6. Degradation kinetics

To evaluate the kinetics of the degradation reactions with the TiO_2 NTs-MOF(Zr) electrode, the data obtained from the UV-Vis analysis was presented as a function of time and then fitted to the different models of reaction orders, considering that the absorbance of methyl red (MR) is proportional to the concentration of this analyte (A = [MR]), following the Lambert-Beer law.

6.6.1. Kinetics of PEC degradation

For the PEC degradation process with the TiO_2 NTs-MOF(Zr), for both 1.8 V and 1.3 V, it was found that the model that showed the best linear relationship corresponded to a first order reaction with the following rate law:

$$rate = kA$$

$$ln\frac{A_0}{A_t} = -kt$$

This means that the rate of the PEC degradation reaction is directly proportional to the concentration of the reactant (MR). Because the concentration of the reactant decreases exponentially over time, as the degradation reaction progresses, the rate of the reaction decreases. The half-time ($t_{1/2}$) of a first-order reaction is given by:

$$t_{1/2} = \frac{\ln(2)}{k}$$

Following the integrated rate law, the $\ln(A_0/A_t)$ was plotted against time. The results of the kinetic analysis of the PEC degradation of MR using the TiO_2 NTs-MOF(Zr) electrode at 1.8 V and 1.3 V are presented in **Table 6.8.** and **Table 6.9.**, respectively. The values of the rate constant (k) show that at a lower voltage, the degradation of methyl red is more kinetically favorable, with a faster rate reaction.

Table 6.8. Kinetics parameters of PEC (1.8V) degradation reaction with the TiO_2 NTs-MOF(Zr) electrode

Cycle	k (min^{-1})	$t_{1/2}$ (min)	R^2
1	0.0029	239.02	0.9957
2	0.0043	161.20	0.9944
3	0.0092	75.34	0.9987

Table 6.9. Kinetics parameters of PEC (1.3V) degradation reaction with the TiO_2 NTs-MOF(Zr) electrode.

Cycle	k (min^{-1})	$t_{1/2}$ (min)	R^2
1	0.0095	72.96	0.9970
2	0.0075	92.42	0.9917
3	0.0120	57.76	0.9964

6.6.2. Kinetics of PC degradation

For the PC degradation of methyl red with the TiO_2 NTs-MOF(Zr) electrode, no rate law model fitted all the data from the different degradation cycles. This supports the theory that the electrode material undergoes changes with each PC cycle, altering its properties and, therefore, the kinetics of the degradation reaction.

6.7. Adsorption test of the TiO_2 NTs-MOF(Zr) electrode

An adsorption test of methyl red was conducted using the TiO_2 NTs-MOF(Zr) electrode under the same conditions than the degradation experiments to test the adsorption properties of the MOF-modified electrode. Results of the adsorption test (**Fig. 6.14.**) showed very slight variations in the concentration of methyl red, indicating that the material did not present a strong adsorption of the analyte. We even observe normalized values above 1, which could signal to the presence of MOF in the solution due to a detachment of the framework from the electrode.

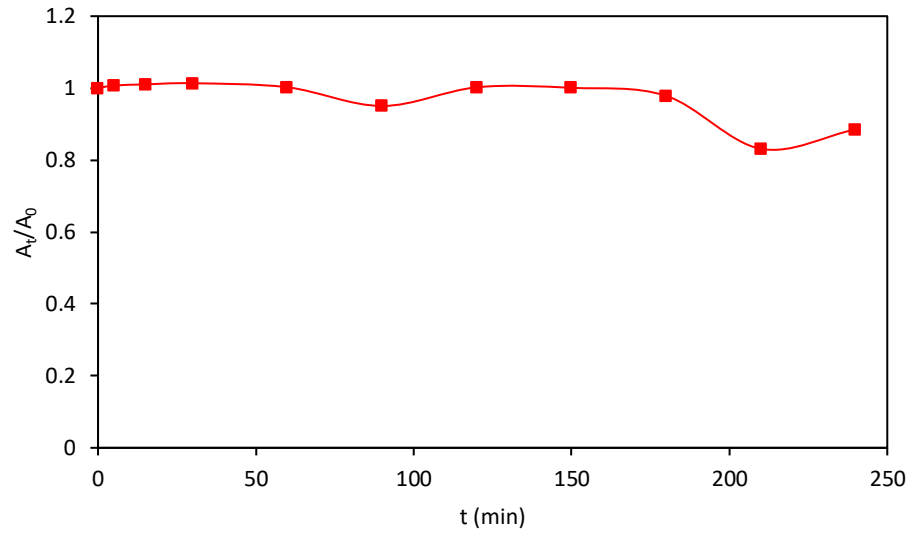

Fig. 6.14. Adsorption test of the TiO_2 NTs-MOF(Zr) electrode.

A purification process of the MOFs in the TiO_2 NTs electrodes was not performed, meaning that the non-volatile DMF solvent molecules may be occupying the porous of the material and, therefore, lowering the adsorption capacity of the framework. DMF is A solvent change to ethanol and a thermal treatment to evaporate the ethanol could allow to vacate the MOF structure.

6.8. EDX analysis post degradation cycles

EDX analysis were performed for the TiO_2 NTs-MOF(Zr) before and after five PEC and five PC cyclic experiments. Results showed a negligible concentration of Zr in the sample (lower than 0.02%) compared to an initial Zr concentration of up to 10% (atomic percentage). Since EDX is a surface-sensitive technique, it is likely that the emitted X-ray signals are only superficial. This means that the presence of the MOF inside or around the nanotube array may not be detected with this characterization technique.

The superficial MOF may undergo a loss during the degradation process; however, it is believed that the internal MOF in the electrode, or even a dopant effect

from a Zr derivative, are conserved inside the nanotube array. The improvement in the degradation efficiency of the bare TiO_2 NTs, even after multiple degradation cycles, supports this theory.

To test this premise, a mechanical scraping of one of the TiO_2 NTs-MOF(Zr) electrodes after five PC cycles was done to perform another EDX analysis both in the scraped electrode and in the shavings (**Fig. 6.15.**). The EDX results of the scraped electrode (**Fig. 6.15.a)** showed a small concentration of Zr in the sample (0.05%), compared to the result for the shavings (**Fig. 6.15.b)** that did not present any Zr whatsoever.

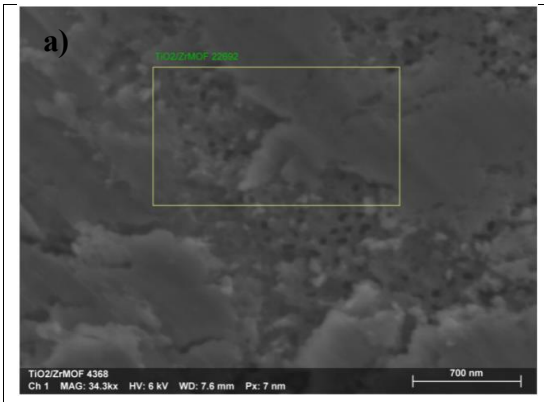

Element	At. No.	Netto	Mass [%]	Mass Norm. [%]	Atom [%]
Titanium	22	8077	55.65	55.65	29.55
Oxygen	8	15728	40.83	40.83	64.88
Fluorine	9	769	2.01	2.01	2.69
Carbon	6	802	1.34	1.34	2.84
Zirconium	40	42	0.17	0.17	0.05
		Sum	**100.00**	**100.00**	**100.00**

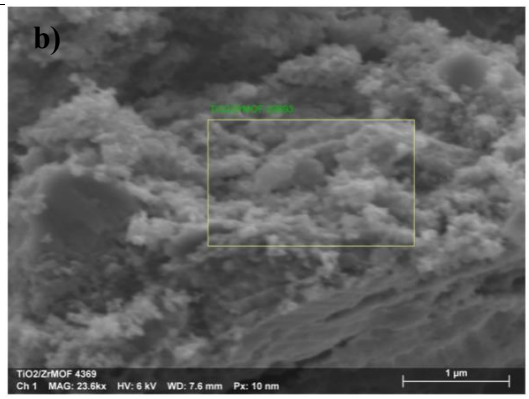

Element	At. No.	Netto	Mass [%]	Mass Norm. [%]	Atom [%]
Titanium	22	16051	57.19	57.19	30.75
Oxygen	8	28534	38.71	38.71	62.29
Fluorine	9	1729	2.32	2.32	3.15
Carbon	6	2073	1.78	1.78	3.81
Zirconium	40	0	0.00	0.00	0.00
		Sum	**100.00**	**100.00**	**100.00**

Fig. 6.15. EDX analysis of a) scraped electrode TiO_2 NTs-MOF(Zr) after 5 PC cycles and its b) scrapings.

These results exhibit the presence of Zr on the inside of the nanotube array, and a lack of material on the surface, showing that the internal MOF, or a Zr derivative, is preserved

during the degradation processes, consequently improving the PC activity of the electrode.

6.9. Preliminary tests of PC degradation with MOF(Zr)-NH_2

Aminated MOF(Zr) was synthesized for the modification of the TiO_2 NTs-based electrodes to analyze the effect that the amine groups have on the PC properties of the material in the degradation of methyl red. The amine groups are introduced to the structure through the organic ligand BDC-NH_2. Two types of electrodes were synthesized, one using only the aminated BDC (100% aminated) and the other using half the plain BDC ligand and half of the aminated ligand (50% aminated). EDX analysis of the aminated electrodes were conducted yet nitrogen was not correctly identified, this could be attributed to the low atomic number of nitrogen, that results in a minimal influence on X-ray intensities and the absence of characteristic EDX signals (Shaban et al., 2013).

An initial CV was carried out to compare the electrochemical properties of the MOF-modified electrodes: 0%, 50%, and 100% aminated **(Fig. 6.16.).** The different voltammogram shapes show the effect that the amine groups have on the electrochemical properties of the electrodes. The electrode aminated only by a 50% presented a wider voltammogram, which suggests that this material is redox-active ins a higher potential range.

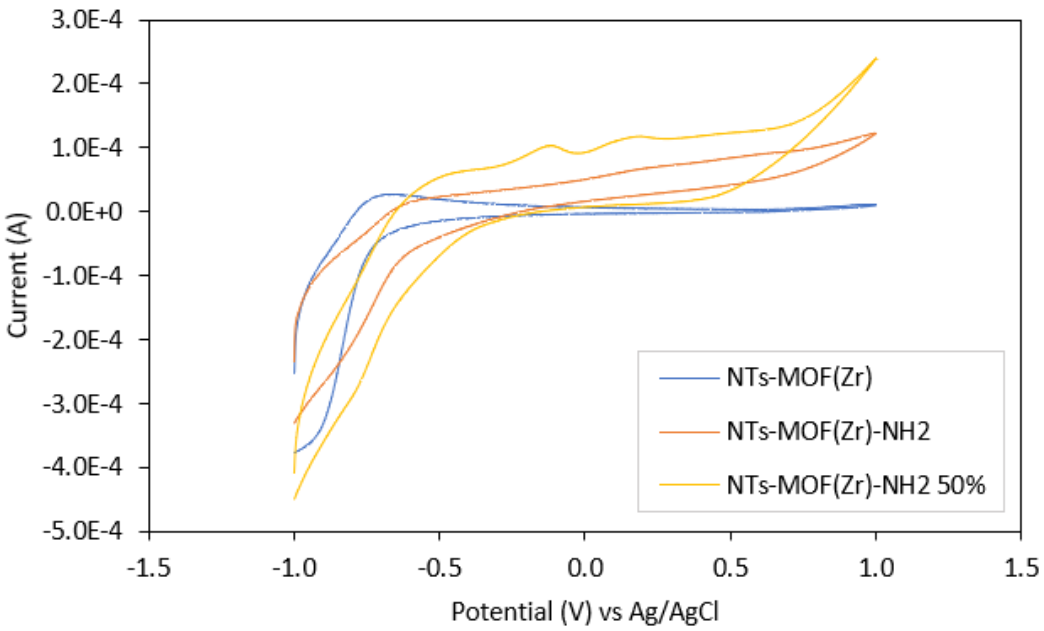

Fig. 6.16. CV comparison of TiO_2 NTs-MOF(Zr)-X modified electrodes (X = H, NH_2).

Three cyclic PC degradation experiments were conducted with the aminated electrodes. The result of the TiO_2 NTs-MOF(Zr)-NH_2 electrode are shown in **Fig. 6.17.** and **Table 6.10.** It can be observed that the degradation efficiency of this electrode improved with each cycle.

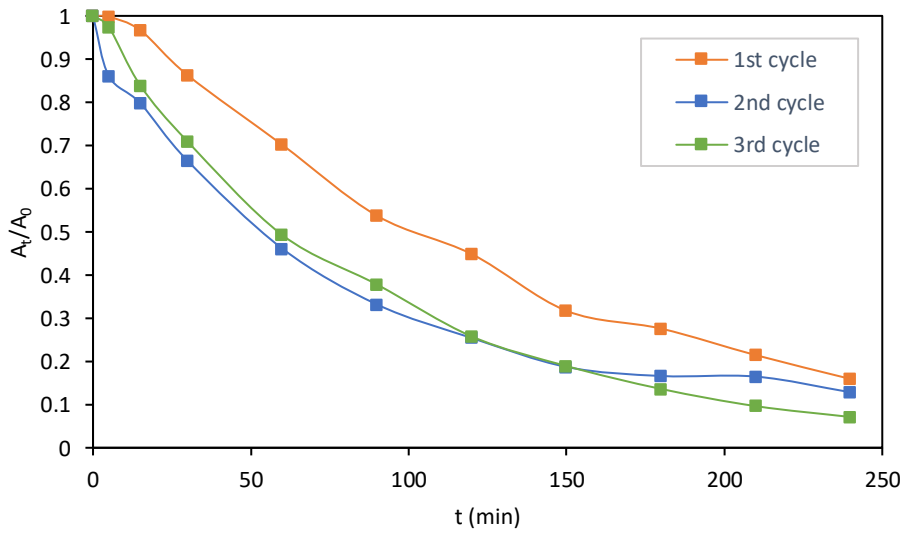

Fig. 6.17. Cyclic experiments of the PC degradation of methyl red with TiO_2 NTs-MOF(Zr)-NH_2.

Table 6.10. Percentage of PC degradation of TiO_2 NTs-MOF(Zr)-NH_2.

Electrode	PC degradation (%)
TiO_2 NTs-MOF(Zr)-NH_2 1st cycle	84.08
TiO_2 NTs-MOF(Zr)-NH_2 2nd cycle	87.15
TiO_2 NTs-MOF(Zr)-NH_2 3rd cycle	92.88

CV characterization was preformed after the three PC degradation cycles of the TiO_2 NTs-MOF(Zr)-NH_2 (**Fig. 6.18.**). A change in the shape of the voltammogram indicates that the material undergoes changes during the PC process that affect its electrochemical properties. A reduction peak appears after the three PC cycles, which can be attributed to the TiO_2 NTs, suggesting that the nanotubes may be uncovering due to a loss in the excess of the MOF.

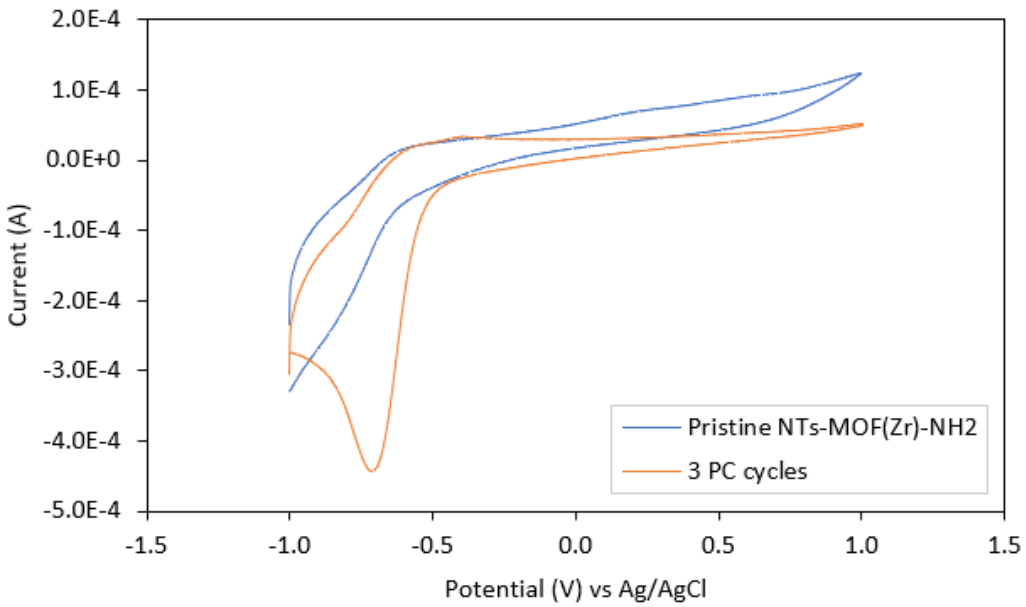

Fig. 6.18. CV of pristine TiO_2 NTs-MOF(Zr)-NH_2 and after 3 PC cycles.

The result of the three PC degradation cycles of methyl red with the TiO_2 NTs-MOF(Zr)-NH_2 50% electrode are shown in **Fig. 6.19.** and **Table 6.11.** Here, we obtained the best degradation efficiency (92%) in the first degradation cycle of all the electrodes tested. Nonetheless, the degradation of methyl red decreased with each cycle, this could point to a low stability of the material. Introducing an amino group into the MOF structure can cause an instability because of the pair of free electrons in the nitrogen, which grant the ligand molecule a polar nature pulling electrons and resulting in a lowering of the stability.

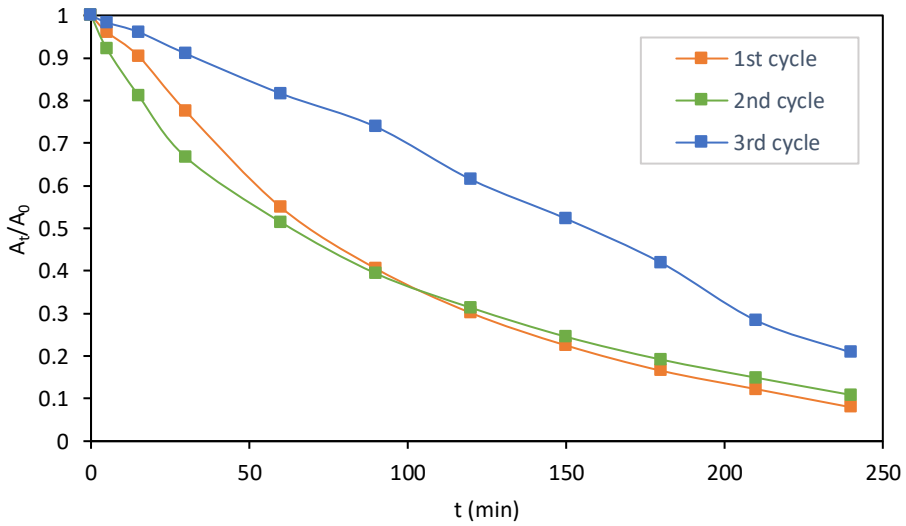

Fig. 6.19. Cyclic experiments of the PC degradation of methyl red with TiO_2 NTs-MOF(Zr)-NH_2 50%.

Table 6.11. Percentage of PC degradation of TiO_2 NTs-MOF(Zr)-NH_2.

Electrode	PC degradation (%)
TiO_2 NTs-MOF(Zr)-NH_2 50% 1st cycle	92.04
TiO_2 NTs-MOF(Zr)-NH_2 50% 2nd cycle	79.19
TiO_2 NTs-MOF(Zr)-NH_2 50% 3rd cycle	89.14

The CV of the TiO_2 NTs-MOF(Zr)-NH_2 50% electrode after the three PC cycles (**Fig. 6.20.**) presents the reduction peak characteristic of the TiO_2 NTs, just like in the case

of the 100% aminated electrode. Furthermore, a reduction of the redox active area of the voltammogram can also be observed, this is in agreement with the reduction of the degradation efficiency with each cycle.

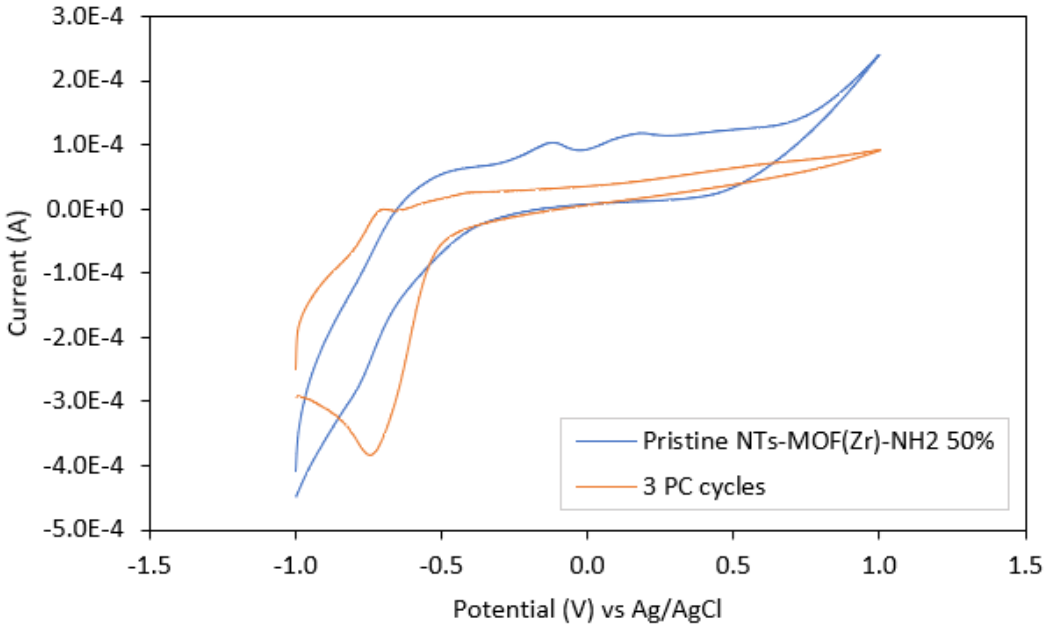

Fig. 6.20. CV of pristine TiO_2 NTs-MOF(Zr)-NH_2 50% and after 3 PC cycles.

6.9.1. Kinetics of the MOF(Zr)-NH_2 degradations

The kinetics of the PC degradation reactions with the aminated electrodes corresponded to a first order reaction. The kinetics parameters obtained for the TiO_2 NTs-MOF(Zr)-NH_2 and the TiO_2 NTs-MOF(Zr)-NH_2 50% electrodes are presented in **Table 6.12.** and **Table 6.13.**, respectively.

Table 6.12. Kinetics parameters of PC degradation reaction with the TiO_2 NTs-MOF(Zr)-NH_2 electrode.

Cycle	k (min^{-1})	$t_{1/2}$ (min)	R^2
1	0.0077	90.02	0.9959
2	0.0086	80.60	0.9622
3	0.0111	62.45	0.9995

Table 6.13. Kinetics parameters of PC degradation reaction with the TiO_2 NTs-MOF(Zr)-NH_2 50% electrode.

Cycle	k (min^{-1})	$t_{1/2}$ (min)	R^2
1	0.0104	66.65	0.9985
2	0.0061	113.63	0.9452
3	0.0089	77.88	0.9966

6.10. PC degradation results comparison

The first PC degradation cycles of all the tested TiO_2 NTs-based electrodes are presented in **Fig. 6.21.** The greatest improvement in the degradation of the azo dye methyl red was observed with the TiO_2 NTs-MOF(Zr)-NH_2 50% electrode, showing an improvement of 29% with respect to the bare TiO_2 NTs.

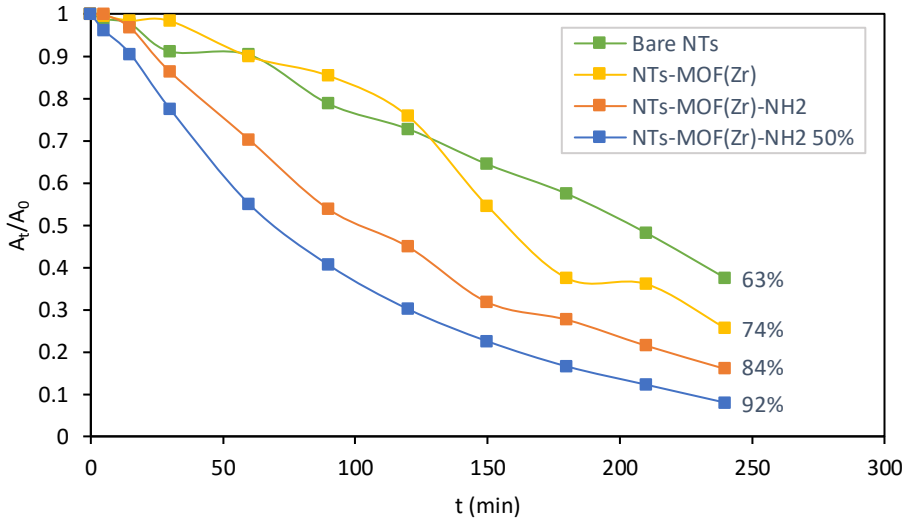

Fig. 6.21. First cycles of PC degradation of the TiO_2 NTs-based electrodes.

7. Conclusions and recommendations

In this work, we presented a simple solvothermal method for the modification of TiO_2 NTs-based electrodes, synthesized by electrochemical anodization, with metal organic-frameworks (MOFs). The electrodes were modified with the transition metals MOFs UiO-66(Zr) and MIL-101(Fe) to study the influence of the framework in the electrochemical properties of the electrode. The characterization of the prepared

electrodes confirmed the growth of the MOFs not only at the surface, but also inside and around the nanotube arrays. In addition, the individual analysis of each component of the electrodes (TiO_2 NTs, UiO-66(Zr), and MIL-101(Fe)) confirmed the correct synthesis of each material.

The photoelectrocatalytic (PEC) and photocatalytic (PC) activity of the electrodes was tested for the degradation of the azo dye methyl red, having an enhancement on the degradation efficiency of the TiO_2 NTs when the MOFs were present in the arrangement. The best degradation results with the TiO_2 NTs-MOF(Zr)-NH_2 under a PC degradation process. The highest degradation efficiency for the TiO_2 NTs-MOF(Zr) electrode was obtained with a PEC system at 1.3 V, owning to a better stability of the material at lower potentials. This demonstrates how a PEC approach can help lowering the recombination rate of photogenerated charge carriers in the semiconductor, having an enhancement on the degradation process. Nonetheless, the PC degradation presented the highest improvement when compared to bare TiO_2 NTs. The use of the TiO_2 NTs-MOF(Zr) heterojunction represents a positive impact on energy efficiency, not requiring high voltage powers and having good degradation even without an applied potential. The MOF-modified TiO_2 NT electrodes were also tested for the electrochemical detection of drugs, but results were not satisfactory.

The presence of the MOF in the electrodes had a synergistic effect with the TiO_2 NTs, but an excess of the material at the surface of the NT array can obstruct the electrochemical activity of the TiO_2 structures. Results showed that the MOF-modified electrode was not a stable material, undergoing structural or composition changes that affected the electrochemical properties of the electrode. It is expected that this work provides guidance for future photelectrocatalysts design. MOFs could be used as

precursors for the integration of metal oxides or metal derivatives onto the TiO_2 NTs arrays to further improve the PEC activity of the electrodes.

Since MOFs structures usually have a low physicochemical stability and low electrocatalytical performance, due to a deficient electrical conductivity, the low stability of the MOF can result in the decomposition of the material or even the loss of it, but this effect is mostly observed in the surface of the NT arrays. Characterization analysis showed a growth of the MOF inside and in between the TiO_2 NTs, having a possible dopant or modification effect of a Zr-derivative on the electrode. Overall, the MOF-modified electrodes presented an enhanced PEC and PC degradation activity, compared to the bare TiO_2 NTs electrode.

Further studies should focus on the improvement of the physicochemical stability of the framework, to enhance the reproducibility and reusability of the electrodes, which could be achieved by additional functionalization of the MOF. PC degradation experiments should be conducted under solar light irradiation to study the possible enhancement of PC activity to the visible light region that the MOF could induce in the electrode. Bare UiO-66(Zr) MOF presents a white coloration, but its aminated form showed a pale-yellow tonality, suggesting activity under visible light. What's more, the intense orange color of the MIL-101(Fe) MOF also makes it a great option for solar PC testing.

8. Bibliography

Alavijeh, R. K., & Akhbari, K. (2020). Biocompatible MIL-101(Fe) as a Smart Carrier with High Loading Potential and Sustained Release of Curcumin. *Inorganic Chemistry*. https://doi.org/10.1021/acs.inorgchem.9b02756

Aliofkhazraei, M., & Makhlouf, A. S. H. (Eds.). (2016). *Handbook of Nanoelectrochemistry: Electrochemical Synthesis Methods, Properties, and Characterization Techniques*. Springer International Publishing. https://doi.org/10.1007/978-3-319-15266-0

Almáši, M., Zeleňák, V., Palotai, P., Beňová, E., & Zeleňáková, A. (2018). Metal-organic framework MIL-101(Fe)-NH2 functionalized with different long-chain polyamines as drug delivery system. *Inorganic Chemistry Communications*, *93*, 115–120. https://doi.org/10.1016/j.inoche.2018.05.007

Ameta, R., Solanki, M. S., Benjamin, S., & Ameta, S. C. (2018). Chapter 6—Photocatalysis. In S. C. Ameta & R. Ameta (Eds.), *Advanced Oxidation Processes for Waste Water Treatment* (pp. 135–175). Academic Press. https://doi.org/10.1016/B978-0-12-810499-6.00006-1

Andrade, P. H. M., Henry, N., Volkringer, C., Loiseau, T., Vezin, H., Hureau, M., & Moissette, A. (2022). *ACS Applied Materials & Interfaces*, *14*(26), 29916–29933. https://doi.org/10.1021/acsami.2c07288

Ara, A., Khattak, R., Khan, M. S., Begum, B., Khan, S., & Han, C. (2022). Synthesis, Characterization, and Solar Photo-Activation of Chitosan-Modified Nickel Magnetite Bio-Composite for Degradation of Recalcitrant Organic Pollutants in Water. *Catalysts*, *12*(9), Article 9. https://doi.org/10.3390/catal12090983

Aribam, B., Konthoujam, B., Singh, P., & Thokchom, B. (2022). Chapter 2—Municipal water treatment with special emphasis on biosorption and nanoparticles. In P. Singh, J. P. Bassin, S. Rajkhowa, C. M. Hussain, & R. Oraon (Eds.), *Environmental Sustainability and Industries* (pp. 55–83). Elsevier. https://doi.org/10.1016/B978-0-323-90034-8.00003-8

Ashraf, M. A. (2017). Persistent organic pollutants (POPs): A global issue, a global challenge. *Environmental Science and Pollution Research*, *24*(5), 4223–4227. https://doi.org/10.1007/s11356-015-5225-9

Barbosa, A. D. S., Julião, D., Fernandes, D. M., Peixoto, A. F., Freire, C., de Castro, B., Granadeiro, C. M., Balula, S. S., & Cunha-Silva, L. (2017). Catalytic performance and electrochemical behaviour of Metal–organic frameworks: MIL-101(Fe) versus NH2-MIL-101(Fe). *Polyhedron*, *127*, 464–470. https://doi.org/10.1016/j.poly.2016.10.032

Bard, A. J., Faulkner, L. R., & White, H. S. (2022). *Electrochemical Methods: Fundamentals and Applications*. John Wiley & Sons.

Batten, S. R., Champness, N. R., Chen, X.-M., Garcia-Martinez, J., Kitagawa, S., Öhrström, L., O'Keeffe, M., Paik Suh, M., & Reedijk, J. (2013). Terminology of metal–organic frameworks and coordination polymers (IUPAC Recommendations 2013). *Pure and Applied Chemistry*, *85*(8), 1715–1724. https://doi.org/10.1351/PAC-REC-12-11-20

Beiranvand, M., Farhadi, S., & Mohammadi-Gholami, A. (2022). Adsorptive removal of tetracycline and ciprofloxacin drugs from water by using a magnetic rod-like hydroxyapatite and MIL-101(Fe) metal–organic framework nanocomposite. *RSC Advances*, *12*(53), 34438–34453. https://doi.org/10.1039/D2RA06213E

Bessegato, G. G., Guaraldo, T. T., de Brito, J. F., Brugnera, M. F., & Zanoni, M. V. B. (2015). Achievements and Trends in Photoelectrocatalysis: From Environmental to Energy Applications. *Electrocatalysis*, *6*(5), 415–441. https://doi.org/10.1007/s12678-015-0259-9

BoorboorAjdari, F., Izadpanah Ostad, M., Niknam Shahrak, M., Ershadi, M., Sadeghi Malek, S., Ghasemi, F., Zolfaghari, Y., & Ramakrishna, S. (2022). Investigating MCM-41/metal-

organic framework nanocomposites as silicon-containing electrodes for supercapacitor. *Surfaces and Interfaces*, *29*, 101796. https://doi.org/10.1016/j.surfin.2022.101796

Candia-Onfray, C., Irikura, K., Calzadilla, W., Rojas, S., Boldrin Zanoni, M. V., & Salazar, R. (2023). Degradation of contaminants of emerging concern in a secondary effluent using synthesized MOF-derived photoanodes: A comparative study between photo-, electro- and photoelectrocatalysis. *Chemosphere*, *315*, 137683. https://doi.org/10.1016/j.chemosphere.2022.137683

Cao, Y., Zhang, H., Song, F., Huang, T., Ji, J., Zhong, Q., Chu, W., & Xu, Q. (2018). UiO-66-NH2/GO Composite: Synthesis, Characterization and CO2 Adsorption Performance. *Materials*, *11*(4), Article 4. https://doi.org/10.3390/ma11040589

Cardoso, J. C., Stulp, S., de Brito, J. F., Flor, J. B. S., Frem, R. C. G., & Zanoni, M. V. B. (2018). MOFs based on ZIF-8 deposited on TiO2 nanotubes increase the surface adsorption of CO2 and its photoelectrocatalytic reduction to alcohols in aqueous media. *Applied Catalysis B: Environmental*, *225*, 563–573. https://doi.org/10.1016/j.apcatb.2017.12.013

Cerrón-Calle, G. A., Aranda-Aguirre, A. J., Luyo, C., Garcia-Segura, S., & Alarcón, H. (2019). Photoelectrocatalytic decolorization of azo dyes with nano-composite oxide layers of ZnO nanorods decorated with Ag nanoparticles. *Chemosphere*, *219*, 296–304. https://doi.org/10.1016/j.chemosphere.2018.12.003

Chen, P., Wang, M., Li, G., Jiang, H., Rezaeifard, A., Jafarpour, M., Wu, G., & Rao, B. (2022). Construction of ZIF-67-On-UiO-66 Catalysts as a Platform for Efficient Overall Water Splitting. *Inorganic Chemistry*, *61*(46), 18424–18433. https://doi.org/10.1021/acs.inorgchem.2c02522

Chimmikuttanda, S. P., Naik, A., Akple, M. S., & Singh, R. (2022). Chapter 10—Processing of hybrid TiO2 semiconducting materials and their environmental application. In D. Giannakoudakis, L. Meili, & I. Anastopoulos (Eds.), *Advanced Materials for Sustainable Environmental Remediation* (pp. 277–300). Elsevier. https://doi.org/10.1016/B978-0-323-90485-8.00011-4

Chung, K.-T. (2016). Azo dyes and human health: A review. *Journal of Environmental Science and Health, Part C*, *34*(4), 233–261. https://doi.org/10.1080/10590501.2016.1236602

Collins, J., Gourdin, G., & Qu, D. (2018). Chapter 3.23 - Modern Applications of Green Chemistry: Renewable Energy. In B. Török & T. Dransfield (Eds.), *Green Chemistry* (pp. 771–860). Elsevier. https://doi.org/10.1016/B978-0-12-809270-5.00028-5

Devi, L., Dalal, K., Manchala, S., Behera, K., Sharma, K. N., & Das, A. (2023). 11 - Nanostructured photoelectrochemical biosensors: Materials and applications. In A. Barhoum & Z. Altintas (Eds.), *Fundamentals of Sensor Technology* (pp. 265–284). Woodhead Publishing. https://doi.org/10.1016/B978-0-323-88431-0.00005-3

Dong, J., Zhang, X., Dong, X., Ng, K. H., Xie, Z., Chen, I.-W. P., Ng, Y. H., Huang, J., & Lai, Y. (2021). Coupled porosity and heterojunction engineering: MOF-derived porous Co3O4 embedded on TiO2 nanotube arrays for water remediation. *Chemosphere*, *274*, 129799. https://doi.org/10.1016/j.chemosphere.2021.129799

Duan, M.-J., Guan, Z., Ma, Y.-W., Wan, J.-Q., Wang, Y., & Qu, Y.-F. (2018). A novel catalyst of MIL-101(Fe) doped with Co and Cu as persulfate activator: Synthesis, characterization, and catalytic performance. *Chemical Papers*, *72*(1), 235–250. https://doi.org/10.1007/s11696-017-0276-7

Eliaz, N. (Ed.). (2012). *Applications of Electrochemistry and Nanotechnology in Biology and Medicine II* (Vol. 53). Springer US. https://doi.org/10.1007/978-1-4614-2137-5

Fakhri, A., Tyagi, I., & Karri, R. R. (2022). Chapter 20—Smart material-based micro/nanostructures for the detection and removal of water impurities. In I. Tyagi, J. Goscianska, M. H. Dehghani, & R. R. Karri (Eds.), *Sustainable Materials for Sensing and Remediation of Noxious Pollutants* (pp. 315–328). Elsevier. https://doi.org/10.1016/B978-0-323-99425-5.00012-8

Férey, G., Mellot-Draznieks, C., Serre, C., Millange, F., Dutour, J., Surblé, S., & Margiolaki, I. (2005). A Chromium Terephthalate-Based Solid with Unusually Large Pore Volumes and Surface Area. *Science*, *309*(5743), 2040–2042. https://doi.org/10.1126/science.1116275

Ferraz, E. R. A., Oliveira, G. A. R., Grando, M. D., Lizier, T. M., Zanoni, M. V. B., & Oliveira, D. P. (2013). Photoelectrocatalysis based on Ti/TiO2 nanotubes removes toxic properties of the azo dyes Disperse Red 1, Disperse Red 13 and Disperse Orange 1 from aqueous chloride samples. *Journal of Environmental Management*, *124*, 108–114. https://doi.org/10.1016/j.jenvman.2013.03.033

Frank, O., Zukalova, M., Laskova, B., Kürti, J., Koltai, J., & Kavan, L. (2012). Raman spectra of titanium dioxide (anatase, rutile) with identified oxygen isotopes (16, 17, 18). *Physical Chemistry Chemical Physics*, *14*(42), 14567–14572. https://doi.org/10.1039/C2CP42763J

Fujishima, A., & Honda, K. (1972). Electrochemical Photolysis of Water at a Semiconductor Electrode. *Nature*, *238*(5358), 37–38. https://doi.org/10.1038/238037a0

Gamal, S., Kospa, D. A., Kaid, M. M., El-Hakam, S. A., Ahmed, A. I., & Ibrahim, A. A. (2023). Fe-Co spinel oxides supported UiO-66-NH2 derived zirconia/ N-dopped porous hollow

carbon as an efficient oxygen reduction reaction electrocatalyst. *Journal of Environmental Chemical Engineering*, *11*(2), 109359. https://doi.org/10.1016/j.jece.2023.109359

Gao, J., Huang, Q., Wu, Y., Lan, Y.-Q., & Chen, B. (2021). Metal–Organic Frameworks for Photo/Electrocatalysis. *Advanced Energy and Sustainability Research*, *2*(8), 2100033. https://doi.org/10.1002/aesr.202100033

Garcia-Segura, S., & Brillas, E. (2017). Applied photoelectrocatalysis on the degradation of organic pollutants in wastewaters. *Journal of Photochemistry and Photobiology C: Photochemistry Reviews*, *31*, 1–35. https://doi.org/10.1016/j.jphotochemrev.2017.01.005

Garcia-Segura, S., Dosta, S., Guilemany, J. M., & Brillas, E. (2013). Solar photoelectrocatalytic degradation of Acid Orange 7 azo dye using a highly stable TiO2 photoanode synthesized by atmospheric plasma spray. *Applied Catalysis B: Environmental*, *132–133*, 142–150. https://doi.org/10.1016/j.apcatb.2012.11.037

Gecgel, C., Simsek, U. B., Gozmen, B., & Turabik, M. (2019). Comparison of MIL-101(Fe) and amine-functionalized MIL-101(Fe) as photocatalysts for the removal of imidacloprid in aqueous solution. *Journal of the Iranian Chemical Society*, *16*(8), 1735–1748. https://doi.org/10.1007/s13738-019-01647-w

Gong, J., Katz, M. J., & Kerton, F. M. (2018). Catalytic conversion of glucose to 5-hydroxymethylfurfural using zirconium-containing metal–organic frameworks using microwave heating. *RSC Advances*, *8*(55), 31618–31627. https://doi.org/10.1039/C8RA06021E

Grundmann, M. (2016). *The Physics of Semiconductors: An Introduction Including Nanophysics and Applications*. Springer International Publishing. https://doi.org/10.1007/978-3-319-23880-7

Günduğar, K., & Semerci, F. (2022). Compositing of MIL-101(Fe) with reduced graphene oxide and polyaniline for capacitive energy storage. *Materials Chemistry and Physics*, *278*, 125641. https://doi.org/10.1016/j.matchemphys.2021.125641

Guo, S., Chi, L., Zhao, T., Nan, Y., Sun, X., Huang, Y., Hou, B., & Wang, X. (2021). Construction of MOF/TiO2 nanocomposites with efficient visible-light-driven photocathodic protection. *Journal of Electroanalytical Chemistry*, *880*, 114915. https://doi.org/10.1016/j.jelechem.2020.114915

Hadi Dehghani, M., Karri, R. R., & Anastopoulos, I. (Eds.). (2022). Soil toxicity and remediation techniques. In *Pesticides Remediation Technologies from Water and Wastewater* (pp. i–iii). Elsevier. https://doi.org/10.1016/B978-0-323-90893-1.00020-9

Hariganesh, S., Vadivel, S., Maruthamani, D., & Rangabhashiyam, S. (2020). Chapter 12 - Disinfection by-products in drinking water: Detection and treatment methods. In M. N. V. Prasad (Ed.), *Disinfection By-products in Drinking Water* (pp. 279–304). Butterworth-Heinemann. https://doi.org/10.1016/B978-0-08-102977-0.00013-5

Harris, D. C. (2016). *Quantitative Chemical Analysis* (9th edition). W. H. Freeman.

Hoang Tran, T. N., Hoang Le, T., Kieu Thi Ta, H., Thi Dang, Y., Thuy Ho Nguyen, L., Hoang Le Doan, T., Fang, C.-K., Hwang, I.-S., Bach Phan, T., & Pham, N. K. (2021). C-AFM study on multi—Resistive switching modes observed in metal–organic frameworks thin films. *Organic Electronics*, *93*, 106136. https://doi.org/10.1016/j.orgel.2021.106136

Hu, H., Zhang, H., Chen, Y., & Ou, H. (2019). Enhanced photocatalysis using metal–organic framework MIL-101(Fe) for organophosphate degradation in water. *Environmental Science and Pollution Research*, *26*(24), 24720–24732. https://doi.org/10.1007/s11356-019-05649-2

Iijima, S. (1991). Helical microtubules of graphitic carbon. *Nature*, *354*(6348), Article 6348. https://doi.org/10.1038/354056a0

Ismail, N. A., Mat Amin, K. A., & Razali, M. H. (2018). Novel gellan gum incorporated TiO2 nanotubes film for skin tissue engineering. *Materials Letters*, *228*, 116–120. https://doi.org/10.1016/j.matlet.2018.05.140

IUPAC (Ed.). (2019). *The IUPAC Compendium of Chemical Terminology: The Gold Book* (4th ed.). International Union of Pure and Applied Chemistry (IUPAC). https://doi.org/10.1351/goldbook

Jia, M., Yang, Z., Xu, H., Song, P., Xiong, W., Cao, J., Zhang, Y., Xiang, Y., Hu, J., Zhou, C., Yang, Y., & Wang, W. (2020). Integrating N and F co-doped TiO2 nanotubes with ZIF-8 as photoelectrode for enhanced photo-electrocatalytic degradation of sulfamethazine. *Chemical Engineering Journal*, *388*, 124388. https://doi.org/10.1016/j.cej.2020.124388

Khudozhitkov, A. E., Arzumanov, S. S., Kolokolov, D. I., & Stepanov, A. G. (2021). UiO-66 (Zr) MOF as a Promising Material for Butane Isomers Separation: Evidence Based on the Analysis of the Adsorbed Alkanes Mobility by 2H NMR and Molecular Dynamics Simulation. *The Journal of Physical Chemistry C*, *125*(24), 13391–13400. https://doi.org/10.1021/acs.jpcc.1c02849

Kim, H.-G., Choi, K., Lee, K., Lee, S., Jung, K.-W., & Choi, J.-W. (2021). Controlling the Structural Robustness of Zirconium-Based Metal Organic Frameworks for Efficient

Adsorption on Tetracycline Antibiotics. *Water*, *13*(13), Article 13. https://doi.org/10.3390/w13131869

Lavacchi, A., Miller, H., & Vizza, F. (2013). *Nanotechnology in Electrocatalysis for Energy* (Vol. 170). Springer New York. https://doi.org/10.1007/978-1-4899-8059-5

Li, B., Gao, X., Zhang, H.-C., & Yuan, C. (2014). Energy Modeling of Electrochemical Anodization Process of Titanium Dioxide Nanotubes [dataset]. In *ACS Sustainable Chemistry & Engineering* (Vol. 2). https://doi.org/10.1021/sc400304h

Li, G., Lian, Z., Wang, W., Zhang, D., & Li, H. (2016). Nanotube-confinement induced size-controllable g-C3N4 quantum dots modified single-crystalline TiO2 nanotube arrays for stable synergetic photoelectrocatalysis. *Nano Energy*, *19*, 446–454. https://doi.org/10.1016/j.nanoen.2015.10.011

Li, L. (2020). The reaction mechanism of photoelectrocatalysis on the surface of TiO2 nanotube array electrode. *Asia-Pacific Journal of Chemical Engineering*, *15*(S1), e2511. https://doi.org/10.1002/apj.2511

Liu, S., Jiang, X., Waterhouse, G. I. N., Zhang, Z.-M., & Yu, L. (2022). Efficient photoelectrocatalytic degradation of azo-dyes over polypyrrole/titanium oxide/reduced graphene oxide electrodes under visible light: Performance evaluation and mechanism insights. *Chemosphere*, *288*, 132509. https://doi.org/10.1016/j.chemosphere.2021.132509

Liu, X., Dang, R., Dong, W., Huang, X., Tang, J., Gao, H., & Wang, G. (2017). A sandwich-like heterostructure of TiO2 nanosheets with MIL-100(Fe): A platform for efficient visible-light-driven photocatalysis. *Applied Catalysis B: Environmental*, *209*, 506–513. https://doi.org/10.1016/j.apcatb.2017.02.073

Liu, Z., He, W., Zhang, Q., Shapour, H., & Bakhtari, M. F. (2021). Preparation of a GO/MIL-101(Fe) Composite for the Removal of Methyl Orange from Aqueous Solution. *ACS Omega*, *6*(7), 4597–4608. https://doi.org/10.1021/acsomega.0c05091

Luttrell, T., Halpegamage, S., Tao, J., Kramer, A., Sutter, E., & Batzill, M. (2014). Why is anatase a better photocatalyst than rutile? - Model studies on epitaxial TiO2 films. *Scientific Reports*, *4*(1), Article 1. https://doi.org/10.1038/srep04043

Macák, J. M., Tsuchiya, H., & Schmuki, P. (2005). High-Aspect-Ratio TiO2 Nanotubes by Anodization of Titanium. *Angewandte Chemie International Edition*, *44*(14), 2100–2102. https://doi.org/10.1002/anie.200462459

Maksimchuk, N. V., Kovalenko, K. A., Fedin, V. P., & Kholdeeva, O. A. (2012). Cyclohexane selective oxidation over metal–organic frameworks of MIL-101 family: Superior catalytic activity and selectivity. *Chemical Communications*, *48*(54), 6812. https://doi.org/10.1039/c2cc31877f

Man, Z., Meng, Y., Lin, X., Dai, X., Wang, L., & Liu, D. (2022). Assembling UiO-66@TiO2 nanocomposites for efficient photocatalytic degradation of dimethyl sulfide. *Chemical Engineering Journal*, *431*, 133952. https://doi.org/10.1016/j.cej.2021.133952

Mirkin, M. V., & Amemiya, S. (2015). *Nanoelectrochemistry*.

Mohaghegh, N., Faraji, M., & Abedini, A. (2018). Highly efficient multifunctional Ag/TiO2 nanotubes/Ti plate coated with MIL-88B(Fe) as a photocatalyst, adsorbent, and disinfectant in water treatment. *Applied Physics A*, *125*(1), 25. https://doi.org/10.1007/s00339-018-2324-8

Moura, L., & Picão, R. C. (2022). Chapter 23 - Removal of antimicrobial resistance determinants from wastewater: A risk perspective on conventional and emerging technologies. In H. Sarma, D. C. Dominguez, & W.-Y. Lee (Eds.), *Emerging Contaminants in the Environment* (pp. 603–642). Elsevier. https://doi.org/10.1016/B978-0-323-85160-2.00023-8

Mukherjee, S., & Mergel, D. (2013). Thickness dependence of the growth of magnetron-sputtered TiO2 films studied by Raman and optical transmittance spectroscopy. *Journal of Applied Physics*, *114*. https://doi.org/10.1063/1.4811682

Nie, J., Mo, Y., Zheng, B., Yuan, H., & Xiao, D. (2013). Electrochemical fabrication of lanthanum-doped TiO2 nanotube array electrode and investigation of its photoelectrochemical capability. *Electrochimica Acta*, *90*, 589–596. https://doi.org/10.1016/j.electacta.2012.12.049

Nyamukamba, P., Tichagwa, L., Mamphweli, S., & Petrik, L. (2017). Silver/Carbon Codoped Titanium Dioxide Photocatalyst for Improved Dye Degradation under Visible Light. *International Journal of Photoenergy*, *2017*, e3079276. https://doi.org/10.1155/2017/3079276

Péter, L. (2021). *Electrochemical Methods of Nanostructure Preparation*. Springer International Publishing. https://doi.org/10.1007/978-3-030-69117-2

Piscopo, C. G., Polyzoidis, A., Schwarzer, M., & Loebbecke, S. (2015). Stability of UiO-66 under acidic treatment: Opportunities and limitations for post-synthetic modifications. *Microporous and Mesoporous Materials*, *208*, 30–35. https://doi.org/10.1016/j.micromeso.2015.01.032

Ponomareva, V. G., Shutova, E. S., Kovalenko, K. A., & Fedin, V. P. (2022). New Type of Nanocomposite CsH2PO4-UiO-66 Electrolyte with High Proton Conductivity. *Molecules*, *27*(23), 8387. https://doi.org/10.3390/molecules27238387

Qilin, G., Yong Ng, H., Dan, Z., & Wang, J. (2020). Metal-Organic Frameworks (MOFs)-boosted filtration membrane technology for water sustainability. *Elements*. https://scholarbank.nus.edu.sg/handle/10635/169561

Ramsden, J. (2016). *Nanotechnology: An introduction* (Second edition). William Andrew is an imprint of Elsevier.

Raut, S. S., Patil, G. P., Chavan, P. G., & Sankapal, B. R. (2016). Vertically aligned TiO2 nanotubes: Highly stable electrochemical supercapacitor. *Journal of Electroanalytical Chemistry*, *780*, 197–200. https://doi.org/10.1016/j.jelechem.2016.09.024

Rojviroon, T., Rojviroon, O., Sirivithayapakorn, S., & Angthong, S. (2021). Application of TiO2 nanotubes as photocatalysts for decolorization of synthetic dye wastewater. *Water Resources and Industry*, *26*, 100163. https://doi.org/10.1016/j.wri.2021.100163

Safari, M., & Mazloom, J. (2023). Outstanding energy storage performance in CoFe bimetallic metal-organic framework spindles via decorating with reduced graphene oxide nanosheets. *Journal of Energy Storage*, *58*, 106390. https://doi.org/10.1016/j.est.2022.106390

Sengupta, A., & Sarkar, C. K. (Eds.). (2015). *Introduction to Nano: Basics to Nanoscience and Nanotechnology*. Springer Berlin Heidelberg. https://doi.org/10.1007/978-3-662-47314-6

Shaban, S. E., Ibrahiem, N. M., El-mongy, S. A., & Elshereafy, E. E. (2013). Validation of scanning electron microscope (SEM), energy dispersive X-ray (EDX) and gamma spectrometry to verify source nuclear material for safeguards purposes. *Journal of Radioanalytical and Nuclear Chemistry*, *296*(3), 1219–1224. https://doi.org/10.1007/s10967-012-2374-x

Sharon, M. (2016). *An Introduction to the Physics and Electrochemistry of Semiconductors: Fundamentals and Applications*. John Wiley & Sons, Inc. https://doi.org/10.1002/9781119274360

Shearer, G. C., Chavan, S., Ethiraj, J., Vitillo, J. G., Svelle, S., Olsbye, U., Lamberti, C., Bordiga, S., & Lillerud, K. P. (2014). Tuned to Perfection: Ironing Out the Defects in Metal–Organic Framework UiO-66. *Chemistry of Materials*, *26*(14), 4068–4071. https://doi.org/10.1021/cm501859p

Song, H., Sun, Z., Xu, Y., Han, Y., Xu, J., Wu, J., Sun, T., Meng, H., & Zhang, X. (2019). Fabrication of NH2-MIL-125(Ti) incorporated TiO2 nanotube arrays composite anodes for highly efficient PEC water splitting. *Separation and Purification Technology*, *228*, 115764. https://doi.org/10.1016/j.seppur.2019.115764

Song, H., Zhang, J., Sun, Z., Sun, T., Han, Y., Meng, H., & Zhang, X. (2020). A novel hybrid electrode of zeolitic imidazolate framework–derived carbon encapsulated in reduced-TiO2 nanotube arrays: Fabrication and photoelectrocatalytic activity. *Applied Organometallic Chemistry*, *34*(9), e5791. https://doi.org/10.1002/aoc.5791

Sun, D., Fu, Y., Liu, W., Ye, L., Wang, D., Yang, L., Fu, X., & Li, Z. (2013). Studies on Photocatalytic CO2 Reduction over NH2-Uio-66(Zr) and Its Derivatives: Towards a

Better Understanding of Photocatalysis on Metal–Organic Frameworks. *Chemistry – A European Journal*, *19*(42), 14279–14285. https://doi.org/10.1002/chem.201301728

Sun, H., Cong, S., Zheng, Z., Wang, Z., Chen, Z., & Zhao, Z. (2019). Metal–Organic Frameworks as Surface Enhanced Raman Scattering Substrates with High Tailorability. *Journal of the American Chemical Society*, *141*(2), 870–878. https://doi.org/10.1021/jacs.8b09414

Sun, Y., Chen, M., Liu, H., Zhu, Y., Wang, D., & Yan, M. (2020). Adsorptive removal of dye and antibiotic from water with functionalized zirconium-based metal organic framework and graphene oxide composite nanomaterial Uio-66-(OH)2/GO. *Applied Surface Science*, *525*, 146614. https://doi.org/10.1016/j.apsusc.2020.146614

Tan, K., Jensen, S., Feng, L., Wang, H., Yuan, S., Ferreri, M., Klesko, J., Rahman, R., Cure, J., Li, J., Zhou, H.-C., Thonhauser, T., & Chabal, Y. (2019). Reactivity of Atomic Layer Deposition Precursors with OH/H 2 O-Containing Metal Organic Framework Materials. *Chemistry of Materials*, *31*. https://doi.org/10.1021/acs.chemmater.8b01844

Taner Camci, M., Aydogan Gokturk, P., Başaran, M., Ulgut, B., Kocabas, A., Kocabas, C., & Süzer, S. (2023). Dynamics of potential screening upon electrification of solid-ionic liquid interfaces probed by XPS. In K. Wandelt & G. Bussetti (Eds.), *Encyclopedia of Solid-Liquid Interfaces (First Edition)* (pp. 661–680). Elsevier. https://doi.org/10.1016/B978-0-323-85669-0.00097-0

Terracciano, M., Galstyan, V., Rea, I., Casalino, M., De Stefano, L., & Sberveglieri, G. (2017). Covalent functionalization of TiO2 nanotubes array for label-free optical biosensing. *Applied Surface Science*.

Vatandoostarani, S., Bagheri Lotfabad, T., Heidarinasab, A., & Yaghmaei, S. (2017). Degradation of azo dye methyl red by Saccharomyces cerevisiae ATCC 9763. *International*

Biodeterioration & Biodegradation, *125*, 62–72. https://doi.org/10.1016/j.ibiod.2017.08.009

Vellingiri, K., Kumar, P., Deep, A., & Kim, K.-H. (2017). Metal-organic frameworks for the adsorption of gaseous toluene under ambient temperature and pressure. *Chemical Engineering Journal*, *307*, 1116–1126. https://doi.org/10.1016/j.cej.2016.09.012

Wu, Y.-F., Kuo, T.-R., Lin, L.-Y., Kubendhiran, S., Lai, K.-C., Chen, T.-Y., & Yougbaré, S. (2022). Investigating energy storage ability of MIL101-(Fe) derivatives prepared using successive carbonization and oxidation for supercapacitors. *Journal of Energy Storage*, *55*, 105420. https://doi.org/10.1016/j.est.2022.105420

Xie, Q., Li, Y., Lv, Z., Zhou, H., Yang, X., Chen, J., & Guo, H. (2017). Effective Adsorption and Removal of Phosphate from Aqueous Solutions and Eutrophic Water by Fe-based MOFs of MIL-101. *Scientific Reports*, *7*(1), Article 1. https://doi.org/10.1038/s41598-017-03526-x

Xiong, X., Zhang, Y., Wang, L., & Tsang, D. C. W. (2022). Chapter 1—Overview of hazardous waste treatment and stabilization/solidification technology. In D. C. W. Tsang & L. Wang (Eds.), *Low Carbon Stabilization and Solidification of Hazardous Wastes* (pp. 1–14). Elsevier. https://doi.org/10.1016/B978-0-12-824004-5.00031-1

Xu, Q., Li, Y., Ji, W., Mei, J., & Wang, X. (2023). Adsorption-Induced In-Situ Construction of TiO2 Hollow Sphere/UiO-66-NH2 Heterostructures with Boosted Photocatalytic Activity toward Cr(VI) Reduction. *ChemNanoMat*, *9*(5), e202300051. https://doi.org/10.1002/cnma.202300051

Xu, W., Dong, M., Di, L., & Zhang, X. (2019). A Facile Method for Preparing UiO-66 Encapsulated Ru Catalyst and its Application in Plasma-Assisted CO2 Methanation. *Nanomaterials*, *9*(10), 1432. https://doi.org/10.3390/nano9101432

Xue, C., Zhang, F., Chang, Q., Dong, Y., Wang, Y., Hu, S., & Yang, J. (2018). MIL-125 and NH2-MIL-125 Modified TiO2 Nanotube Array as Efficient Photocatalysts for Pollute Degradation. *Chemistry Letters*, *47*(6), 711–714. https://doi.org/10.1246/cl.180010

Yang, F., Li, W., & Tang, B. (2018). Facile synthesis of amorphous UiO-66 (Zr-MOF) for supercapacitor application. *Journal of Alloys and Compounds*, *733*, 8–14. https://doi.org/10.1016/j.jallcom.2017.10.129

Yang, H., & Fei, H. (2017). A generic and facile strategy to fabricate metal–organic framework films on TiO2 substrates for photocatalysis. *Dalton Transactions*, *46*(9), 2751–2755. https://doi.org/10.1039/C7DT00082K

Yost, B. T., Gibbons, B., Wilson, A., Morris, A. J., & McNeil, L. E. (2022). Vibrational spectroscopy investigation of defects in Zr- and Hf-UiO-66. *RSC Advances*, *12*(35), 22440–22447. https://doi.org/10.1039/D2RA03131K

You, S.-M., El Rouby, W. M. A., Thamilselvan, A., Tsai, C.-K., Darmanto, W., Doong, R.-A., & Millet, P. (2020). Fe/Ni Bimetallic Organic Framework Deposited on TiO2 Nanotube Array for Enhancing Higher and Stable Photoelectrochemical Activity of Oxygen Evaluation Reaction. *Nanomaterials*, *10*(9), Article 9. https://doi.org/10.3390/nano10091688

Yu, W., Xu, M., Liang, X., Wang, J., Fang, W., & Wang, F. (2023). Construction of a novel Cu1.8S/NH2–La MOFs decorated Black-TNTs photoanode electrode for high-efficiently

photoelectrocatalytic degradation of 2, 4-dichlorophenol. *Chemosphere*, *313*, 137591. https://doi.org/10.1016/j.chemosphere.2022.137591

Zakir, O., Ait Karra, A., Idouhli, R., Elyaagoubi, M., Khadiri, M., Dikici, B., Aityoub, A., Abouelfida, A., & Outzourhit, A. (2022). Fabrication and characterization of Ag- and Cu-doped TiO2 nanotubes (NTs) by in situ anodization method as an efficient photocatalyst. *Journal of Solid State Electrochemistry*, *26*(10), 2247–2260. https://doi.org/10.1007/s10008-022-05237-4

Žerjav, G., Žižek, K., Zavašnik, J., & Pintar, A. (2022). Brookite vs. rutile vs. anatase: What`s behind their various photocatalytic activities? *Journal of Environmental Chemical Engineering*, *10*(3), 107722. https://doi.org/10.1016/j.jece.2022.107722

Zhang, H., Jia, M., Tong, J., Peng, H., Xiang, Y., Chen, Z., Xu, Z., Yang, Z., & Xiong, W. (2023). Coupling effects between metal–organic framework derivatives and oxygen-deficient TiO2 nanotubes: Identified charge-transfer processes and photoelectric synergistic effect. *Environmental Science: Nano*, *10*(8), 1993–2009. https://doi.org/10.1039/D3EN00223C

Zhang, J., Hu, Y., Qin, J., Yang, Z., & Fu, M. (2020). TiO2-UiO-66-NH2 nanocomposites as efficient photocatalysts for the oxidation of VOCs. *Chemical Engineering Journal*, *385*, 123814. https://doi.org/10.1016/j.cej.2019.123814

Zhang, Q., Yang, B., Tian, Y., Yang, X., Yu, R., Wang, J., Deng, T., & Zhang, Y. (2022). Fabrication of silicotungstic acid immobilized on Ce-based MOF and embedded in Zr-based MOF matrix for green fatty acid esterification. *Green Processing and Synthesis*, *11*(1), 184–194. https://doi.org/10.1515/gps-2022-0021

Zhong, S., Xi, Y., Chen, Q., Chen, J., & Bai, S. (2020). Bridge engineering in photocatalysis and photoelectrocatalysis. *Nanoscale*, *12*(10), 5764–5791. https://doi.org/10.1039/C9NR10511E

Zhou, S., Guo, J., Dai, Z., Liu, C., Zhao, J., Gao, Z., & Song, Y.-Y. (2021). Engineering Homochiral MOFs in TiO2 Nanotubes as Enantioselective Photoelectrochemical Electrode for Chiral Recognition. *Analytical Chemistry*, *93*(35), 12067–12074. https://doi.org/10.1021/acs.analchem.1c02326

Zhou, X., Huang, W., Shi, J., Zhao, Z., Xia, Q., Li, Y., Wang, H., & Li, Z. (2014). A novel MOF/graphene oxide composite GrO@MIL-101 with high adsorption capacity for acetone. *Journal of Materials Chemistry A*, *2*(13), 4722–4730. https://doi.org/10.1039/C3TA15086K

9. Annexes

9.1. Annex 1.

Five cyclic experiments of the PEC degradation of methyl red (1.3 V) with the TiO_2 NTs-MOF(Zr) electrode and its comparison with the bare TiO_2 NTs electrode.

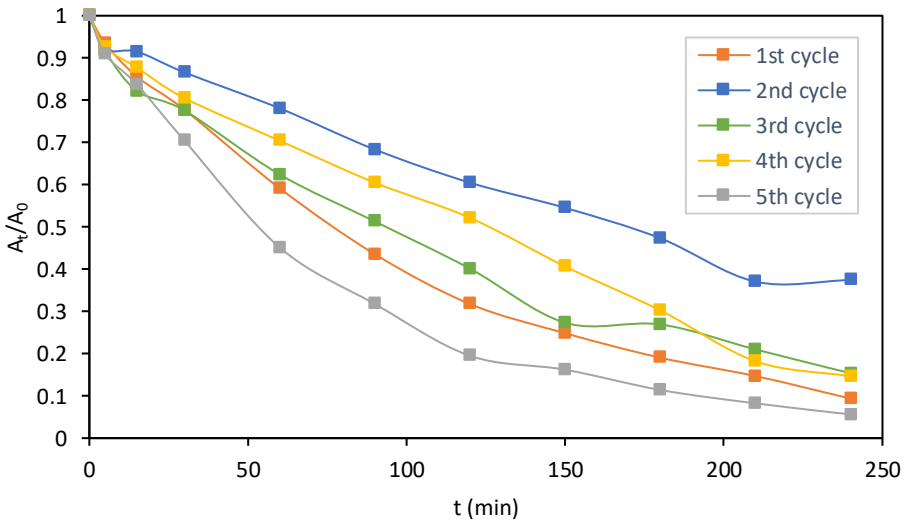

9.2. Annex 2.

Five cyclic experiments of the PC degradation of methyl red with the TiO_2 NTs-MOF(Zr) electrode.